UNIVERSITA' DEGLI STUDI DI MILANO
Facoltà di Scienze Matematiche Fisiche e Naturali
Corso di laurea magistrale in Fisica

STUDIES OF A GAMMA-BLIND FAST-NEUTRON IMAGING DETECTOR FOR BNCT APPLICATIONS

Relatore interno : Prof.ssa Grazia Gambarini
Relatore esterno : Prof. Amos Breskin
Correlatore : Dott. Giuseppe Battistoni

Tesi di Laurea di
Irene Carne
Matricola n° 701700
Cod. PACS 87.53.-j

Anno Accademico 2006-2007

“Anyone who has never made a mistake
has never tried anything new”

A. Einstein

Contents

Introduction

The goal of the proposed research activity is to develop a fast neutron imaging detector, based on thick gas electron multiplier (THGEM) [1], blind to gamma radiation, in order to evaluate the fast neutron component and its spatial distribution at the collimator of a reactor epithermal column designed for Boron Neutron Capture Therapy (BNCT) treatment.

BNCT is form of radiation therapy [2,3], currently in the research stage, that takes advantage of the high cross section, for slow neutrons, of the reaction of the stable isotope ^{10}B, previously selectively accumulated in the tumour tissue:

$$^{10}B(n,\alpha)^{7}Li \quad (\sigma = 3840 \text{ barn})$$

The produced energetic short-range alpha particles and lithium ions deposit most of their energy within the cell containing the original ^{10}B atom. Currently, epithermal neutron beams with sufficient intensity for BNCT treatment of patients, can only be produced in nuclear reactors. The total absorbed dose in tissue irradiated with such beams originates from thermal neutrons, intermediate and fast neutrons and gamma rays. The various dose components have a different relative biological effectiveness (RBE) and therefore have to be determined separately [4]. Consequently, for the BNCT treatment planning is important to determine the spatial dose component distributions, in agreement with the desired neutron beam parameters defined by the International Atomic Energy Agency (IAEA) is important [5].

For the safe treatment of patients with ionizing radiation, it is of crucial importance that the basic characteristics of the neutron beam (beam geometry, neutron and spectrum, absorbed dose and fluence distributions), are determined with in-air and in phantom, in a coherent and reproducible way. Therefore, reliable dose-monitoring systems are needed in order to verify that the characteristics of the beam satisfy all the required restrictions. Because of the complexity of the mixed (thermal/epithermal/fast) neutron and gamma ray fields, the currently Codes of Practice for radiotherapy dosimetry are not applicable to BNCT. In order to inspect the dosimetric procedure used in different BNCT facilities and set up a protocol on the basis of the methods judged more suitable, an international commission worked on a common project for 4

years from 1998. At the end of the activity the partners had evinced that the original title of "Code of Practice" might be somewhat too ambitious. The commission could only argued that much research is still necessary to propose standard methods. The final document is therefore produced as a set of "recommendations" [6].

Most of the beams aimed at BNCT are designed to have a broad energy spectrum ranging from a few eV up to about 30 keV. However, the presence of a fast-neutron component is unavoidable. These additional neutrons with energies greater then 30 keV contribute to most of the neutron dose in tissue. Consequently, a number of techniques have been adapted to the measure of spectra of BNCT beams from thermal to 15 MeV. The methods applied at different BNCT beams have been critically analysed and compared [6, 7] to evaluate the consistency and the satisfactory.

Activation methods are techniques used to determine neutron flux by measuring the radioactivity induced in proper materials as a result of neutron capture. The induced activity is related to the irradiating neutron fluence rate, that can therefore be obtained by analysing the gamma-rays spectrum emitted by the produced nuclei. The results from the activation measurements are used as input for an adjustment process which combines cross section data with the calculated neutron spectrum, resulting in a final estimation of the thermal-, epithermal- and fast-neutron fluxes and their uncertainties. Copper, indium, gold or manganese foils are usually utilized, both bare and cadmium-covered, in order to measure the fluxes above and below cadmium cut-off energy (0.5 eV). With a multiple-foil activation technique, the method can also be used for neutron spectrometry. To this aim, different activation materials, whose cross section shows resonances at different energies, are utilized. In case of the irradiation fields developed for BNCT, considering the response region of the other types of detectors, as a function of the neutron energy, this method is appropriate and then is it the most utilized owing to its simplicity.

In the measurements performed by Voorbraak et al. (Petten - 1991) the design was an activation foil set which can be used for the determination of the thermal, epithermal and fast components of the neutron beam spectrum free-in-air and which can be used also to adjust the calculated neutron beam spectrum. Both thermal and resonance reactions are utilized to cover the thermal and epithermal neutron energy range up to 5 keV. The resonance neutron detectors, with a diameter of 12 mm, are placed inside a cadmium box with walls of 1 mm thickness to cut off the

thermal neutrons. Information about the fast part of the neutron energy spectrum, above ~0.5 MeV, is obtained from three threshold detectors, with a diameter of 20 mm. An additional gold foil is irradiated in front of the cadmium capsule. The set of detectors and their parameters are presented in Tab. I. The thermal and resonance detector materials are diluted in Al in order to prevent self-shielding and perturbation of the beam. The order of the foil materials in the set agrees with the increase of the main resonance energy of the reactions and also with the increase of the threshold for the threshold detectors.

Reaction	Cover		Composition	Foil thickness (mm)
Thermal				
^{197}Au (n,γ) ^{198}Au			1 % in Al	0.2
Resonance		Resonance energy		
^{115}In (n,γ) ^{116}In	Cd	1.457eV	0.2 % in Al	0.2
^{45}Sc (n,γ) ^{46}Sc	Cd	5000 eV	99.99 %	0.1
^{197}Au (n,γ) ^{198}Au	Cd	4.906 eV	1 % in Al	0.2
^{238}U (n,γ) ^{239}U	Cd	6.7 eV	23 % in Al	0.1
^{186}W (n,γ) ^{187}W	Cd	18.8 eV	1 % in Al	0.2
^{139}La (n,γ) ^{140}La	Cd	73.5 eV	5 % in Al	0.2
^{55}Mn (n,γ) ^{56}Mn	Cd	337 eV	1 % in Al	0.2
^{63}Cu (n,γ) ^{64}Cu	Cd	580 eV	10 % in Al	0.2
Threshold		Threshold energy		
^{115}In (n,n') ^{115m}In		0.5 MeV	100 %	0.1
^{58}Ni (n,p) ^{58}Co		1.9 MeV	100 %	1.0
^{27}Al (n,α) ^{24}Na		6.5 MeV	100 %	1.03

Tab. I. Free-beam foil set (Voorbraak et al., 1991)

The activation method is also used at the HK-10 epithermal neutron beam of the LVR-15 at BRI, Řež. The set of activation foils is based on the Petten set as described by Marek et al., 1998. The SAND-PC (Marek, 1998) and BASACF (Tichy, 1990) codes with the cross-section data libraries IRDF-90 (Kocherov and McLaughlin, 1993, Griffin et al., 1994), SNLRML (Griffin et al., 1993) and DOSCROS84 (Zijp et al., 1984) are used for the adjustment. The

BASACF code, which assumes the normal distribution of the activities, spectra and cross-sections, is based on the Bayesian approach to the problem solution. The program needs all statistical information including the covariance matrices of the activities, spectrum and cross-sections to be entered. Typical values (1 STD) for the uncertainty of the adjusted neutron spectrum in epithermal neutron fields of interest in BNCT are:

- 20-25 % (in the thermal neutron energy region),
- 5-10 % (in the intermediate neutron energy region),
- 25-30 % (in the fast neutron energy region),

depending on the quality of the input data used in the spectrum adjustment. In the thermal- and fast-neutron regions these values are much higher than in typical reactor beam. However, for the purpose of treatment planning and in-phantom dosimetry, the epithermal part of the spectrum dominates the source term.

Bonner sphere spectrometer BS (see chapter 3) consists of a number of moderating-spheres having different diameters, typically made of polyethylene, with a thermal neutron sensor at the centre. The generally adopted set of the moderating spheres has diameters from 7.62 cm (3") up to 45.72 cm (18"). The most frequently used thermal neutron detector is a scintillation crystal ^{6}LiI(Eu) utilising the (n,α) reaction on lithium (Nachtigall et al., 1972; Sanna, 1973). The reaction (n,α) on ^{10}B was used e.g. by Maerker et al., 1971, in a proportional chamber filled with BF_3. Morgues et al., 1975 used a small-volume proportional counter filled with ^{3}He. Further possibilities are the TLD 600 thermoluminescent detectors (Engelke et al., 1974), solid-state track detectors in contact with ^{235}U (Tichy et al.,1980) and activation detectors (Spurny et al., 1979). More recent works (Hertel et al., 1985; Mares et al., 1991, 1994, 1995), based on experiments and neutron transport calculations, have re-examined the response of the spherical moderators for different types of thermal neutron detectors. To interpret the Bonner sphere measurements, the response function of the chosen detector has to be determined for each sphere, in a broad energy range, typically from thermal to 20 MeV. For reliable determinations of response functions, both Monte Carlo calculations and experimental calibrations in standard neutron fields are necessary. Owing to the spherical shape of the moderators, the response results to be isotropic. Many unfolding codes have been developed to attain the final spectrum,

and improvements are still studied. Nevertheless, the validity of Bonner spheres results, in particular for BNCT epithermal neutron beams, has been mostly questioned. An example of Bonner spheres application to BNCT neutron beams was described by Marek et al., 1998 (BRI, Řež). The thermal sensor was a cylindrical 4 x 8 mm Li(Eu) scintillation detector and the polyethylene spheres have diameters of 5.08, 7.62, 10.16 and 12.7 cm. As the beam diameter is usually smaller then 15 cm, only these four spheres and the bare detector were used for the spectral measurements.

An international comparison of different types of neutron spectrometers (Klein 1997, Kluge 1997) shows that the expected uncertainties (1 STD) in case of BS are as follows:

- ~ 4 % (for the total neutron fluence rate),
- ~ 8 % (for the neutron fluence rate in the thermal neutron energy region),
- 10-20 % (for the neutron fluence rate in the intermediate neutron energy region),
- 10-20 % (for the neutron fluence rate in the fast neutron energy region)

The *proportional counter with hydrogen gas* is a method of measuring neutron spectra based on recording hydrogen recoil nuclei. This has been known for a long time and found widespread application in a variety of recording systems in which the energy of protons is measured. The attractiveness of the method is based on the fact that the cross-section for the scattering of the neutrons by hydrogen nuclei is well known, the scattering is isotropic in the centre of mass system, the proton recoil spectrum has a simple "rectangular" distribution.

A *spherical proportional counter* filled with hydrogen gas, presented by Jansky (1991) has been used to measure fast-neutron spectra ranging in the energy interval between 60 keV and 1.5 MeV. To cover such a wide energy range, three counters filled with hydrogen of different pressures (1, 3 and 10 atm) were used. The calibration of the spectrometer was performed on the basis of measurement of leakage neutron spectra from iron spheres of 20, 30 and 50 cm in diameter and a D_2O filled sphere of 30 cm in diameter having a ^{252}Cf neutron source installed in the centre. The proton recoil spectrum obtained by the measurements is unfolded to the neutron spectrum using a direct differentiation algorithm with a correction related to the neutron interaction with hydrogen nuclei and to the proton escape from the detector volume. The uncertainty of the resulting neutron spectrum depends on the uncertainty of the energy calibration, which is 1 to 2% (1 STD), the detector efficiency, which is 2-3% (1 STD), and the

statistical error. The measureme uncertainty is better than 10% (1STD) in the whole energy range between 60 keV and 1.5 MeV.

Proton and alpha recoil counters were developed at Harwell Laboratory (Oxfordshire, UK) for radiological purpose. The system consists of three spherical proportional counters filled with hydrogen to pressures approximately 1, 3 and 10 atm, covering the range of 10 keV to 1.5 MeV. To extend this energy range up to 15 MeV, an alpha counter (^{4}He) is used. Since as it has a low energy limit at 2 MeV, it is necessary to interpolate the neutron energy spectrum between the upper energy limit of the proton recoil counters and the low energy limit of the alpha counter. Further, for neutrons with energy in the range of ^{4}He counter, the fluence rate relative to those in the range for the other counters is small, so the counting statistics obtained using this counter in simultaneous measurements with the other counters are poor. Therefore, unfolding the spectra in the conventional ways is not possible. Consequently, it was necessary to develop a method for estimating the fluence rates in broad energy bins by comparing the areas under the alpha recoil distribution with obtained for mono-energetic neutrons used for calibration. An improvement to this method would be to use this counter at higher power, although this is not always practicable.

The application of a *scintillation spectrometer with a stilbene crystal* to determine the fast neutron spectrum in BNCT is described by Marek (1990). The size of the crystal was 10 x 10 mm, the discrimination of gamma rays was based on the different shape of the scintillation pulses (the PSD method). The spectrum was measured at low reactor power in two parts: one part covers energy interval ~0.5 up to 3 MeV and the second 1.5 up to 12 MeV. Reconstruction of the neutron spectrum from the proton recoil spectrum was based on the Johnson algorithm (Johnson, 1981) that uses the direct differentiation technique. Correction of multiple-neutron scattering of hydrogen, proton escape and neutron interactions with carbon nuclei were included in the unfolding process. The total uncertainty in the neutron spectrum is estimated to vary from 7% (1 STD) at a neutron energy of 1 MeV to 15% (1 STD) at 10 MeV.

A series of neutron energy spectrometry techniques has been described, showing the necessity to improve a new system for fast-neutron spectrometry. We firstly proposed a detector prototype made of a polyethylene (polypropylene) layer for fast-neutron to proton conversion, coupled to two cascaded THGEMs (see Chapters 1 and 2) and a dedicated read-out electrode, for a robust,

cheap and simple fast-neutron spatial detection procedure. The detector could provide an estimation of the fast neutron dose component and its spatial distribution for applications in Boron Neutron Capture Therapy (BNCT). For a good spatial characterization of a fast-neutron beam, the detector should have high neutron detection efficiency and low sensitivity to gamma rays. The design of the system requires an optimization of the radiator converter geometry according to the neutron source parameters.

The THGEM, introduced in 2004 at the Radiation Detection Laboratory at Weizmann Institute of Science (Rehovot, Israel), is the most recent development in gaseous hole-multipliers. It is geometrically expanded version of the standard GEM. It's fabricated with a standard Printed-Circuit Board (PCB) technique out of double-clad insulating-material plates; the electrode consists of mechanically drilled holes in the plate, with a chemically etched rim (typically 0.1 mm) around each hole; the latter is essential for reducing the probability of gas breakdowns; higher permissible voltages and hence higher detector gain may then be attained. The THGEM operation principle is identical to that of a standard GEM. Upon application of a voltage difference across the THGEM, a strong dipole field is established within the holes. Electrons deposited by ionizing radiation in a conversion region above the THGEM are drifted towards the THGEM under an electric field and are focused into the THGEM holes by the strong electric field inside the holes. Each hole acts as an independent multiplier, which is separated from other avalanches. The avalanche confinement within the holes has the advantage of reduced photon-mediated secondary effects; this leads to high-gain operation in a large variety of gases [6].

After a preliminary study of the converter-THGEM system, that presented poor efficiency below 5 MeV, a new configuration was proposed and studied. The detector concept has a moderator layer of polyethylene (with variable thickness) to decelerate fast-neutrons and a slow-neutron converter foil on the back, coupled to two cascaded THGEMs. The moderator layer comprises a slow neutron absorbing isotope to increase spatial resolution and reduce the gamma component. For the first numerical studies of the method it was decided to use pure ^{6}Li as absorber dopant in the moderator and a metallic ^{6}Li n-converter foil. The principle is very similar to the Bonner sphere [7], but instead of spherical geometry we proposed to use a set of flat plates with different thickness. For neutron spectrometry, the Bonner sphere spectrometer (BS) is presently the only system which covers the whole energy range from thermal to GeV

neutrons. Such a system, as described before, consists of a thermal neutron sensor (as ^{6}LiI(Eu) scintillator) which is placed at the centre of polyethylene spheres with different diameters (3" to 18"). From the measured reading of a set of spheres, information can be derived about the spectrum of the neutron field in which the measurements were made. The derivation of this spectral information is not simple: the codes are complex and required several input parameters obtained from realistic a priori information, mainly based on guessed spectrum and beam divergence. As consequence, the validity of BS results, obtained for the characterization of a reactor beam, has often been questioned. The collimator has typically a 12-15 cm of side or diameter and the Bonner spheres have diameters up to 45.72 cm. The position of the centre of the spheres for a set of measurements has to be the same and is determined by the maximum chosen diameter. In Fig. I, II some experimental set-ups are shown; it is evident that the results are strongly dependent on the precision of the input parameters, like the beam divergence. The expectation is that the new proposed flat-geometry should allow to reduce such drawbacks and moreover to obtain spatial information.

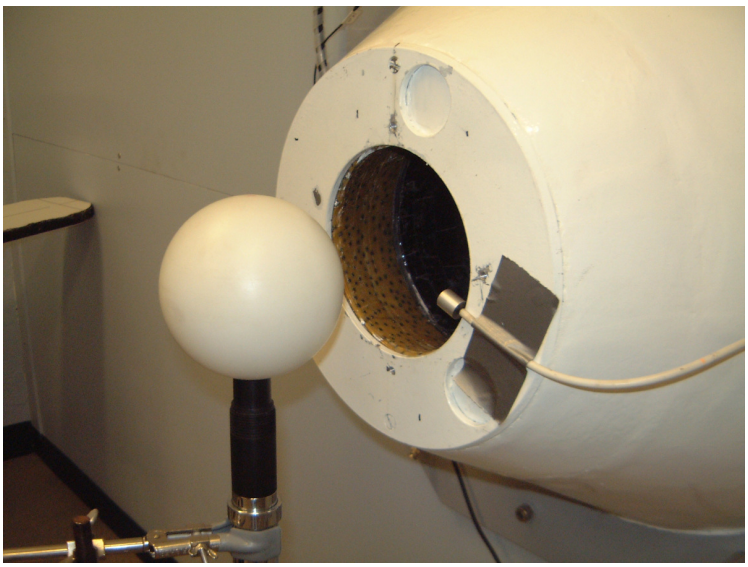

***Fig I**. Example of Bonner spheres measurements*

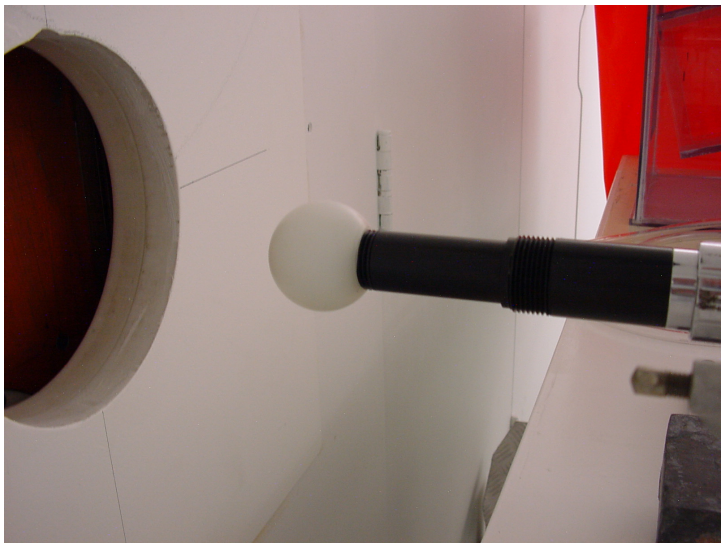

Fig II. *Beam profile measurements with Si(Li) detector inside a Bonner sphere in front of the HFR (Petten) beam exit*

The thesis activity was based both on Monte Carlo calculations, using GEANT4 and MCNP [8, 9] simulation code, and experimental activities, aimed to perform feasibility studies and develop of a THGEM-based detector prototype, for fast neutron imaging with low gamma sensitivity.

Chapter 1 - THick Gas Electron Multiplier (THGEM)

1.1 Introduction

Progress in experimental particle physics has always been strictly linked to improvements in accelerator and detector technologies [10]. In particular, experiments are based on the ability of researchers to detect particles produced by large accelerators or storage rings. In the last century several major inventions in the field of gaseous detectors were made. Let us just mention the Geiger counter [11], parallel plate detectors [12] and multi-wire proportional chambers (MWPC) [13]. The main feature of all of these detectors is that they exploit gas multiplication or Townsend avalanches.

Multiwire Proportional Chambers (MWPC) have been the most employed large area, flat geometry, photo-detectors in particle physics where two-dimensional localization of particles is required. The inventor of this detector, G. Charpak, was awarded the Nobel Price in 1992. However, though MWPC-based detectors are economic and with relative high spatial resolution, due to their open geometry, they suffer from secondary effects; as a result, their gain is therefore limited and they have low local count rate due to space-charge limitation.

A new era in gas detector development began with the introduction of micro-pattern detectors, based on electrodes formed on insulating substrates by micro-lithographic technologies [14]. Due to their performances, the micro-pattern based detectors have become an interesting alternative for radiation detection and imaging in a large variety of applications [15]. They are characterised by a fast avalanche process and high position resolution. However, micro-pattern gas detectors are limited in size, expensive, fragile and again due to the open geometry some of them suffer form secondary effects. The microelectronic techniques eventually triggered a chain of many other inventions, all of them grouped under the title of micro-pattern gaseous detectors (MPGD); it is quite a wide class of detectors, from strips, to dots and to hole-type structures. It will thus be useful to introduce a definition for micro-pattern detectors: they are high granularity gaseous detectors with small (below 1 mm) distances between the anode and the cathode electrodes.

The most extensively studied micro-pattern gaseous detector has hole-type structure, the so called Gas Electron Multiplier (GEM); it was introduced by F. Sauli in 1997 [16] and it has typically 50-70-μm diameter holes chemically etched in a 50-μm thick metalized Kapton foil. Its operation principle is based on electron avalanche multiplication inside gas medium; electron drift into the GEM holes, where due to a strong electric field (~80 kV/cm) they gain enough energy to ionize the gas molecules, which, as shown in Fig 1.1, results in avalanche process. It operates in a large variety of gases, including noble-gas mixtures, providing a gain of ~10^3 in a single element and gains exceeding 10^6 in a cascade of 3-4 elements. Furthermore, gas avalanche multiplication within small holes is attractive because the avalanche confinement in the hole strongly reduces photon-mediated secondary effects and hole-multiplication provides true pixilated radiation localization.

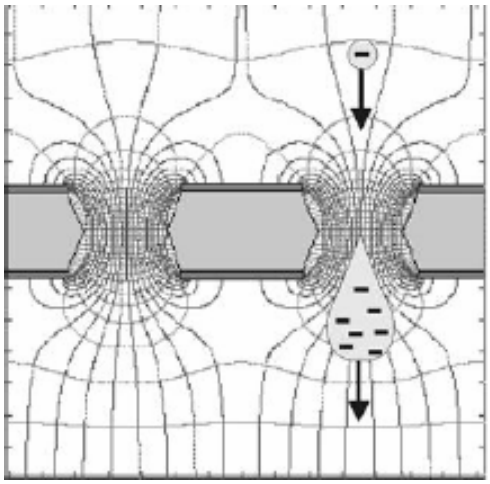

Fig 1.1*. Schematic view of the operational principle of the standard GEM. Electrons follow the field lines and are focused into the holes, where an avalanche multiplication process takes place at the strong electric field there.*

1.2 Gaseous detectors

Detection and transport inside the gas

Charged particles and photons traveling inside a gas medium can interact with it in many ways. The most probable interaction, generally used for detection, is the electromagnetic interaction, which results in both excitation and ionization of the gas molecules. The energy required for creating an electron-ion pair depends on the gas type and is typically around 25-35 eV.

Photon interactions with the gas molecules depend on the photon energy. At low energy up to several keV, the dominant process is the photoelectric one. At the range over 10 keV Compton scattering takes over and at energies above MeV electron-positron pair production is the most probable process. In our test experiments, x-rays were absorbed in gas resulting in its ionization by the emitted primary electrons, resulting in photoelectrons emitted into the gas medium. X-ray interaction with the gas molecules is a quantum process involving one or more transitions in the atomic electron shells of the gas molecule components. The attenuation of the x-ray flux in the medium is a function of its energy and of the medium composition. Its absorption length in the medium is given by:

$$\lambda = \frac{1}{N\sigma}$$

where N is the gas density and σ is the cross section for collisions.

We used, in our laboratory experiments, a ^{55}Fe source which emitted 5.9 keV x-ray photons, so in the Argon atomic shell (Ej) of 3.2 keV results an emission of a primary photoelectron with an energy of 2.7 keV (5.9 keV-3.2 keV). The photoelectron has a range of about 100 microns at one atmosphere. The residual ionized and excited molecule can decay to its ground state mainly via two mechanisms. The first one is the fluorescence (i.e. internal electron transition with photon emission Ej - Ei (from atomic level Ej to lower atomic level Ei)). This secondary photon has energy smaller than the ionization threshold and thus a very long mean-free-path for absorption; it can therefore escape the volume of the detector. The second mechanism is the Auger effect, this is a rearrangement of the atomic electrons followed by the emission of a second electron of energy 3.2 keV. For example in Argon we have photon emission in 15% of the cases and in 85% of the cases two electrons emission.

The passage of a charged particle in a medium results in a discrete number of primary ionizing collisions, which liberate primary election-ion pair. Some ejected electrons can have enough energy to further ionize the medium, producing secondary electron-ion pairs; the total number of electron-ion pairs can be express by:

$$n = \frac{\Delta E}{W_i}$$

Where, ΔE is the energy-loss in the medium (e.g. gas volume), and W_i is the effective average energy to produce one electron-pair (i.e. 22 eV for Ar/CH_4). The total charge created in the gas

is either collected at the read out electrode or is multiplied in the gas to yield detectable pulse-signals proportional to the deposited energy.

If an external electric field *E* is applied across the gas volume, a net movement of the ions along *E* direction is observed. This net motion is the effect of collisions with the gas molecules and acceleration by the field *E* between successive collisions. The average velocity of this slow motion is called ion drift velocity *v* and it is defined as

$$v = \mu \frac{E}{p}$$

where *p* is the gas pressure and μ the ion mobility. This tends to remain fairly constant over wide range of electric field and gas pressure, and does not differ greatly for either positive or negative ions typical values are between 1 and $1.5*10^{-4}$ $m^2*atm/V*s$. The mobility of electrons, except for very low fields, is not constant. In fact, due to their small mass, electrons can substantially increase their energy between collisions with the gas molecules under the influence of an electric drift field E_{drift}. In a simple formulation, one can write the drift velocity, as:

$$v_e = \frac{eE_{drift}}{2m}\tau$$

where τ is the mean time between collisions and *m* the electron mass. At high fields, a typical value of v_e is around 5 cm/μs, which is roughly 1000 times grater than that for ions under similar conditions [17].

THGEM's can be coupled to solid radiation converter: it can be placed above the THGEM or deposited directly on its top face. In both cases the radiation-induced emitted electrons are efficiently focused into the multiplication holes. The solid converter material can be chosen according to the application; it can be a photocathode in gaseous photomultipliers [18], an x-ray converter (e.g. CsI) in secondary-emission x-ray imaging detectors [19] or a neutron converter (e.g. Li, B, Gd, polyethylene etc.) in thermal-or fast-neutron imaging detectors [20]. The proposed detector prototype is based on neutron moderation and absorption inside a ^{6}Li enriched high-hydrogen material, coupled with a ^{6}Li foil for the thermal neutrons conversion in charged particles. The description of the particle interactions is presented in Chapter 2

Gas multiplication

Gas multiplication is a consequence of increasing the electric filed within the gas to a sufficient high value. At electric fields above a few kV/cm, electrons are easily accelerated by this and may have significant kinetic energy to cause excitations and ionizations of the gas molecules. The excitations result, among others, in photon emission; these photons can create secondary electron emission, perturbing the process of detection (photon feedback). Adding complex molecules to noble gases, such as hydrocarbons which have radiation-less transitions, will absorb these photons and therefore will reduce secondary effects. The process of ionizations by electron collisions is the basis for the avalanche multiplication. If the kinetic energy of electrons is greater than the ionization energy of neutral gas molecule, it is possible for an additional ion pair to be created in the collision. After a mean free path l electron-ion pair will be produced, and the two electrons will continue to generate, again after one mean free path, two additional electron-ion pairs and so on. This gas multiplication process therefore takes a form of a cascade, known as Townsend avalanche. If n is number of electrons at a given position and n_0 is the number of electrons at X=0, after a path X, the increase in the number will be exponential:

$$M = \frac{n}{n_0} = e^{\frac{X}{l}}$$

where M represents the multiplication factor. The Townsend coefficient $\alpha = l^{-1}$ is a function of the electric field E and as seen in Fig 1.2 the detected charge depends on the potential difference V_0 that is applied on the electron inside the gas medium. At very low values of voltages, charges begin to be collected, but recombination is still the dominant process. As the voltage is raised, full collection begins (this is the mode of operation in the ionization chamber region). As the voltage is increased, multiplication starts and the detection charge is proportional, through the multiplication factor M, to the original deposited charge. Increasing the applied voltage (800 to 1200 volt range), this proportionality is gradually lost, as a consequence of the electric field distortions due to the large space charge created. This region reaches saturation gain, where the same signal is detected independently of the original ionizing event. At even higher electric fields it is the Geiger-Muller region, where the photon emission process begins to propagate avalanches in the counter, and the full length of the detector becomes a sheath of electrons and ions.

Secondary processes, like photon emission inducing the generation of avalanches spread over the gas volume, photon- and ion-induced secondary avalanches and space charge deformations of the electric field (which is strongly increased near the front of the avalanche), eventually result in spark breakdown.

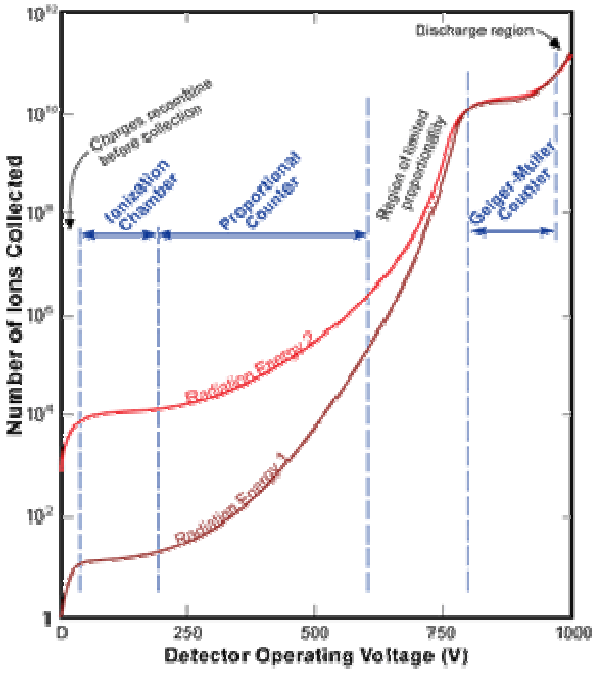

***Fig 1.2**. The different regions of operation of gas filled-detectors. The graph shows the relationship of ion collection in a gas filled detector versus the applied voltage.*

The statistical distribution of the energy of electrons, and therefore of *M*, in general does not allow one to operate at average gains much above 10^6 if one wants to avoid breakdowns. However, a multiplication process inside holes reduces dramatically these secondary effects and therefore allows reaching higher gains. Using the THGEM, stable operation was indeed obtained at gains above 10^7.

Gas mixtures

Gas avalanche multiplication occurs in all gases; experimental requirements restrict the choice to several possibilities, as for instance low working voltage, high gain operation, high rate capabilities, etc… Noble gases have only two ionizing dissipation modes:

- emitting a photon or an electron
- making gas multiplication possible at relatively low field strengths

However, using only a noble gas for electron multiplication will not allow gains higher than $\approx 10^3$. This is because during the avalanche process atoms are excited and will return to the ground state via emission of a photon. The energy of this photon it typically higher than the ionization potential of most metals, resulting in a photo electric effect in the metal of which the detector is constructed, producing additional unwanted avalanches (photon-feedback) not connected to the primary radiation we want to detect. Another possible source of secondary avalanches is produces by ions drift towards the cathode (ions-backflow), which eventually may extract electron from it (ion-feedback). This recombination will also result in an emission of a photon, but in this case, very close to the cathode causing the same effect as discussed earlier. Even at moderate gains, the probability of these processes is high enough to create a situation of permanent discharge. To counter the effect of these secondary avalanches, a second gas consisting of polyatomic molecules (usually hydrocarbons) is added to the noble gas. Because these molecules have a large range of non-radiative excited states (vibrational, rotational, chemical reactions), they allow absorption of photons in a wide energy range. In this way the excess photons, resulting from the de-excitation of the noble gas, can be absorbed without creating secondary avalanches. Another beneficial effect is that these large molecules generally have a lower ionization potential. Because of this, the created noble gas-ions will be able to recombine with electrons by extracting them from the molecule. Adding a small percentage of these quenching gases to the noble gas allow for gas-gains up to 10^6. The quenching efficiency of a polyatomic gas increases with the number of atoms in the molecule. So for operation at high gains, long chains of hydrocarbons are added to the gas mixture. A drawback of using (large) hydrocarbons as a quencher is that they can lose energy by dissociation into smaller radicals. These radicals can either recombine into smaller molecules, or form larger molecules (polymerization). These molecules will become attached to both the cathode and anode and,

since they are insulators, will become electrically charged. This will have an adverse effect on the performance of the detector because of the distortion of the electric field. Because of this ageing effect, the lifetime of gaseous detectors is limited [17].

1.3 THGEM description

The THGEM is actually geometrically expanded version of the standard GEM. It's economically fabricated with a standard Printed-Circuit Board (PCB) technique out of a double-clad insulating material-material plates (FR-4, Kevlar, Teflon, etc…). FR-4 (Flame Retardant 4), for example, is a type of material used for making a Printed Circuit Board (PCB). It describes the board itself with no copper covering. FR-4 is a composite of a resin epoxy reinforced with a woven fiberglass material and it is typically a yellowish color. FR-4 is similar to an older material called G-10, replaced in most applications. The electrode consists of mechanically drilled holes in the plate, with a chemically etched rim (typically 0.1 mm) around each hole (Fig 1.3); the latter is essential for reducing the probability of gas breakdowns; higher permissible voltages and hence higher detector gain may then be attained [6]. The THGEM operation principle is identical to that of a standard GEM. Upon application of a voltage difference across the THGEM, a strong dipole field E_{hole} is established within the holes. Electrons deposited by ionizing radiation in a conversion region above the THGEM are drifting towards the THGEM under the field E_{drift} and are focused into the THGEM holes by the strong electric field inside the holes. The electrons are multiplied within the holes under the high electric field (25-50 kV/cm); depending on the size and direction of the field E_{trans}, a fraction of the resulting avalanche electrons are collected on the THGEM bottom electrode while the rest may be further transferred to a collecting anode or to a successive multiplier element. Each hole acts as an independent multiplier, which is separated from other avalanches. The avalanche confinement within the holes has the advantage of reduced photon-mediated secondary effects; this leads to high-gain operation in a large variety of gases [6]. In this work, measurements were carried out with single-THGEM and double-THGEM detector configurations, as descript in Chapter 2.

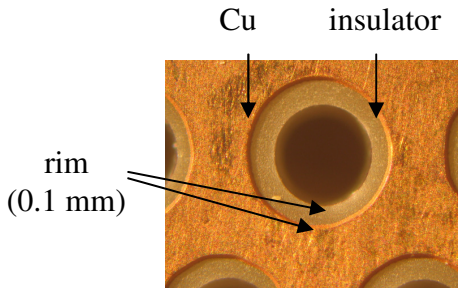

***Fig 1.3**. A photograph of a THGEM: 0.4 mm thickness. A rim of 0.1 mm is etched around the drilled holes.*

1.4 New method of production

A new economically method of THGEM production is in study. The fabrication is still with a standard Printed-Circuit Board (PCB) technique out of a double-clad insulating material plates, but the holes and the rims are created in a different way. A mechanical drilling is first applied on the copper plate and a series of chemical baths are used to etch the rims. Controlling the bath time is possible to control the rim size. Some results for four groups of 3x3 THGEM (rim = 0.04 mm, 0.06 mm, 0.08 mm and 0.12 mm) are presented in Chapter 2.

In the following pictures some examples of rims and holes are shown. The images were taken with the scanning electron microscope (*SEM*). This is a type of electron microscope that creates various images by focusing a high energy beam of electrons onto the surface of a sample and detecting signals from the interaction of the incident electrons with the sample's surface. The type of signals gathered in a SEM vary and can include secondary electrons, characteristic x-rays, and back scattered electrons. In a SEM, these signals come not only from the primary beam impinging upon the sample, but from other interactions within the sample near the surface. The SEM is capable of producing high-resolution images of a sample surface in its primary use mode, secondary electron imaging. Due to the manner in which this image is created, SEM images have great depth of field yielding a characteristic three-dimensional appearance useful for understanding the surface structure of a sample [21]. Fig 1.4 shows the inner surface of the hole and the rim for a 3 x 3 cm^2 THGEM made with the old method of production and Kevlar as insulator material. The rim is not regular and the surface of the hole has fibres sticking out. This last characteristic is also shown in Fig 1.5 for a 3x3 THGEM produced with the old method and FR-4 as insulator. With the new method of production, after

polishing, the rim and the hole seem to have good quality (Fig. 1.6). We still have production problems with the larger 10 x 10 cm^2 THGEM detector.

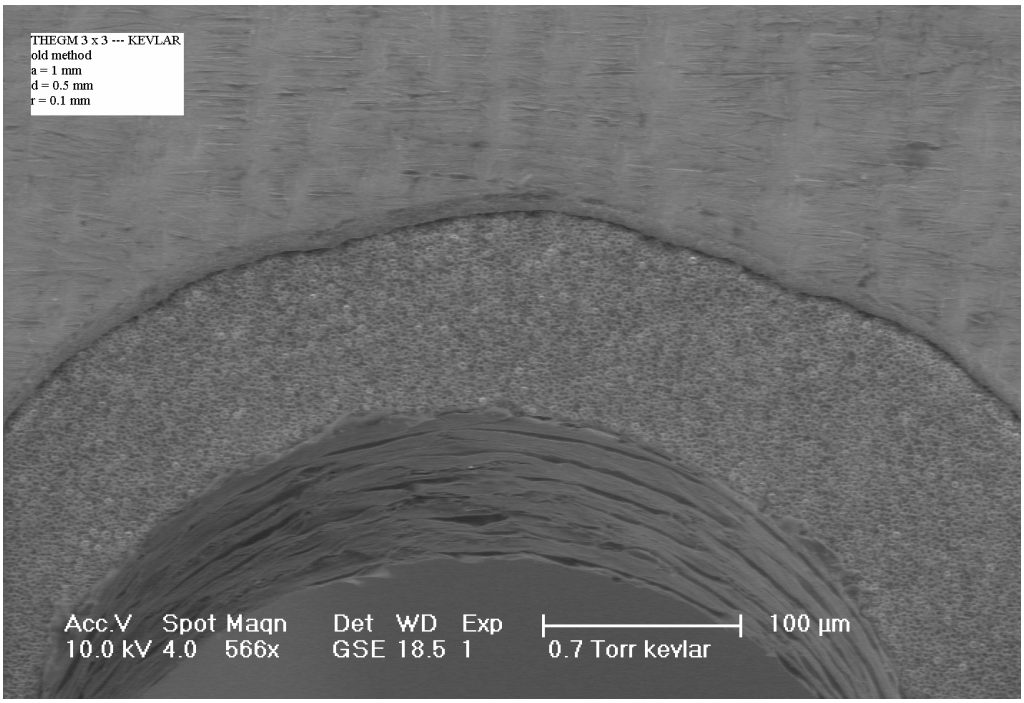

Fig 1.4. *SEM image of 3x3 THGEM produced with the old method (mask) from Kevlar as insulator material (a = 1 mm, d = 0.5 mm, h = 0.1 mm, t= 0.2 mm)*

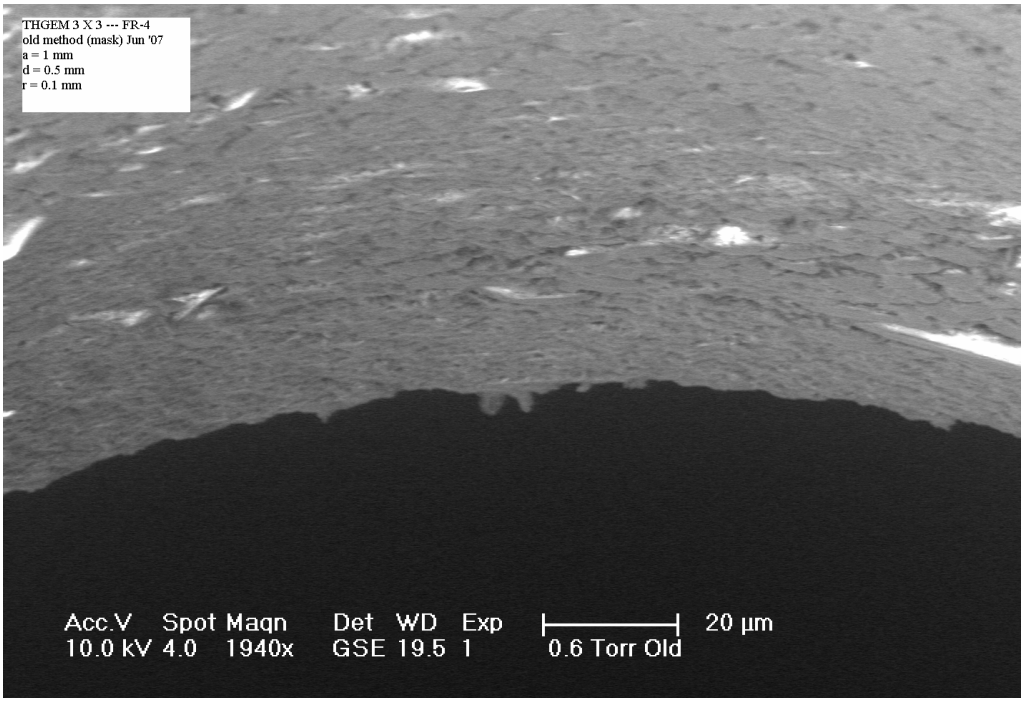

Fig 1.5. *SEM image of 3x3 THGEM produced with the old method (mask) and FR-4 as insulator material (a = 1 mm, d = 0.5 mm, h = 0.1 mm, t= 0.4 mm)*

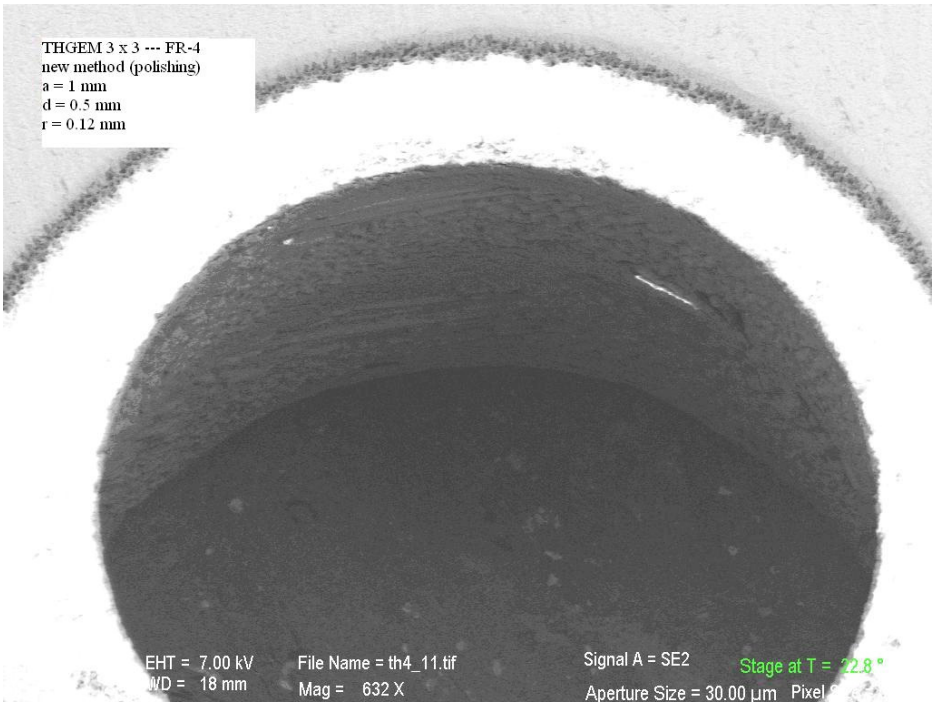

***Fig 1.6**. SEM image of 3x3 THGEM produced with the new method (polishing) and FR-4 as insulator material (a = 1 mm, d = 0.5 mm, h = 0.12 mm, t= 0.4 mm)*

Chapter 2 - Measurements

2.1 General studies on THGEM

In order to optimize and study the performance of the THGEM-based detector, operated in different gases, we irradiated the 3 x 3 cm^2 prototype with soft x-ray source (5.9 KeV). Gain and energy resolution were investigated with soft x-rays for different detector configurations and parameters.

Detector Assembly

The detector, based on THGEM, was located within a stainless-steel vessel, 17 cm in diameter, having a 50 μm thick Mylar windows glued to the stainless steel with epoxy (Fig 2.1). The detector assembly was composed of a mesh drift cathode, two standards FR-4 made THGEMs in cascade and a mesh anode (Fig. 2.2). The THGEMs used for our experiments have holes with diameter between 0.3 - 1 mm displayed in a hexagonal pattern, with 0.1 mm rim around the holes and a pitch between 0.7 – 1.5 mm; table 2.1 summaries the geometries described in this work.

The conversion gap above the first THGEM multiplier was 10 mm wide while the transfer and induction gaps were respectively of 2 and 1 mm. The high voltage was supplied to individual THGEM electrodes through a 15 MOhm serial resistor to limit eventual discharge currents.

The effective THGEM gain was determined measuring pulse-heights, with a charge-sensitive preamplifier (Canberra model 2006, with a sensitivity of 100 mVolt/pC): the signals were read out directly from the bottom electrode of THGEM 2. The output of the preamplifier was further processed through a linear amplifier (Ortec - 571) and multi-channel analyzer (Amptek, MCA-8000).

Geometry #	Thickness t (mm)	hole diameter d (mm)	pitch a (mm)
1	0.4	1.0	1.5
2	0.4	0.3	0.7
3	0.4	0.6	1.2
4	0.4	1.0	1.8

Tab 2.1. THGEM geometries and parameters

A uniform flow (i.e. Ar/CH_4, (95:5) or pure Ar) into the chamber is guaranteed by two gas inlet and one gas outlet for the connection to the gas system. The spacers had some holes to allow free gas flow inside the detector assembly.

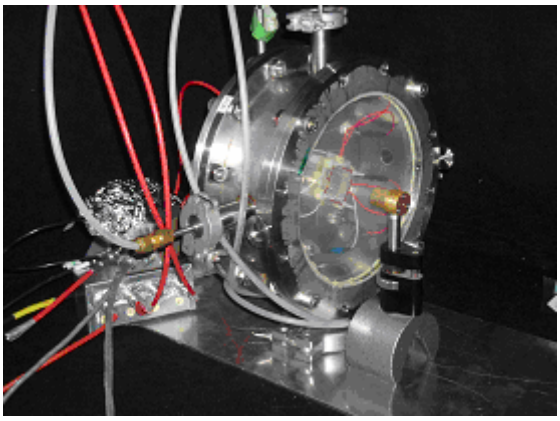

Fig 2. 1. *Picture of the THGEMs detector*

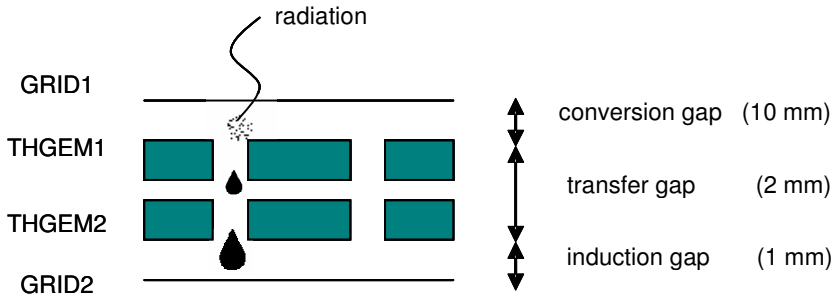

Fig 2.2. *Schematic draw of the double-THGEM detector assembly*

The THGEM electrodes, the cathode and the anode, were biased with independent high-voltage power supplies through 20 MΩ resistors in series and the signals were read through decoupling capacitors (fig. 2.3). A current limit of 50 nA was usually set on the power supplies biasing the THGEMs (CAEN, model N471A). Drift-field and transfer-field values were set up to 1 kV/cm and 3.5 kV/cm, respectively. For gain measurements we applied a slightly reversed induction field (-1 kV/cm) for full electrons' collection, while for imaging and optimization we applied an induction field of 4.5 kV/cm.

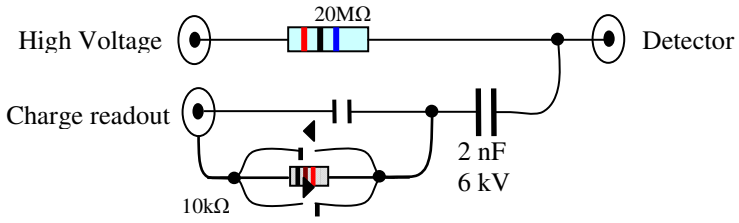

***Fig 2.3**. Power and readout circuit*

Calibration of the Electron Chain

The analysis in this work was done in pulse-counting mode, i.e. analyzing the signals pulse height distribution. The precise knowledge of the ionization signal amplitude for a gas detector is fundamental to determine the absolute effective gain (gas multiplication factor) and therefore to the entire detector performance.

Fig 2.4 shows the electronic circuit used for the calibration of the charge-sensitive preamplifier and for the calibration of the whole electronic chain. It includes a pulse generator and RC circuit (R = 50 Ohm and C = 10 pF) for charge injection, the charge-sensitive preamplifier, the linear amplifier and the multi-channel analyser (MCA).

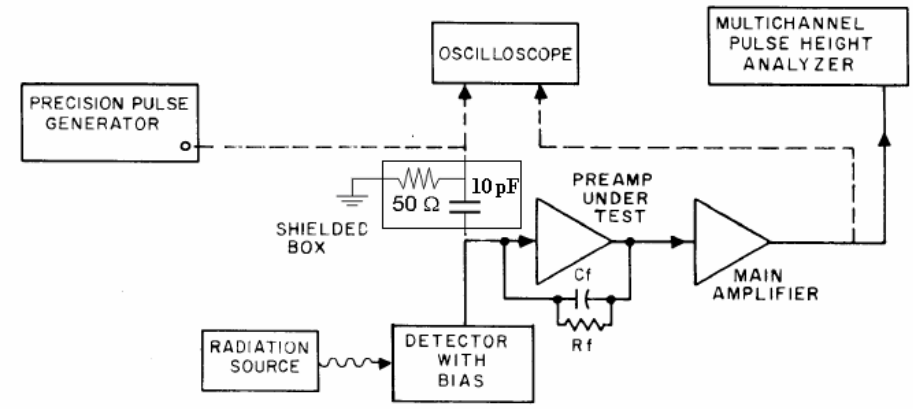

***Fig 2.4.** Measurement of pulse height distribution*

The total charge *Q* injected through the *RC* circuit is equal to the $C \cdot V$ product, were *V* is the amplitude rectangular pulse with a frequency of 50 Hz and width of 1 ms. This circuit acts as a differentiator where the integrated pulse area is proportional to the pulse generator amplitude and therefore proportional to the injected charge.

The user is generally interested in a calibration which allow to determine the energy scale of pulse height distribution and the two parameters have to be determined are the slope and the intercept of calibration line (assuming the analyzer linearity).

The slope, the relation between the inject charge and the corresponding channel number, may be define simply as :

$$n = \frac{Q}{ch} = \frac{C \cdot V}{ch}$$

where ch is the Gaussian pulse height distribution centroid for a given injected charge value. The effective charge gain *G* of a gas detector can be defined by the ratio of the number electrons collected on the anodic electrode *Q* and to the number of primary electrons Q_0 deposited by the incident radiation in the gas conversion gap. If this one is composed of a mono-energetic photon beam, the primary charge created in the conversion gap may be calculated as the ratio between the energy deposited by the incident X-rays *E* and the average energy to produce an electron-ion pair in the gas *W*. So, *G* is defined as

$$G = \frac{Q}{Q_0} \approx \frac{ch \cdot n \cdot W}{E}$$

An ideal MCA would produce a perfectly linear conversion of pulse height to channel number, under this condition, a plot of pulse height versus channel number would be a simple straight line as shown in Fig 2.5 for charge-sensitive preamplifier (ORTEC 124 with a sensitivity of 275 mV/pC), Linear Amplifier (ORTEC 572A, with shaping time of 0.5 μs), MCA (Amptek-800A).

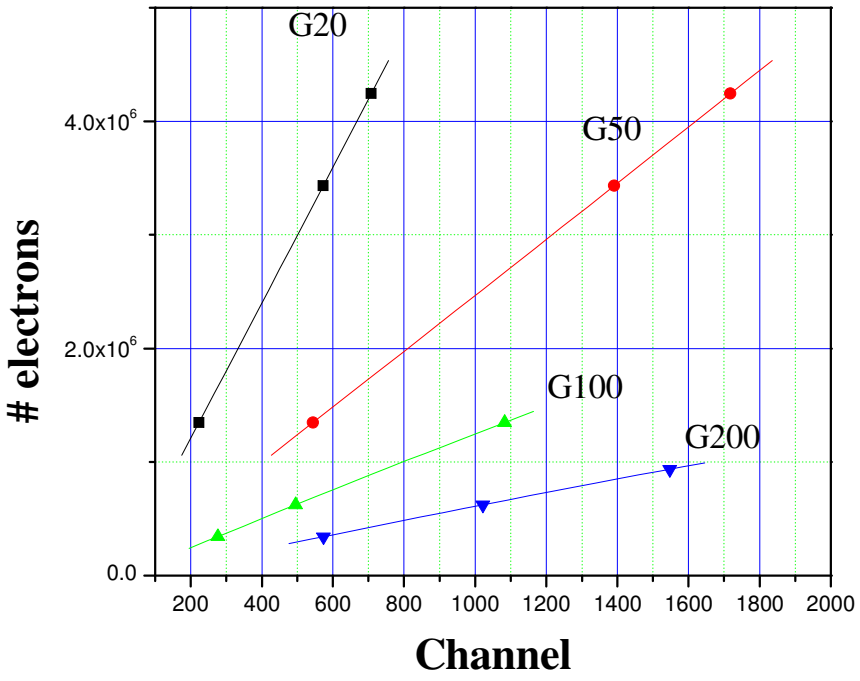

Fig 2.5. *Different MCA calibration plot for different gain amplifier value*

Gain measurements

The effective gain was studied in different gases and in various THGEM geometries by measuring the signal current for various potential differences across the THGEMs electrodes. The set-up of the high voltage supply for 2-THGEMs and 1-THGEM is shown in Fig 2.6 and Tabs 2.2 and 2.3. The ^{55}Fe x-ray source has located in front of the window detector with a collimator with a hole of 1 mm diameter.

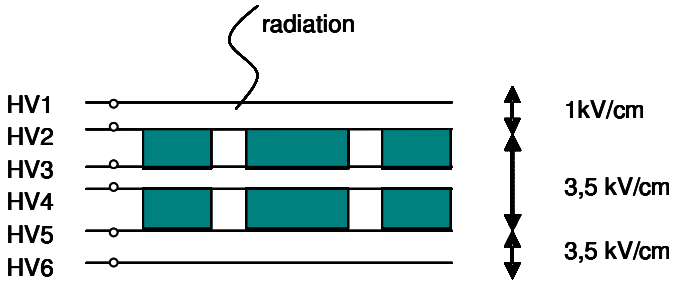

Fig 2.6*. Set up of high voltage supply*

	Voltage (V)
HV1	- V -1700
HV2	-V – 700
HV3	-700
HV4	0
HV5	V
HV6	V + 1500

***Tab 2.2**. Set up Power Supply for 2-THGEMs*

	Voltage (V)
HV1	- V -1000
HV2	-V
HV3	0
HV4	-100
HV5	not connected
HV6	not connected

***Tab 2.3**. Set up Power Supply for 1-THGEM*

The maximum gain value was defined by the onset of the sparks in the holes' rim.

$$Gain = \frac{N_t}{N_i} = e^M = e^{V\alpha}$$

Where N_t is the number of electrons at a given position, N_i is the initial number (230 in Ar/CH_4 gas), M represents the multiplication factor and α is the Townsend coefficient [22] . In Fig 2.7 and 2.8 the gains measured with 2-THGEM of geometry #1 in atmospheric pressure with Ar/CH_4 (95:5) gas and of geometry #2 in atmospheric pressure with pure Argon gas are shown respectively. In Fig 2.9 the gain measured with THGEMs of different geometries and gases at atmospheric pressure is shown.

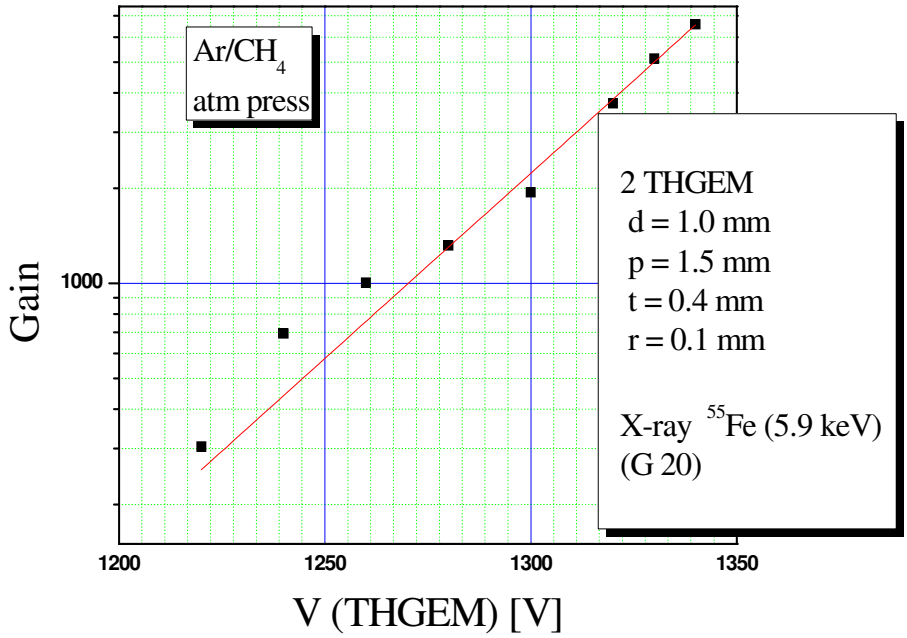

***Fig 2.7**. Gain measured with 2-THGEM of geometry #1 in atmospheric pressure Ar/CH_4 (95:5).*

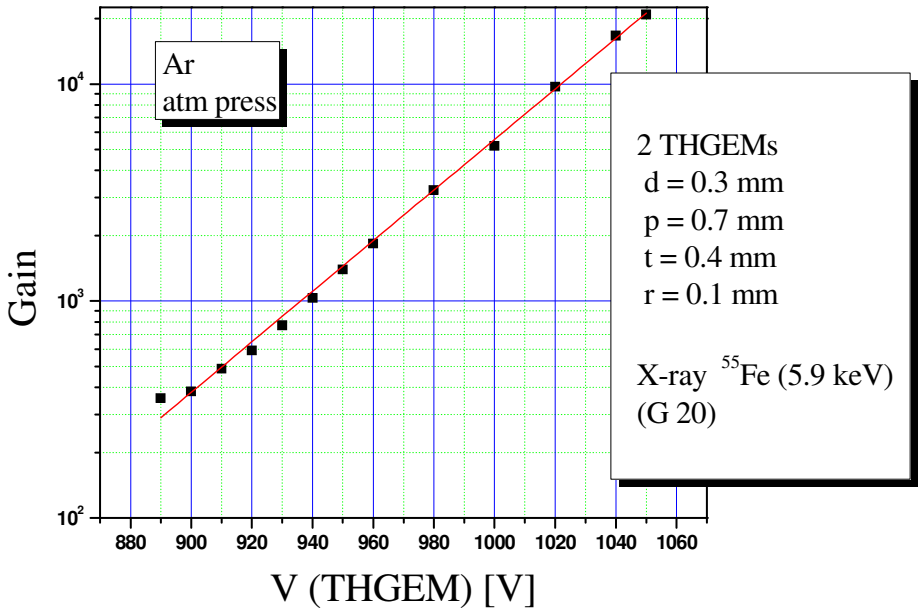

***Fig 2.8**. Gain measured with 2-THGEM of geometry #2 in atmospheric pressure pure Ar.*

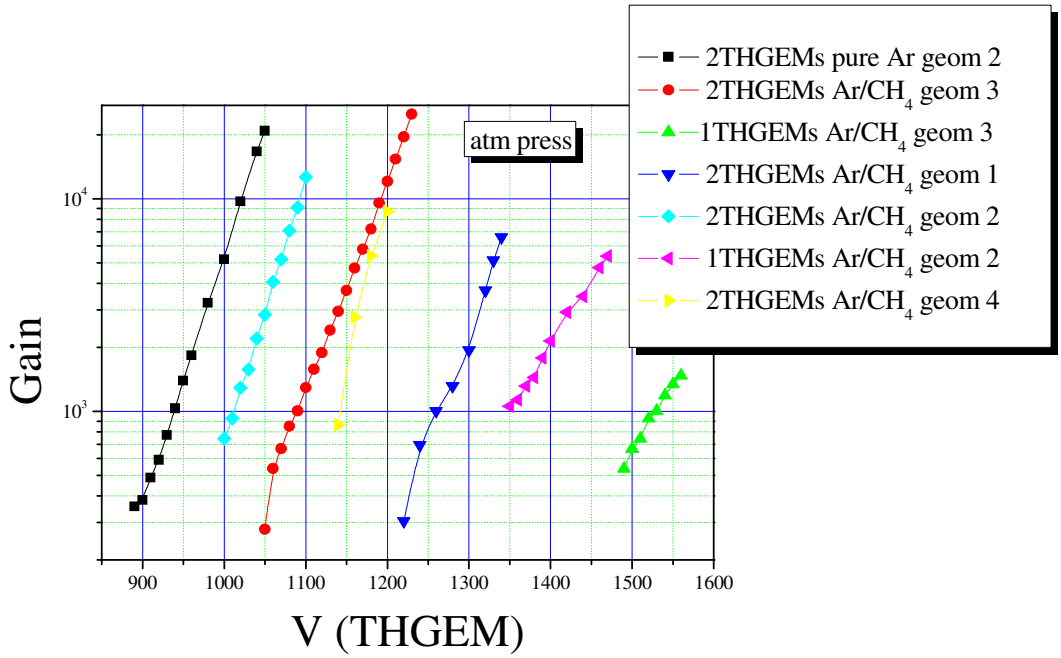

***Fig 2.9**. Gain measured with THGEMs of different geometries and gases at atmospheric pressure. The geometries are defined in Tab. 2.1.*

Energy resolution

The energy resolution of a detector is the ability to distinguish individual lines in the spectrum. Assuming that the formation of each electron is governed by Poisson probability distribution, and if this were the only source of fluctuation in the signal, then the response function of the detector for a mono-energetic lines emitted by the source would have a Gaussian shape. The convention expression for the energy resolution uses the full width at half maximum (FWHM) of the peak:

$$R = \frac{\Delta E}{E} = \frac{FWHM}{peak\_position} = 2.35\frac{\sigma}{peak\_position} = \frac{2.35}{\sqrt{N}}$$

where R is the number of charge carrier and the resolution improves as N in increased.

Measurements of the energy resolution of different radiation detectors have shown that the values for R can be lower by a factor 3 or 4 than the minimum predicted by the statistical arguments. These results would indicate that the processes that give rise to the formation of each

individual charge carrier are not independent, as the number of ways an atom may be ionized is limited by the discrete electron shells, so the total number of charge carriers can not be described by simple Poisson statistics. A measure of these fluctuations is the so-called *Fano factor* and is defined as

$$F = \frac{observed\_variance\_in\_N}{N}$$

because the variance is given by σ^2 , the energy resolution is

$$R = 2.35\sqrt{\frac{F}{N}}$$

Energy resolution of 2-THGEMs based detector, having geometry #2, was assessed using 5.9 keV ^{55}Fe X-ray source in pure Argon, at atmospheric pressure. The full width at half maximum (FWHM) is shown in Fig 2.10. It should be clear that that the smaller the figure for the energy resolution, the better the detector will be able to distinguish between two radiations whose energies lie near each other .

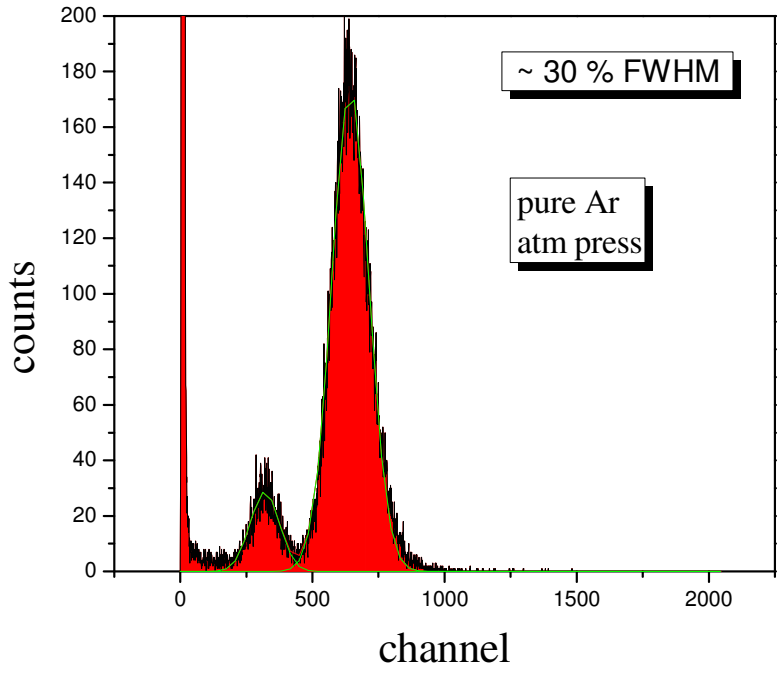

Fig 2.10. *Energy spectrum recorded with 2-THGEM of geometry #2 in atmospheric pressure pure Ar (1040 V – Gain 1.6*10^4)*

Gain vs rim (new method of production)

The relation between maximum gain versus rim size was studied using two 3 x 3 cm^2 THGEMs in cascade. These THGEM were made with the new method of production (Chapter 1). The electrodes had 0.5 mm holes with variable rim sizes (0.04 mm, 0.06 mm, 0.08 mm, 0.12 mm). The conversion gap above the first THGEM multiplier was 11 mm wide while the optimized transfer and induction gap were of the order of 2 mm; the drift, transfer and induction fields were respectively of the order of 1 kV/cm, 3.5 kV/cm and a reversed field of -1 kV/cm. The reversed induction fields permits measuring the collected charge on the last THGEM anode (bottom electrode). The gain response of the detector was investigated using a collimated ^{55}Fe source (5.9 keV X-rays), 1 mm^2 in size. The maximum gain is definite by the onset of the sparks in the holes' rime. Fig. 2.11 shows the maximum gain as function of rim size. As the rim size increased the maximum attainable gain increased exponentially, reaching a value of $3x10^4$ with a rim of the order of 0.12 mm.

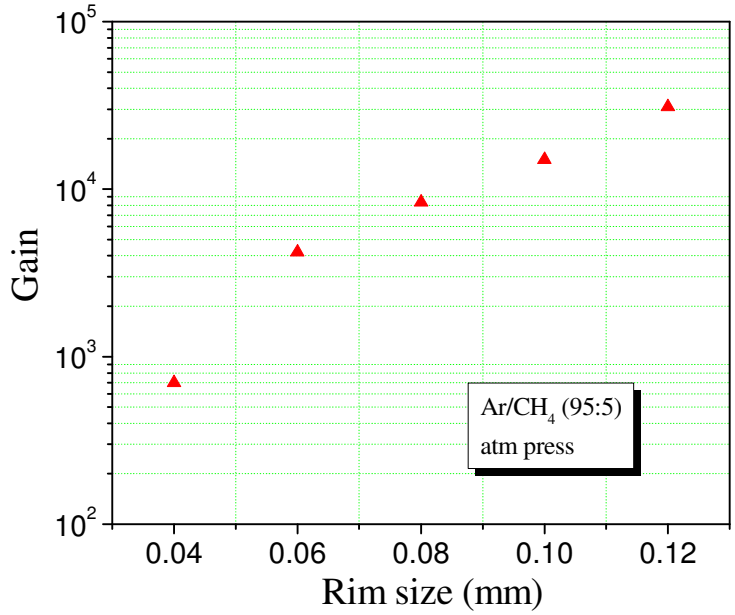

***Fig 2.11**. Maximum attainable gain versus rim size in the THGEM (a = 1 mm, d = 0.5 mm, r =0.04, 0,06, 0.08, 0.1, 0.12 mm)*

2.2 The THGEM imaging detector

Because of production problem with the large THGEM, was not possible to operate on the imaging system. The following section will describe the imaging properties of the THGEM investigated in the past. More details about the x-ray imaging detector and results are shown in [24].

There are two main techniques for signal readout from micropattern detectors. The first one is the use of the induced charge from the metallic readout strips or pads and the second one is the use of the light emission produced by Townsend avalanches'. In the case of the hole- type detector a readout plate is usually placed ~1mm below the detector. To obtain 2D images either a system of strips isolated from each other and oriented perpendicular to each other or pads are used. Recently, very promising results were obtained with a so-called "active pixel" readout – an amorphous silicon thin-film transistors array [25].

The THGEM imaging detector prototype, as shown in Fig. 2.12, consist of a metallized-Mylar drift-cathode foil and two THGEMs coupled in cascade to a resistive anode. A double-sided strip readout electrode is placed behind the resistive-anode plate. Radiation induced electrons are multiplied in a cascade with in the THGEM holes; the resulting charge is collected onto a highly-resistive anode. The moving charge in the induction gap induces a localized signal at a position-encoding readout electrode.

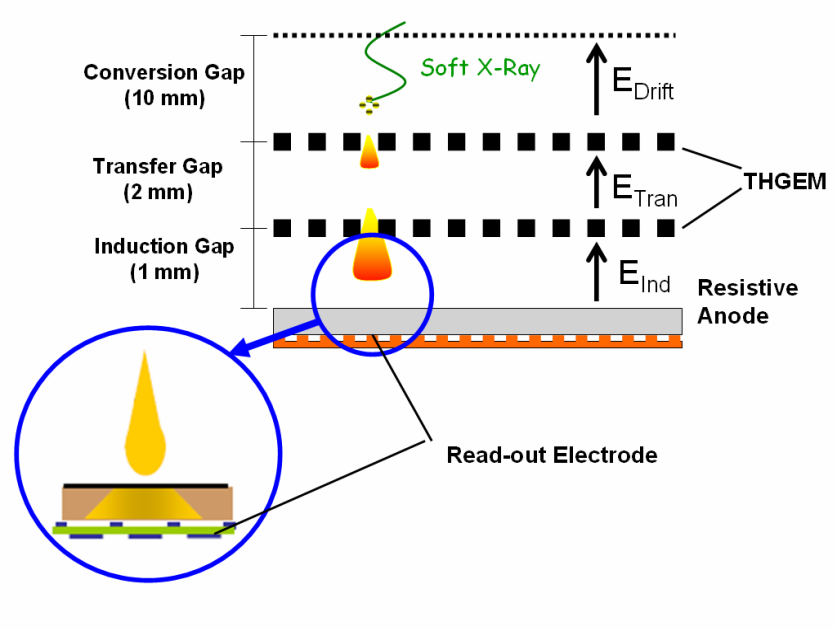

***Fig 2.12**. Schematic view of the double-THGEM imaging detector*

The THGEM electrodes employed in that work have holes of diameter 0.5 mm arranged in a hexagonal pattern, with a pitch of 1 mm; the etched rim around each hole is 0.1 mm. The thickness of the plate is 0.4 mm. The detector was located within a stainless steel vessel, 20 cm in diameter, that incorporates a 50 μm thick Mylar window. It was operated under continuous gas flow, at 1 atmosphere of Ar/CH_4, (95:5); the spacers between electrodes assured efficient gas exchange also in the amplification region. The radiation-conversion and drift gap above the first THGEM multiplier was 10 mm wide, while the transfer and induction gaps were 2 and 1 mm wide, respectively; the drift (E_{drift}), transfer (E_{tran}) and induction fields (E_{ind}) were set at 1, 3.5 and 4.5 kV/cm, respectively. The position readout was realized by induced signal recording through the resistive anode onto a dedicated readout board, using delay-line encoding.

The resistive anode technique allowed for spreading of the induced signal on the readout electrode such that the geometrical size of the induced charge matches the width of the readout-strip pitch. This readout technique also permits for a galvanic decoupling between the multiplication stage and the readout electrode board. Thus, the resistive anode can be operated at high voltage while the readout board is maintained at ground potential. The low-capacitive coupling between resistive anode and readout board also protects the readout electronics from eventual spurious discharges in the detector.

The induced signals were collected on a double-sided X-Y readout electrode, structured with diamond-shape pads printed on both sides of a standard 0.5 mm thick printed-circuit-board (PCB). The pads are interconnected with strips running in orthogonal directions (X and Y) on each of the two board faces, with a pitch of 2 mm. The strips on each side of the board are coupled to a discrete delay-line circuit.

The readout elements are shown schematically in Fig. 2.13. The printed diamond-shaped pads are geometrically designed such that equal charge is induced on both PCB sides and they are non-overlapping in order to reduce the capacitive coupling.

The avalanche location is derived from the time difference between induced signals propagating along the discrete LC delay-line circuit. The latter is composed of 52 LC cells (Fig. 2.14) with an inductance of L=290 nH and a capacitance of C=27 pF per cell; the corresponding delay is 1.4 ns/mm; the total delay for each coordinate is thus 140 ns and the nominal impedance is Z = 103 Ω.

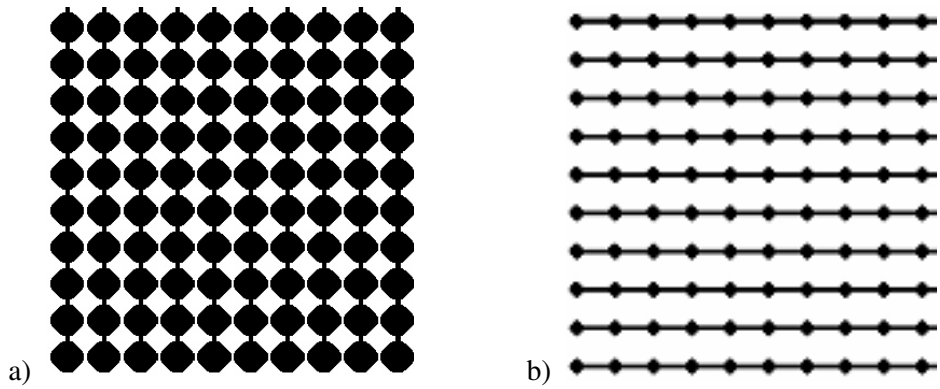

***Fig 2.13**. Example of back (a) and front (b) patterns of a readout test-board*

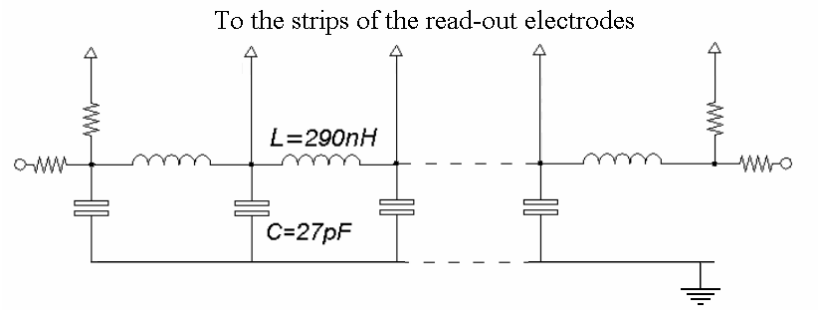

***Fig 2.14**. Schematic view of the readout electrode of the THGEM and the discrete-element LC delay-line circuit*

All THGEM electrodes were biased with independent high-voltage power supplies (CAEN N471A) through 20 MΩ serial resistors. The signals from the electrodes which are not at ground potential were capacitively decoupled from the high voltage. Signals from the electrodes of the second THGEM were fed to charge and current preamplifiers, providing the integrated charge signal and a fast common trigger for the position measurements and for coincidence and TOF experiments. For measurement of the total charge, the electron multiplication factor (gain) and the energy resolution, a charge-sensitive preamplifier (ORTEC 124 with a sensitivity of 275 mV/pC) and a shaping amplifier (ORTEC 572A) were used. A current-sensitive preamplifier (VV44, MPI Heidelberg) and a shaping amplifier (ORTEC 570) were employed for the pulse-shape processing of the 'fast' component of the signals. The pulse-height spectra were analyzed by means of a multi-channel analyzer (AMPTEK MCA8000A).

Fig. 2.15 shows the scheme of the readout electronics of the 100 x 100 mm^2 double-THGEM imaging detector. The data acquisition (DAQ) hardware is based on the 8-channel Time-to-Digital Converter (TDC) chip F1 and the ATMD board [26]. The system also comprises a Charge-to-Time Converter (QTC), based on LeCroy's MTQ300A-chip [27].

This module also permits measuring the avalanche charge behind the last THGEM (after pulse shaping with a Timing Filter Amplifier (TFA)). Events are stored in the PC memory with the corresponding position and time signals.

The signals from the ends of each delay-line and the "common start" signal from the last THGEM cathode were amplified by fast linear amplifiers (VV46, MPI-Heidelberg). The amplified position signals were delayed by 60 ns and fed to an ORTEC CF934 Constant Fraction Discriminator (CFD). The common signal was discriminated by a Canberra 1428 CFD and used as common start for the TDC. The slow (TTL) output of the CFD "enabled" the gate of the ORTEC CFD and allowed valid signals from the delay-lines to pass. The outputs of the CFD were used as "stop" signals for the TDC. The data acquisition software, a modified version of CAMDA [26], calculated the position coordinates and performed a plausibility check on the measured timing signals (comparison of time-sums). Valid data were accumulated in histograms and/or stored as list-mode files in the PC memory.

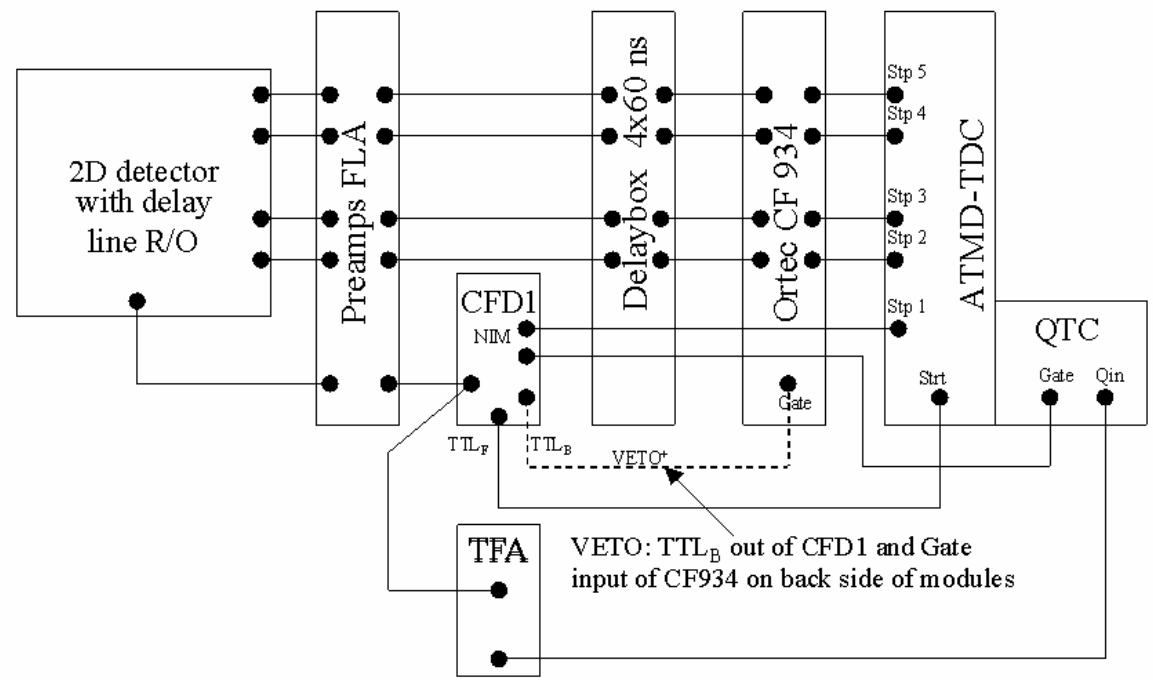

***Fig 2.15**. Schematic view of the DAQ system.*

The result of the digitalization process is an image of 800x800 pixels; each pixel has a linear extension of 125 μm. The images are stored with high dynamic range (4 Byte integers / pixel). However, for visualization of the image on the screen, these high-dynamic-range images were compressed to 8-bit gray-level images.

Chapter 3 - Detector prototype

3.1 Introduction

The goal of the research activity is to develop an imaging system of fast-neutrons (100 keV – 10 MeV) for applications in Boron Neutron Capture Therapy (BNCT). In addition to imaging capability the system should provide the determination of the *neutron spectrum* with *minimum gamma-sensitivity.*

Such detector will provide new and useful information for BNCT research, such as simultaneous determination of neutron spectra with a spatial resolution of centimetres inside a phantom (cylindrical with the dimension of the head) at different depths, from the entrance of the neutron beam. This could be obtained by repeating the set of measurements for the free-in-air measurements behind the collimator, but with phantoms of various thicknesses in front of the spectrometer made of tissue equivalent material. Measurements have to be repeated with increasing slice thickness, up to the phantom height. In such a way, it could be possible to have information about the variations of the neutron spectrum inside the phantom.

Two kinds of detectors were proposed and investigated in this work:

- Fast neutron imaging detector based on detection of recoil protons
- Bonner-type flat imaging neutron spectrometer

The first detector measures only the fast neutron component of the spectrum. It is made of a thin polyethylene (PE) layer for fast-neutron to proton conversion, coupled to two cascaded THGEM and a dedicated read-out electrode. Knock-on protons created by interaction of fast neutrons with hydrogen atoms in PE layer are emitted from PE and are detected by the gaseous THGEM detector.

The second detector consists of a series of variable thickness layers made of moderator/absorber mixture (polyethylene mixed with a neutron absorbing isotope (Li, B)), positioned in front of a slow neutron detector made of a neutron converter foil coupled to two cascaded THGEM and a dedicated read-out electrode (see Chapter 2).

The following section will describe the physical principles behind the two approaches:

3.2 Production and detection of recoil protons by fast neutrons

Neutrons, having no charge and with a mass slightly higher than that of a proton, do not interact directly with electrons but are confined to direct nuclear effects (elastic and inelastic scattering) and nuclear reactions (the absorption of a neutron by the nucleus and the emission of electromagnetic radiation or an energetic particle).

Elastic collisions are billiard ball collisions which result in sharing of kinetic energy of the neutron between the target nucleus and the impacting neutron; thus, leaving a less energetic neutron and a highly energized recoil nucleus. The recoil nuclei quickly become ion pairs and loose energy through excitation and ionization as they pass through the biological material.

The amount of the energy transferred to the nucleus when struck by a neutron increases as the mass of the target approaches that of a neutron.

$$E = E_0\left(\frac{M-m}{M+m}\right)^2$$

where E is the energy of scattered neutron, E_0 is the initial energy of the neutron, M is the scattered nucleus mass and m is the neutron mass. This concept is defined as the law conservation of energy and momentum. Since the neutron is slightly heavier than the proton, the element which closely approximates the mass of the neutron is hydrogen. In neutron-hydrogen collisions the average energy transferred to the hydrogen nucleus is about ½ that of the energy originally contained in the neutron. For incoming neutron ($E_n \ll 931$ MeV, non relativistic kinetic beam energy) conservation of momentum and energy in the center of mass coordinate system gives

$$E_R = E_N \frac{2A}{(1+A)^2}(1-\cos\Theta)$$

where E_R is the recoil nucleus kinetic energy in the lab system, E_N is the incoming neutron kinetic energy in the lab system, A is the mass of target nucleus/neutron mass and Θ is the

scattering angle in the center of mass coordinate system. In Fig. 3.1 the elastic scattering in the laboratory coordinate system is shown $\left(\cos\theta = \frac{\sqrt{(1-\cos\Theta)}}{2} \right)$

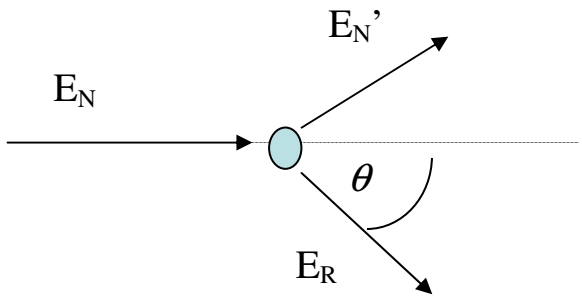

Fig 3. 1*. Schematic view of the elastic scattering in the laboratory system*

the relation for the recoil nucleus energy is

$$E_R = E_N \frac{4A}{(1+A)^2}\left(\cos^2\theta\right)$$

From this last equation we can see that the energy is a function of scattering angle. For example for a head-on collision, with $\theta \approx 0$, the recoil energy is at maximum and if the target is hydrogen the neutron transfers all of its energy.

$$E_{R\max} = E_N \frac{4A}{(1+A)^2}$$

To explain the way in which the recoil energies are distributed between a minimum of zero and a maximum given by this formula, we have to define the probability $P(E_R)dE_R$ to create a recoil with energy dE_R about E_R as

$$P(E_R) = 2\pi \sin\Theta \frac{\sigma(\Theta)}{\sigma_s}\frac{d\Theta}{dE_R}$$

where $\sigma(\Theta)$ is the differential scattering cross section in the center of mass system and σ_s is the total scattering cross section integrated over all angles. Evaluating $d\Theta/dE_R$ and substituting for it we obtain the following equation

$$P(E_R) = \frac{(1+A)^2}{A} \frac{\sigma(\Theta)}{\sigma_s} \frac{\pi}{E_N}$$

A very important simplification holds if $\sigma(\Theta)$ does not change with Θ and is equal to $\sigma_s/4\pi$ (the scattering process is isotropic in the center of mass coordinate system). In case of hydrogen target, that means the expected proton recoil energy distribution is therefore a simple rectangle, extending from zero to the full incident neutron energy, as shown in Fig 3.2 [28].

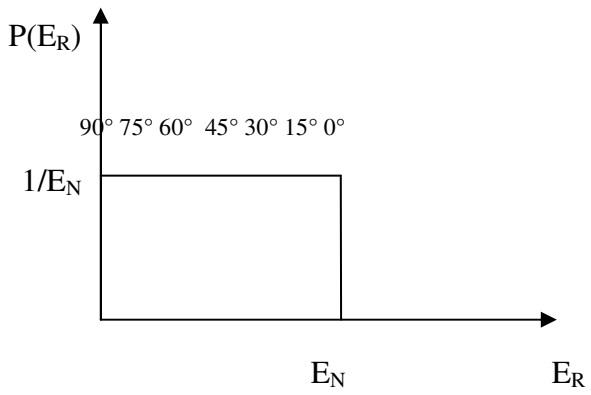

Fig 3. 2*. Energy distribution of recoil proton produced by mono-energetic neutrons. Recoil energies are indicated for various values of the recoil emission angle* θ

As mentioned before the proton recoil detector proposed here will consist of a thin polyethylene (PE) radiator coupled to a gaseous THGEM proton detector. Fig. 3.3 shows energy spectrum of protons emitted from PE foil vs. the energy of the incident neutron energy. The spectrum was calculated using GEANT4 Monte-Carlo simulation program (see Chapter 4). A 1 mm thick layer of PE, with density 0.93 g/cm^3 at room temperature, was placed between mono-directional neutron beams, emitted from a point-like source and a cylindrical detector. The detector was in close contact to the PE layer and the simulation was performed for a wide range (1-19 MeV) neutron energies. 10^7 incident neutrons was used for each neutron energy. As can be observed from Fig. 3.3 the spectrum of the recoil protons emitted by the converter does not have the

characteristic rectangular shape (Fig. 3.2) as one might expect from a hydrogen-rich material; due to the fact that protons lose energy along their path inside the converter because of interaction with the atoms of the converter.

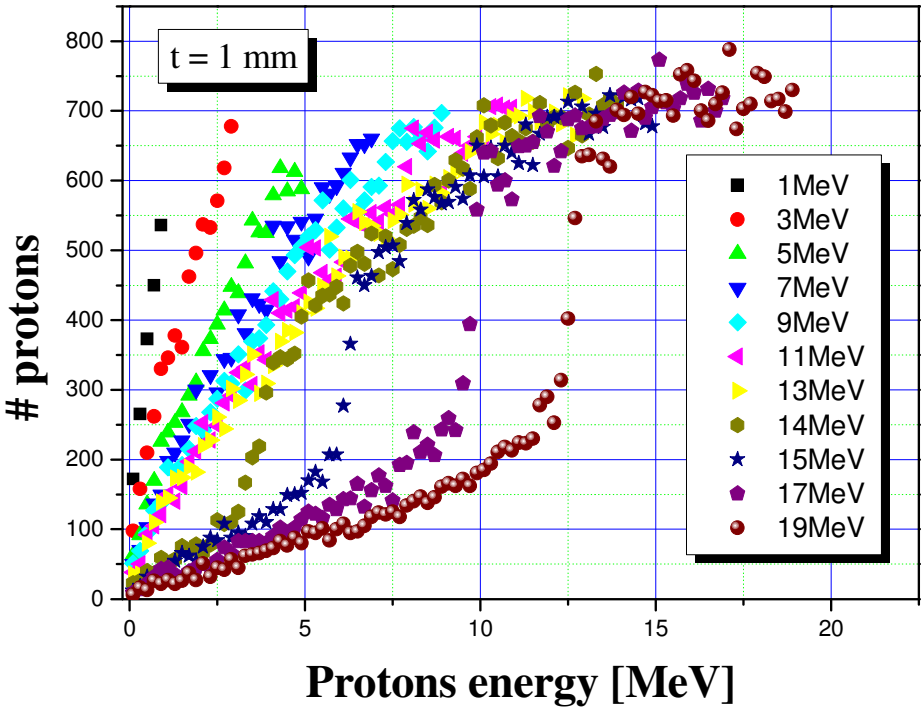

***Fig 3. 3**. Energy distribution of recoil protons for different energy neutron beam (incident number particle 10^7) at 1 mm layer.*

As will be evident from Chapter 4 the efficiency of such detection configuration is rather low and is not suitable for measurement of neutrons below 5 MeV. The second approach described below should permit determination of neutron spectra within a range of 0.1-10 MeV.

3.3 Bonner-type flat neutron spectrometer

Neutron spectrometry and Bonner sphere

Methods of neutron spectrometry can be classified into seven groups based on the principle used to sense or measure neutron energy [29],[30]:

1. nuclear recoil methods, in which the neutron is scattered and the energy of a recoiling nucleus is measured, as in the discovery of the neutron [31];

2. nuclear reaction method, based on measurements of the energies of charged particles released in neutron-induced nuclear reactions, e.g. $^{3}He(n,p)t$ and $^{6}Li(n,\alpha)t$;

3. time of flight methods, in which the neutron velocity is measured;

4. threshold methods, in which a minimum neutron energy is indicated by the appearance of a neutron-induced effect such as radioactivity, a specific gamma-ray energy or a phase transition;

5. the use of "integral" detector (e.g. Bonner Sphere) in which the neutron energy distribution is determined by unfolding a set of readings of detectors (or detector geometries) which differ in the energy-dependence of their response to neutrons;

6. methods based on neutron diffraction;

7. methods in which the time-distribution of the slowing down of a short burst of high-energy neutrons in a suitable medium is measured.

For neutron spectrometry the Bonner sphere spectrometer (BS) is the only system which covers the whole energy range from thermal to GeV neutrons. Bonner sphere sets have been used for decades for the measurement of neutron spectra with neutron energies up to 20 MeV [32].The usual Bonner sphere set consists of six to eight high density polyethylene spheres with diameters varying from 3 to 18 inches. Either a BF_3 counter, ^{6}LiI scintillator or ^{3}He detector is located at the center of each sphere to detect the moderated neutrons. As the reaction cross sections of B, Li, and He with neutrons follow a *1/v* relationship, a thick moderator is needed to slow down the faster neutrons to thermal energies for absorption in the detector materials. The thick moderator however increases the neutron absorption which decreases the response [33]. From the measured reading of a set of spheres, information can be derived about the spectrum of neutron field in which the measurements were made. The derivation of this spectral information is not simple, and the validity of BS results has often been questioned. An other disadvantage from this method is the poor energy resolution, which does not allow appreciating fine structures as narrow peaks and the weight [34]. The new idea is to have spatial information with energy resolution for a more complete beam characterization. The results of Monte Carlo

calculations are shown in Chapter 4. Provided a well-established response matrix and adequate irradiation conditions the most delicate part of the BS-based spectrometry is the unfolding process. Many computerized BS unfolding codes have been developed, whose critical points are, in general, the complexity of the codes, the need of a very expert user and the need of realistic a priori information, such as a ‘‘default spectrum’’ as close as possible to the spectrum to be obtained.

The reading C_i of the thermal neutron sensor inside the i-th Bonner sphere, when exposed in a point of a neutron field, can be expressed as

$$C_i = \Phi \int_{E_{min}}^{E_{max}} R_i(E)\varphi(E)dE$$

where Φ is the neutron fluence in cm^{-2}, $R_i(E)$ is the response function of the sphere (in cm^2). It is usually derived with Monte Carlo calculations and represents the reading per unit fluence as a function of the mono-energetic neutron energy, *E*. The set of response functions for all Bonner spheres forms the ‘‘response matrix’’. φ(E) is the energy distribution of the neutron fluence normalized to $1/cm^2$ and its unit is MeV^{-1}.

The energy distribution of the neutron fluence is given by $\Phi_E = \Phi\varphi(E)$ and its unit is $cm^{-2}MeV^{-1}$. When a set of *m* Bonner spheres is exposed to the same neutron fluence, a set of readings C_i, $i = 1,\ldots m$, is collected. The neutron fluence Φ and its energy distribution φ(E) may be derived by inverting a set of m equations, which for computer calculation purposes can be expressed in the following discrete form:

$$C_i = \Phi \sum_{j=1}^{N_g} R_{ij}\varphi_j \Delta E_j \qquad j = 1, \ldots, m$$

where N_g is the number of energy groups. The unfolding problem in BS spectrometry is under-determined, i.e. the number of unknown is largely higher than the number of independent

measurement ($N_g > m$). This implies that a set of solution could satisfy the previous equation and this ambiguity may be extremely hard to notice in complicated problems [35].

Detector prototype

The principle proposed in our project is very similar to the Bonner sphere, but instead of spheres we use a set of flat plates with different thickness. The detector consists of a series of variable thickness layers made of moderator/absorber mixture (polyethylene mixed with a neutron absorbing isotope (Li, B), positioned in front of a slow neutron detector made of a neutron converter foil coupled to two cascaded THGEM and a dedicated read-out electrode as shown in Fig. 3.4 below.

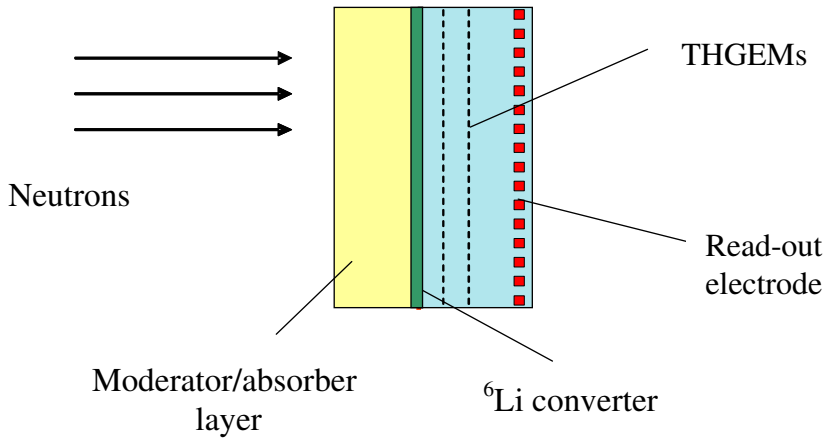

Fig 3. 4. *Schematic view of the proposed imaging system set-up*

The idea of the addition of an absorber dopant material to the moderator block, is to reduce the diffusion length of thermal neutrons during the path inside the layer. For the first study of the method it was decided to use pure ^{6}Li as absorber in the moderator and a metallic ^{6}Li converter foil (see Chapter 4). The cross section for the ^{6}Li(n,α)t reaction is shown in Fig. 3.5. For an optimal choice of the converter foil material, some properties should be considered. In order to achieve a high detection efficiency with minimum foil thickness, a large neutron cross section in needed. The range of the neutron-induced charge particle should be large compared with the converter foil thickness and is it desirable to have a large secondary electron emission from the

foil to the volume for the high operation stability and an optimal imaging performance. Another important characteristic, is the low gamma sensitivity of the material [22] .

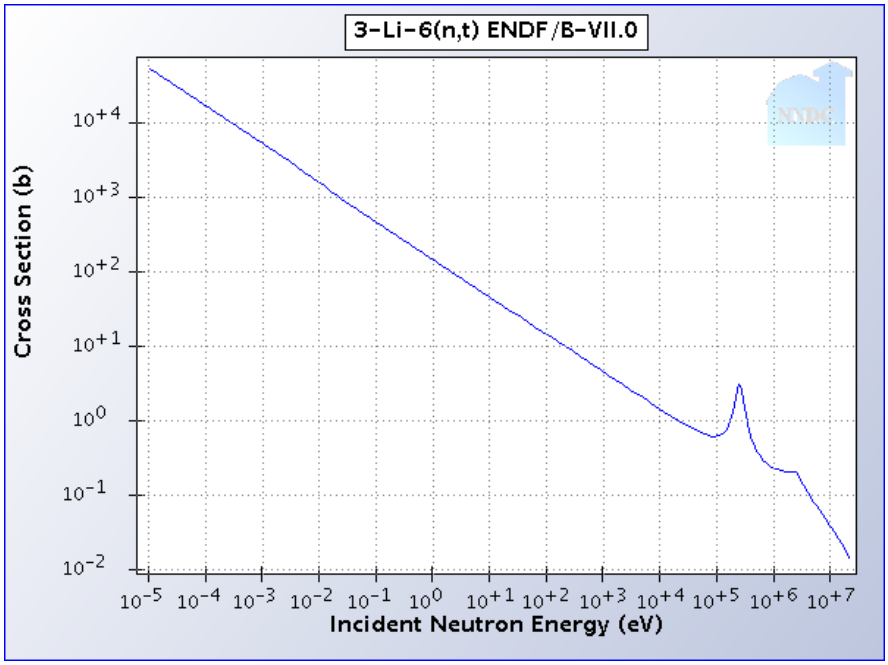

***Fig 3. 5**. Neutron cross section of ^{6}Li(n,t)α reaction from ENDF/B-VII.0*

After the moderation inside the layer, the neutrons reach the solid foil and convert into charged particles which can leave the foil surface and produce slow electrons in the gas, just in the vicinity of this escaping point. ^{6}Li has the advantage that no γ are emitted after the neutron capture and that triton and α are densely ionizing particles. The efficiency of such a detector is given by the escape probability of at least one of the charged particles into the gas which is defined by the balance between the absorption length μ for neutrons (depending on the neutron wavelenght λ) and the range r of the charged particles in the foil material. The triton produced in the ^{6}Li(n,t)α reaction has an energy of E = 2.74 MeV which in metallic Li results in a range of r = 0.132 mm while for the α-particle E = 2.05 MeV and r = 0.022 mm. The particles escaping from the converter foil produce about 70 (α) and 250 (t) low-energy secondary electrons across the 2 mm of the preamplification gap, between the foil and the THGEMs, which is sufficient for 100% detection efficiency [36]. In fig. 2.6 is shown the calculated

probability of a triton emission for incoming neutron versus the foil. In this experiment, the particles are detected on both sides.

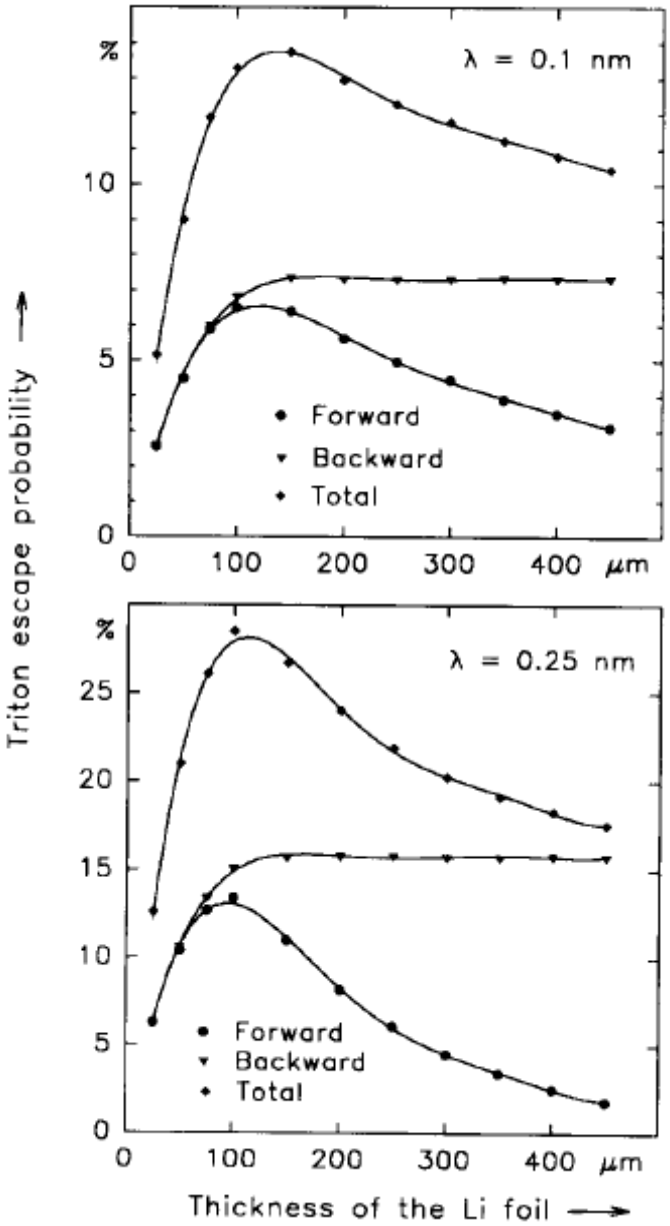

Fig 3. 6*. Calculated triton escape probabilities versus thickness of a ^{6}Li converter foil for neutrons of wavelength l = 0.1 nm and l = 0.25 nm [36]*

Unlike the neutral radiations (i.e. neutrons and gamma/X-rays), the charged particles (alpha particle, fission fragments, protons, deuterons, tritons, and μ and pi mesons) interact with matter

primarily through the Coulomb interaction between their positive charge and the negative charge of electrons in the absorber atoms [28].

Upon entering any absorbing medium, the charged particle immediately interacts with many electrons. The energy that is transferred to the electrons must come at the expense of the charged particle, and its velocity therefore decreases, as a result of the encounter, until the particle is fully stopped.

Because of the small, gradual amount of energy transferred from the ion to the absorbing material, the particle passage may be treated as a continuous slowing down process. Near the end of its track, an ion experiences charge exchange between the absorber, and picks up electrons until it becomes a neutral atom. The range of the α-particle (E = 2.05 MeV) and triton (E = 2.5 MeV) in pure Argon gas is 11 mm and 56 mm respectively, as calculated using [37].

The energy loss per unit distance, the *stopping power (S=-dE/dx),* depends on the type and energy of the particle and on the material. Usually, the energy loss per unit distance increases while the particle slows down. The classical expression that describe the energy loss, known as *Bethe-Bloch formula,* is

$$-\frac{dE}{dx} = \frac{4\pi\ e^{4} N_A}{m_0}\frac{z^2}{v^2} Z \quad \left[\ln \frac{2\pi\ m_0\ v^2}{I} \quad - \quad \ln\left(1-\beta^2\right) - \beta^2 \right]$$

where v and ze are the velocity and charge of the primary particle, N and Z are the number density and atomic number of the absorber atom, m_0 is the electron mass and e is the electronic charge. β is the ratio v/c and the parameter $I = h\langle\nu\rangle$ represents the average excitation and ionization potential of the absorber. For non-relativistic charged particles (v<<c), only the first term in the brackets is significant. The equation is generally valid for different types of charged particles provided their velocity remains large compared with the velocities of the orbital electrons in the absorbing atoms. The variation in the energy loss for a number of different charged particle is shown in Fig. 3.7 over a wide energy range. This graph shows that the value of *dE/dx* for many different types of charged particles approaches a near-constant broad minimum value at energies above several hundred MeV, where their velocity approaches the velocity of light.

A plot of the energy loss along the track of a charged particle such as that shown in Fig. 3.8, is known as a *Bragg curve.* This plot is for an alpha particle of 5.9 MeV in air.

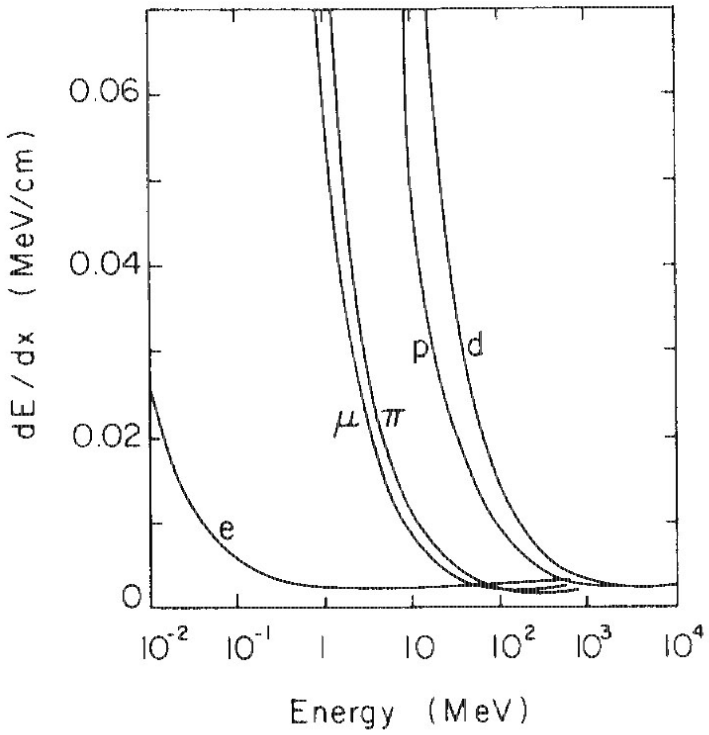

Fig 3. 7*. Variation of energy loss in air versus energy of charged particle shown.*

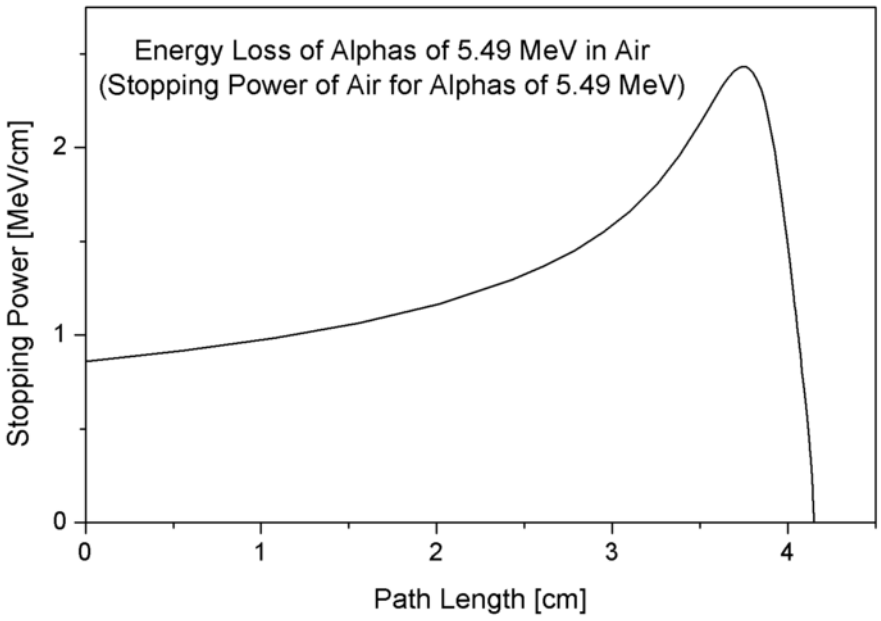

Fig 3. 8. *The energy loss of alphas particle of 5.49 MeV in air*

Chapter 4 - Monte Carlo Simulation

In order to develop an imaging system of fast-neutrons (100 keV – 10 MeV) for applications in BNCT, we present a summary of the simulation activities using GEANT4 and MCNP4c-5 codes. The work was focused to provide a solution to determinate the fast neutron spectrum (and dose) with some position sensitivity.

4.1 Introduction

The systematic development of Monte Carlo methods has its origin in the work at Los Alamos and dates back to about 1944. The method is based on the generation of random numbers and is named after the city in the Principality of Monaco famed for its roulette casinos. It is nowadays a commonly used tool for solving complex mathematical equations arising in modelling problems in many fields. In radiation physics, the Monte Carlo method is used mainly for solving the Boltzmann transport equation.

Solving the Boltzmann transport equation, individual particles are followed when they interact with the medium in the same manner as in the physical world. Their interaction at each positions are determined using random numbers and the probability functions for interaction. A new energy and new direction of motion are sampled after each interaction. A particle is followed until it reaches an energy which makes the impact on the quantity scored negligible. The building blocks of a Monte Carlo code are a random number generator, a physical model of the various steps in particle transport, and the probability distributions of the variables used in the models. The rest is geometrical transformations and scoring of the quantities of interest[38].

4.2 MCNP

The MCNP Code is the internationally recognized code for analyzing the transport of neutrons and gamma rays (hence NP for *neutral particles*) by the *Monte Carlo* method (hence MC). The code deals with transport of neutrons, gamma rays, and coupled transport, i.e., transport of secondary gamma rays resulting from neutron interactions. The MCNP code can also treat the

transport of electrons, both primary source electrons and secondary electrons created in gamma-ray interactions [39].

The neutron energy regime is from 10-11 MeV to 20 MeV for all isotopes and up to 150 MeV for some isotopes, the photon energy regime is from 1 keV to 100 GeV, and the electron energy regime is from 1 keV to 1 GeV. The capability to calculate k_{eff} eigenvalues for fissile systems is also a standard feature. The user creates an input file that is subsequently read by MCNP. This file contains information about the problem in areas such as: the geometry specification, the description of materials and selection of cross-section evaluations, the location and characteristics of the neutron, photon, or electron source, the type of answers or tallies desired, and any variance reduction techniques used to improve efficiency [8].

MCNP is a code undergoing continuous development at Los Alamos National Laboratory and has periodic new releases. The version used in this work is 4c. The code and instruction manual are distributed by the Radiation Safety Information Computational Center at Oak Ridge National Laboratory (http://www-rsicc.ornl.gov/).

4.3 GEANT4

Geant4 is a free software package composed of tools which can be used to accurately simulate the passage of particles through matter. All aspects of the simulation process have been included in the toolkit (the geometry of the system, the materials involved, the fundamental particles of interest, the generation of primary events, the tracking of particles through materials and electromagnetic fields, the physics processes governing particle interactions, the response of sensitive detector components, the generation of event data, the storage of events and tracks, the visualization of the detector and particle trajectories and the capture and analysis of simulation data at different levels of detail and refinement). At the heart of Geant4 is an abundant set of physics models to handle the interactions of particles with matter across a very wide energy range. Geant4 is written in C++ and exploits advanced software-engineering techniques and object-oriented technology to achieve transparency. These ideas first appeared in two studies done independently at CERN and KEK in 1993. Both groups sought to investigate how modern computing techniques could be applied to improve the existing FORTRAN based Geant3 simulation program. Activities were merged in the fall of 1994 and a formal proposal, RD44, to construct an entirely new program based on object-oriented technology was submitted to

CERN's Detector Research and Development Committee. The initiative grew to become a large international collaboration of physicist programmers and software engineers from a number of institutes and universities participating in a range of high-energy physics experiments in Europe, Japan, Canada and the United States. The objective was to write a detector simulation program which had the functionality and flexibility necessary to meet the requirements of the next generation of subatomic physics experiments. The collaboration now profits from the accumulated experience of many contributors to the field of Monte Carlo simulation of physics detectors and physical processes [9].

4.4 GEANT4 evaluation

In order to evaluate the accuracy of GEANT4 and to get practice of its formalism, we performed some preliminarily tests. In details, the goal of these tests was to obtain a comparison between the mass attenuation coefficient and neutron cross section obtained from GEANT4 simulations, with the ones published in the literature (NIST database [40]). The *world* geometry used for the simulation is shown in Fig 4.1.

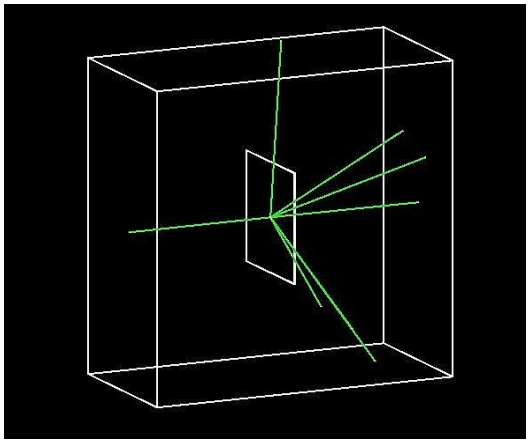

Fig 4.1. *World geometry with layer and sphere sensitive detector and incident neutron particle beam (GEANT4 Wired output file)*

A thick layer of Copper, with density 8.96 g/cm^3 at room temperature, was placed between a mono-energetic and mono-directional photon beam, emitted from a point-like source, and small detector. The dimensional of the sphere detector is 0.1 mm radius and is placed far away from the Cu layer such that we can consider the system as a “good geometry” one (we detected only the particle which did not interact in the layer, according to the mass attenuation coefficient definition). The simulation with different gamma energy and thickness are show in Tab 4.1.

The attenuation coefficients μ was obtained from the following equation:

$$\mu = \frac{1}{x} \ln \frac{I_0}{I}$$

where x is the thickness of the layer, I_0 is the number of incident particles and I is the number of detected particles.

Energy [keV]	**n detected**	**thickness** [mm]	**μ/ρ (NIST)** [cm2/g]	**μ (NIST)** [cm-1]	**μ (GEANT4)** [cm-1]	**err** %
50	390989	0.4	2.613	23.41	23.48	0.3
	95502	1			23.49	0.3
100	84581	0.4	0.4584	4.11	4.10	0.2
	633117	1			4.11	0.0
150	820167	1	0.2217	1.986	1.982	0.2
200	945983	0.4	0.1559	1.396	1.389	0.5
	571467	4			1.393	0.2
	870007	1			1.398	0.1

***Tab 4.1**. Results of different energy gamma incident beam (10^6 particles) simulation with Copper layer at different thickness to compare coefficient attenuation with literature.*

As shown in Tab. 4.1, the μ values calculated through the GEANT4 simulations were compared with the NIST data and the discrepancy are less then 0.5% for the Cu. We repeated the same simulations for Aluminium, Hydrogen and Carbon layer as shown in Tabs 4.2.

Energy [keV]	**n detected**	**thickness** [mm]	**μ/ρ (NIST)** [cm2/g]	**μ (NIST)** [cm-1]	**μ (GEANT4)** [cm-1]	**err** %
200	876352	4.0	0.1223	0.33	0.33	0.0

***Tab 4.2.a**. Results of 200 keV energy gamma incident beam (10^6 particles) simulation with Aluminium layer with different thickness to compare coefficient attenuation with literature.*

Energy [keV]	**N detected**	**Thickness** [mm]	**μ/ρ (NIST)** [cm2/g]*10-3	**μ (NIST)** [cm-1]*10-3	**μ (GEANT4)** [cm-1]*10-3	**err** %
50	996978	1	0.335	0.031	0.03	3.2
	969902	10			0.031	0.0
100	997326	1	0.294	0.026	0.027	3.8
	973689	10			0.0266	2.3
150	997535	1	0.265	0.024	0.025	4.2
	976339	10			0.02	0.0

***Tab 4.2.b**. Results of different energy gamma incident beam (10^6 particles) simulation with Hydrogen layer at different thickness to compare coefficient attenuation with literature.*

Energy [keV]	**N detected**	**Thickness** [mm]	**μ/ρ (NIST)** [cm2/g]	**μ (NIST)** [cm-1]	**μ (GEANT4)** [cm-1]	**err** %
50	958542	1	0.187	0.42	0.42	0.0
100	966353	1	0.151	0.34	0.34	0.0
150	969933	1	0.265	0.31	0.31	0.0
200	972620	1	0.123	0.28	0.28	0.0

***Tab 4.2.c**. Results of different energy gamma incident beam (10^6 particles) simulation with Carbon layer at different thickness to compare coefficient attenuation with literature.*

We used the same geometry to calculate the microscopic neutron cross section σ . This is defined as the probability per nucleus that a neutron beam interact with the nucleus and is measured in barns (1b = 10^{-24} cm^2). The macroscopic cross section Σ takes into account the number of nuclides present and the expression is $\Sigma = N\sigma$. So σ is calculated as

$$\sigma = \frac{1}{x}\ln\left(\frac{I_0}{I}\right)\frac{1}{N}$$

Initially we obtained results not comparable with literature (i.e. error 60% for simulation with 1 MeV neutron incident beam and Hydrogen layer of 1 mm thickness). We changed the *hadronic physics list* source and then we compared GEANT4 σ values with ENDF data**,** the discrepancies are less then 1% (see Tabs 4.3). Hadronic physics is notoriously a very broad and difficult field. The only current viable approach, in these cases, is to use different simplified models, whose approximated validity is often restricted to particular incident particles, target material types, and interaction energies. By using a proper set of these models it is often possible to cover different regions of interest. In GEANT4 a large set of hadronic models are available, and the user can choose and combine them according to her/his needs, in terms of application, precision, and computing time [41].

Energy [MeV]	**N detected**	**Thickness** [mm]	**σ (ENDF)** [barn]	**σ (GEANT4)** [barn]	**err** %
1	7582	10	4.24	4.28	1.1
0.1	49	10	12.73	12.65	0.6

***Tab 4.3.a**. Results of different energy neutron incident beam (10^6 particles) simulation with Hydrogen layer at different thickness to compare cross section value with literature.*

Energy [eV]	**N detected** I	**Thickness** [mm]	**σ (ENDF)** barn	**σ (GEANT4)** Barn	**err** %
0.025	36223	0.1	773	778.9	0.8

***Tab 4.3.b**. Results neutron incident beam (10^6 particles) simulation with Boron layer at different thickness to compare cross section value with literature.*

4.5 Efficiency (GEANT4)

The initial proposed detector prototype was made of a polyethylene layer for fast-neutron to proton conversion, coupled to two cascaded THGEM and a dedicated read-out electrode, for a robust, cheap and simple fast neutron spatial detection procedure. The detector should provide an estimation of the fast neutron dose component and its spatial distribution for applications in Boron Neutron Capture Therapy (BNCT). For a good spatial representation of a fast neutron beam, the detector should have high neutron detection efficiency and low sensitivity to gamma rays; thus one has to find a compromise between neutron efficiency and gamma sensitivity, optimizing the radiator converter geometry according the neutron source energy.

We employed a simulation program to detect proton. A layer polyethylene (PE), with density 0.93 g/cm^3 at room temperature, is placed between mono-directional neutron beam, emitted from a point-like source, and a cylinder detector. This one is closer to the layer and is 0.1 mm thickness. We simulated different energy neutron incident beam (10^7 particles) with layer at different thickness. A schematic view is shown in Fig. 4.2. The thickness of the converter must be a compromise between the requirement of a thick converter for high neutron absorption and the limited escape length for protons recoil from PE (hydrogen-rich material).

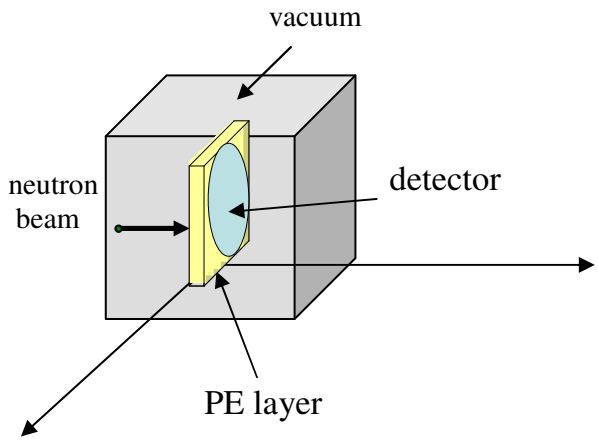

***Fig 4.2**. Schematic view of the geometry to simulate the performance of the neutron/proton converter, using different energy neutron incident beam (10^7 particles) with different thickness of the layer.*

The efficiency of a device based on recoil proton or other ones can be calculated from the scattering cross section σ_s. The conversion efficiency for the fast neutron component using a hydrogen-rich converter may be expressed as

$$Efficiency = \varepsilon\left(1 - \exp\left(-n_v x \sigma_s\right)\right)$$

where ε is the fraction of proton coming out of the layer, x is the thickness of the layer, n_v is the atomic density of the converter and σ_s its neutron elastic scattering cross-section. The total conversion efficiency depends on the energy spectrum of the primary neutron beam and the converter thickness[28]. The efficiency for different value of energy neutron beam and thickness is shown in Fig 4.3.

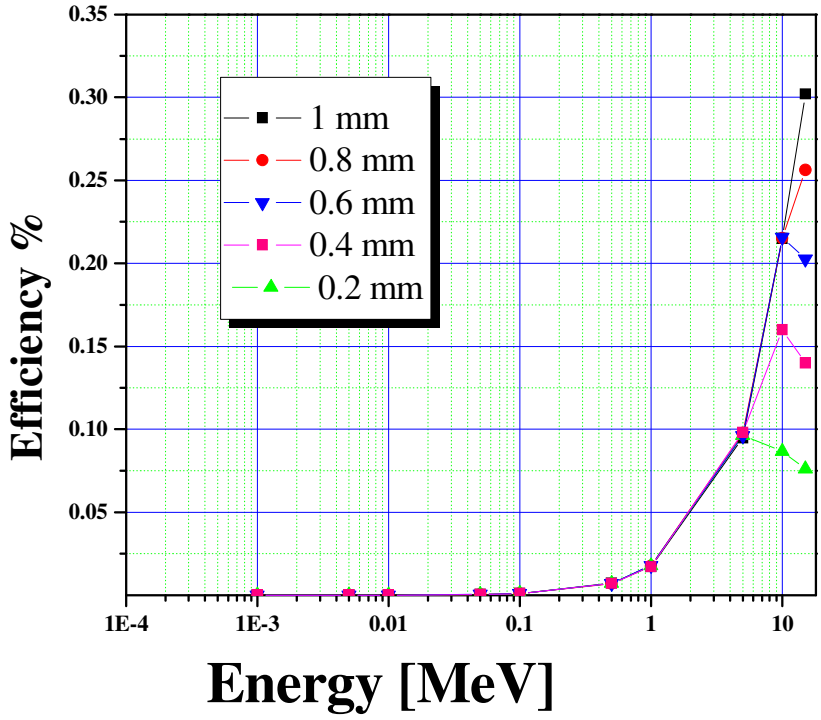

***Fig 4.3**. Efficiency % for different value of energy neutron beam (incident number particle 10^7) and layer thickness*

We know that for 1 mm thick converter the calculated efficiency with 5 MeV neutrons was around 0.2 %. This is for calculation and optimization of the radiator converter efficiency in the FANGAS (a neutron-counting detector based on a solid neutron converter coupled to a gaseous electron multiplier (GEM) developed by V. Dangendorf et al.), performed with GEANT4 [42]. The performance of the converter, in terms of neutron to proton conversion, obtained from our GEANT4 simulations, increase with the thickness of the converter (Fig 4.4). More precisely, as the energy of the primary neutron beam increases the most efficient converter's thickness increases. The drop of the conversion efficiency is pretty undersized for all the neutron energy. In conclusion, the thicker is the converter the better is the conversion efficiency, but only for neutron energy > 5 MeV.

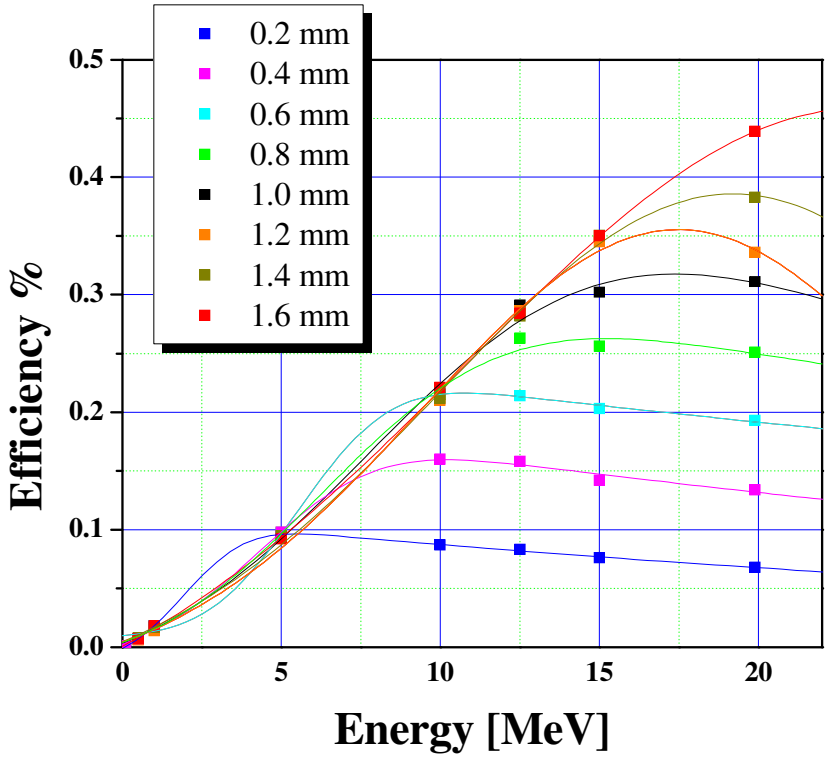

***Fig 4.4**. Efficiency % for different value of energy neutron beam (incident number particle 10^7, from 100 keV) and layer thickness*

Fig 4.5 shows the calculated detection efficiency vs converter thickness for different incident neutron energies. Neutron efficiency, for high energy neutron beam, initially increases with converter thickness, but then tends to saturate when the thickness approaches the proton range in the material. The range of lower energy protons (< 5 MeV) in polypropylene is shorter than the minimal thickness employed in this simulation, thus the efficiency is already saturated [43].

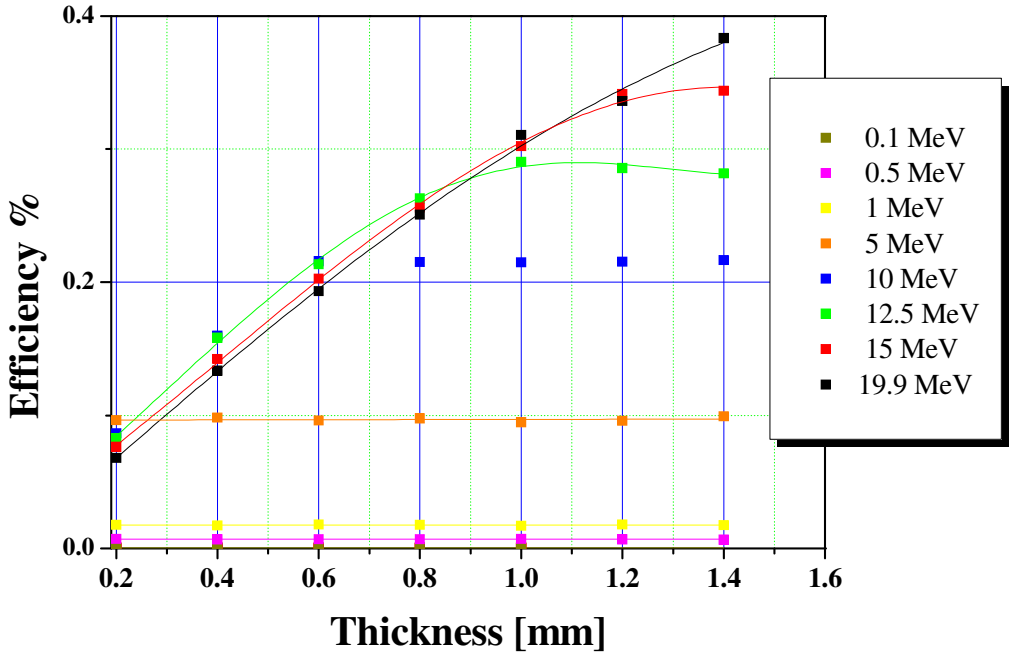

***Fig 4.5**. Efficiency % for different value of layer thickness (incident number particle 10^7, from 100 keV) and energy neutron beam*

4.6 GEANT4 vs MCNP

Since the neutron energy range of interested is from 100 keV to 10 MeV, a new idea to provide a solution to determine the neutron spectrum (and dose) in the energy range of interest together with some position sensitivity was proposed. The description of the proposed detector prototype is in Chapter 3.

We employed a simulation program to check the GEANT4 physics. A Polyethylene + 10% ^{6}Li mixture (density 0.883 g/cm3 at room temperature) and a ^{6}Li foil were positioned in front of a mono-directional neutron beam at different energies (0.1, 1, 5, 10 MeV), emitted from a point-like source. A schematic view is shown in Fig. 4.6. We followed the particles inside the materials and we compared the range of alpha (En = 1.96 MeV) and triton (En = 2.6 MeV) inside ^{6}Li foil. Tab 4.4 shows the comparison between SRIM 2006 data and our GEANT4 evaluation.

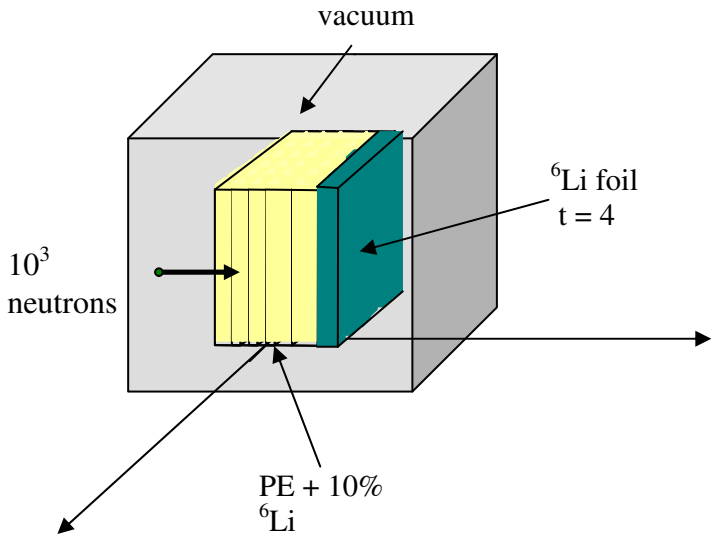

***Fig 4.6**. Schematic view of the geometry set-up to check the GEANT4 physics.*

Particle	Alpha	Triton
	En = 1.96 MeV	En = 2.6 MeV
GEANT4	range ≈ 18.8 μm	range ≈ 127 μm
SRIM 2006	range ≈ 20 μm	range ≈ 130 μm

***Tab 4.4**. Comparison of the range of alpha (En = 1.96 MeV) and triton (En = 2.6 MeV) inside ^{6}Li foil, between SRIM 2006 data and our GEANT4 evaluation.*

In order to validate the GEANT4 results, we compared the MNCP and GEANT4 neutron spectrum at the exit of the moderator/absorber layer (10 mm). A PE+10% ^{6}Li mixture (density 0.883 g/cm^{3} at room temperature) was placed between mono-directional neutron beam (100 keV), emitted from a point-like source, and 10 concentric cylinder detectors. Those ones are closer to the layer, are 0.1 mm thickness and step of 2 mm. Fig. 4.7 shows a schematic view of the geometry set-up.

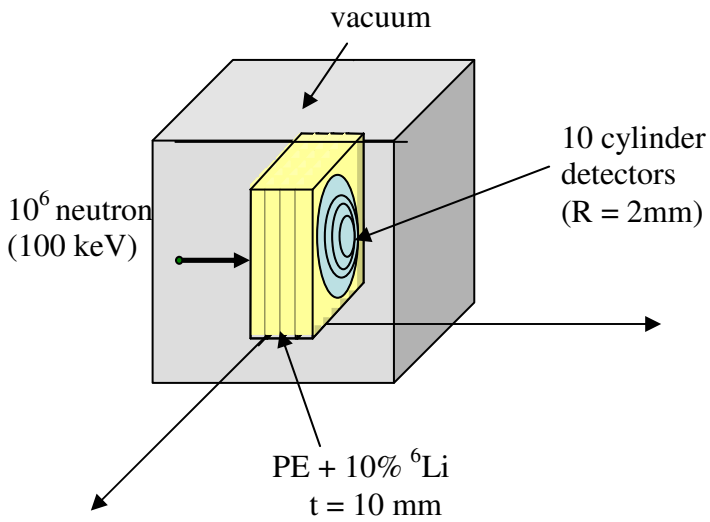

***Fig 4.7**. Schematic view of the geometry to compare GEANT4 and MCNP response.*

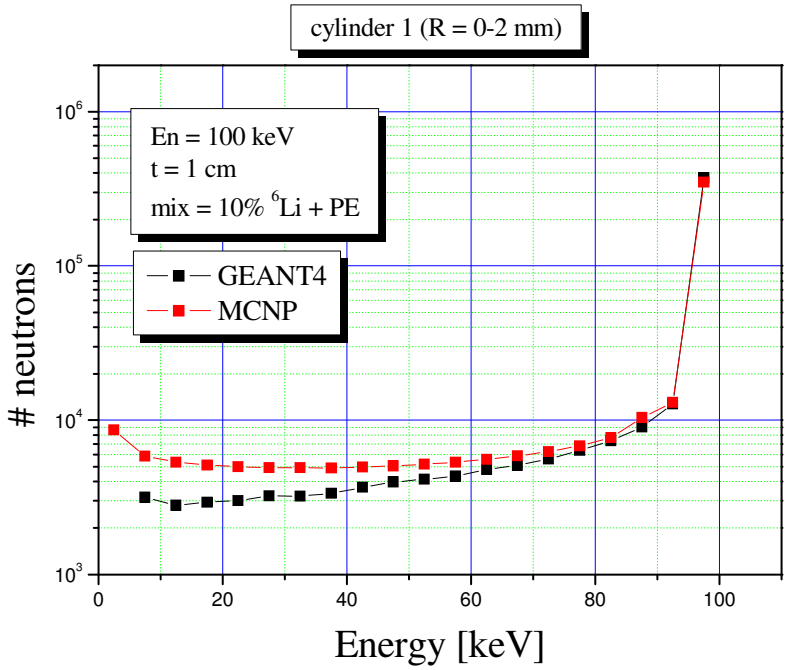

***Fig 4.8**. Comparison of MNCP and GEANT4 neutron spectrum in the central cylinder at the exit of the moderator/absorber layer (10 mm, 10% Li). Incident neutron energy of 100 keV.*

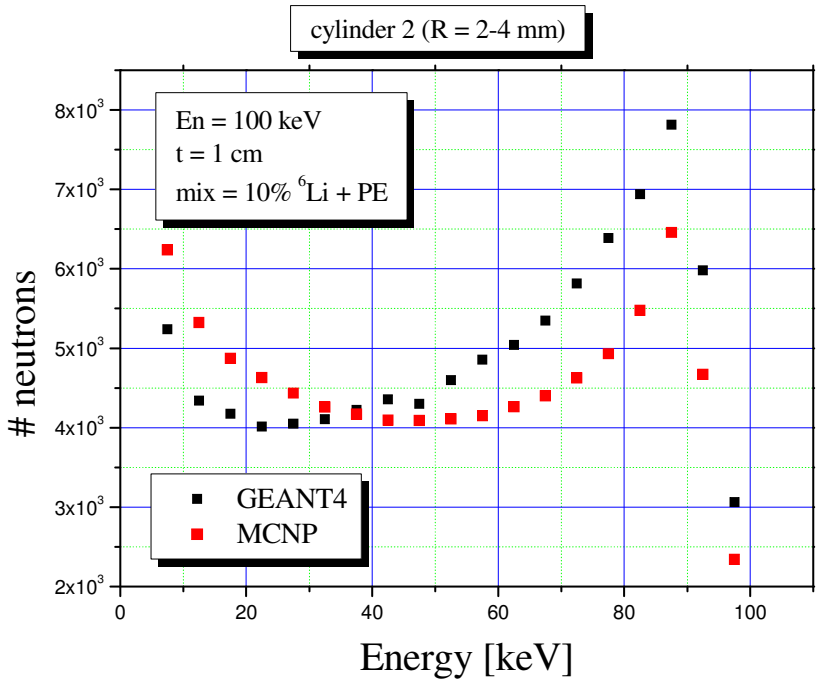

***Fig 4.9**. Comparison of MNCP and GEANT4 neutron spectrum in the second cylinder (R_{in} = 2 mm, R_{out} = 4 mm) at the exit of the moderator/absorber layer (10 mm, 10% Li). Incident neutron energy of 100 keV.*

After the comparison of MNCP vs GEANT4 for the neutrons response function, we decided to use MNCP for the neutrons inside the moderator/absorber layer and GEANT4 (or MCNPX in the future) for what concern the transport of charge particles.

4.7 Simulation with MCNP (versions 4.c and 5)

In order to get an idea of position sensitivity we generated a Point Spread Function (PSF) for different energy, thickness and composition and we calculated the FWHM (full weight at half maximum) and FWTM (full weight at tenth maximum). The first step of simulation was the evaluation of the PSF behind a 1 cm moderator/absorber thickness, with different composition of the absorber/moderator (%PE + %^{6}Li) and different energy of the incident neutron beam (from 100 keV up to 10 MeV);

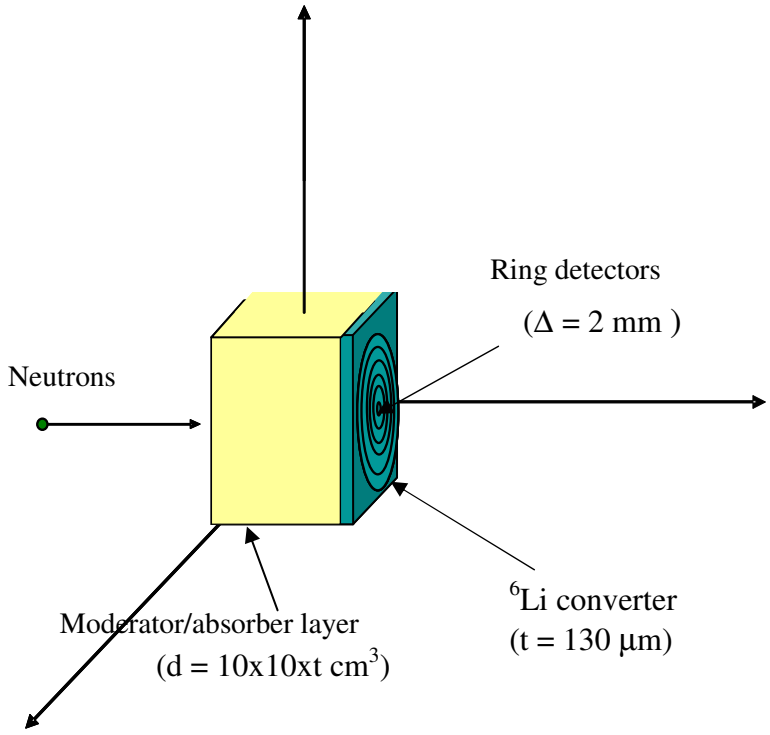

***Fig 4.10**. Set up for the simulations*

We set up a ring structured detector of a 130 μm thick ^{6}Li (as shown in Fig. 4.10) and we simulated the probability of a ^{6}Li(n,t)α reaction (number of tritons created in each detector ring for cm^2 and normalized for the number of incident neutron (10^7)).

In Fig. 4.11 are shown the PSF for different moderator/absorber composition at the same energy of neutron incident beam. For the thickness of 1 cm, the composition of the layer doesn't make changing in the PSF. To show the trend of the PSF outside the central ring, we plot it in Fig. 4.12 in logarithmic scale.

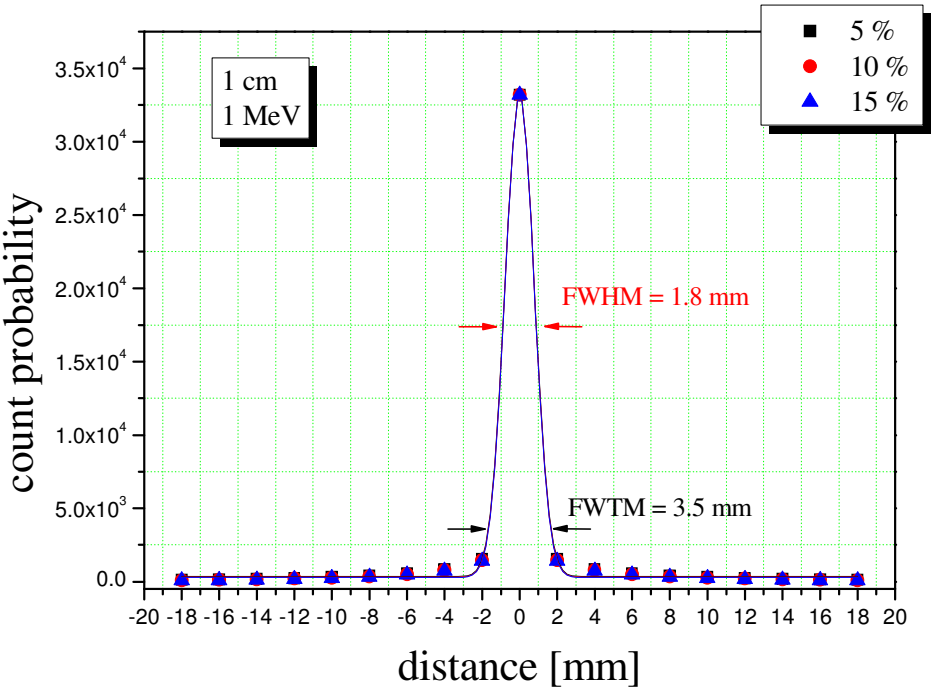

***Fig 4.11**. Comparison of PSF for different moderator/absorber composition (% ^{6}Li) with 1 cm thickness and for 1 MeV needle incident neutron beam*

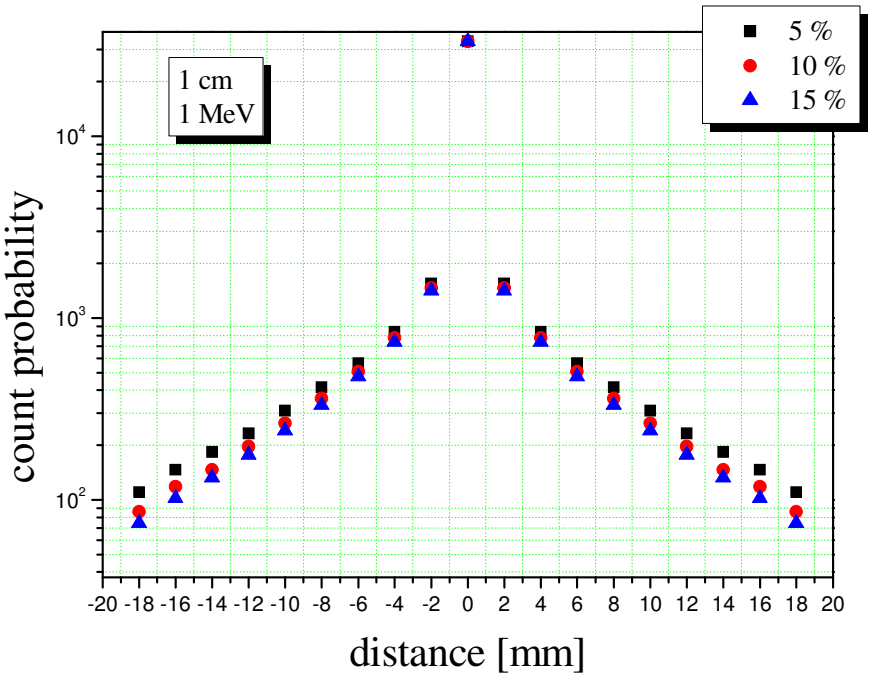

***Fig 4.12.** Comparison of PSF for different moderator/absorber composition (% ^{6}Li) with 1 cm thickness and for 1 MeV needle incident neutron beam in logarithmic scale*

To understand the role of the ^{6}Li in the moderator, we made the same calculation behind a thickness of 20 cm. In Fig. 4.13 are shown the results for the energy of 5 MeV neutron incident beam. The spatial information is completely lost for 100 keV and 1 MeV. Fig. 4.14 shows the PSF for 20 cm, at 5 MeV, in logarithmic scale.

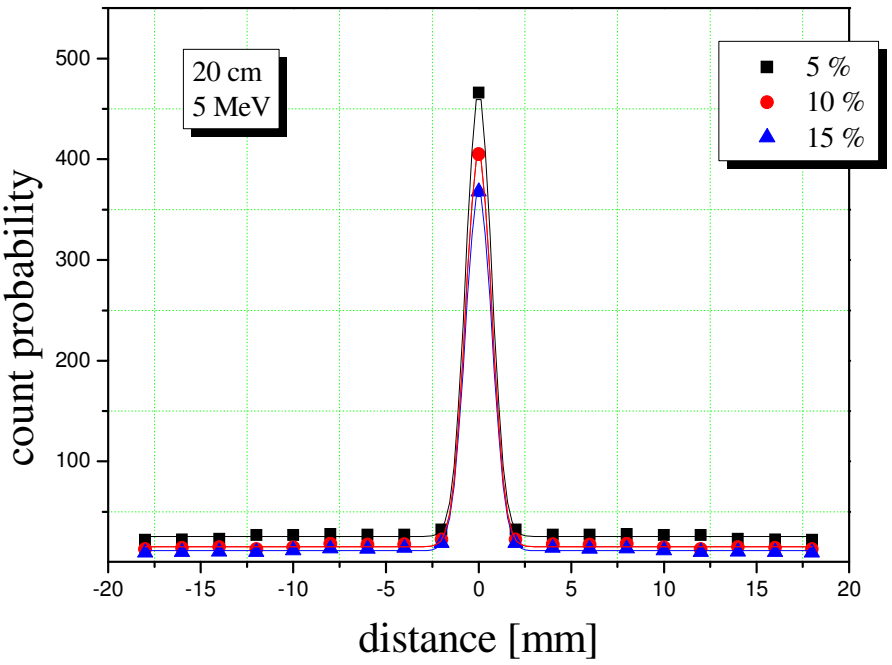

***Fig 4.13**. Comparison of PSF for different moderator/absorber composition (% ^{6}Li) with 20 cm thickness and for 5 MeV needle incident neutron beam. FWHM : 1.63 mm (5%); 1.66 mm (10%); 1.69 mm (15%); FWTM = 3.5 mm (5%); 3.5 mm (10%); 3.5 mm (15%)*

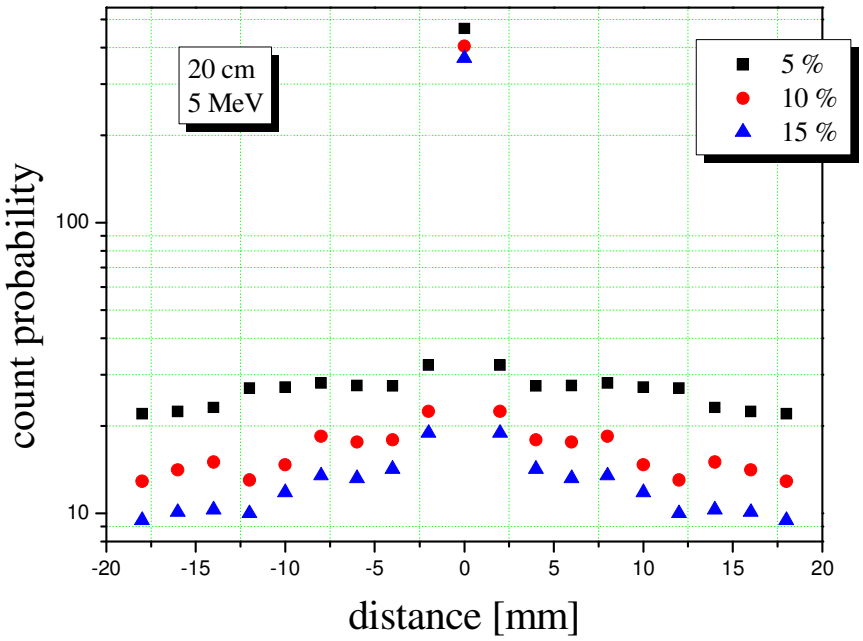

***Fig 4.14**. Comparison of PSF for different moderator/absorber composition (% ^{6}Li) with 20 cm thickness and for 5 MeV needle incident neutron beam with logarithmic scale.*

We calculated the FWHM and the FWTM for each energy, thickness and composition. In Fig. 4.15 and 4.16 the FWHM and FWTM versus the energy of incident neutron beam are respectively shown, whereas in Fig. 4.17 and 4.18 as function of the moderator/absorber thickness.

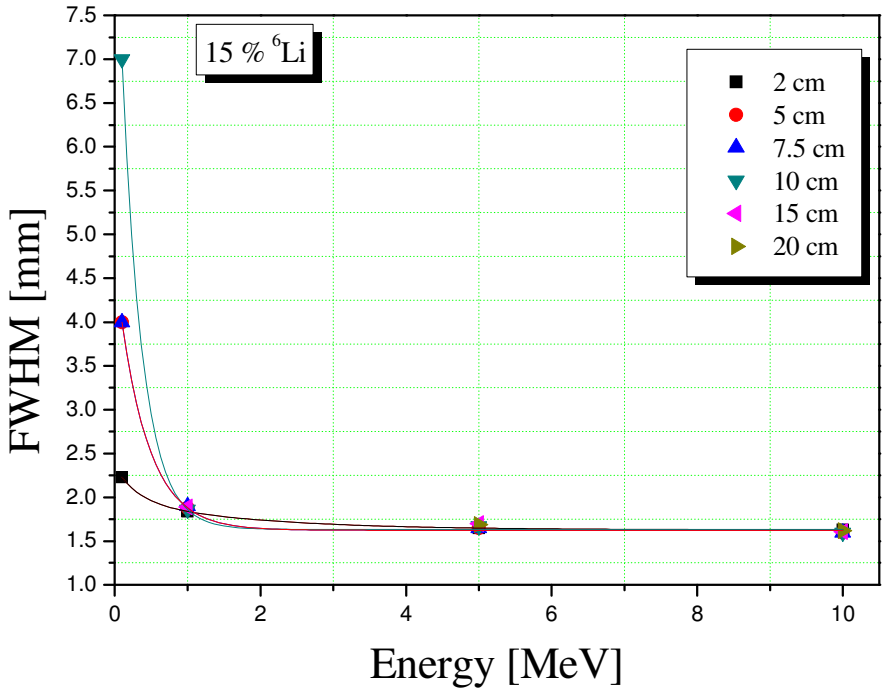

***Fig 4.15**. Comparison of FWHM versus energy of incident neutron for different thicknesses*

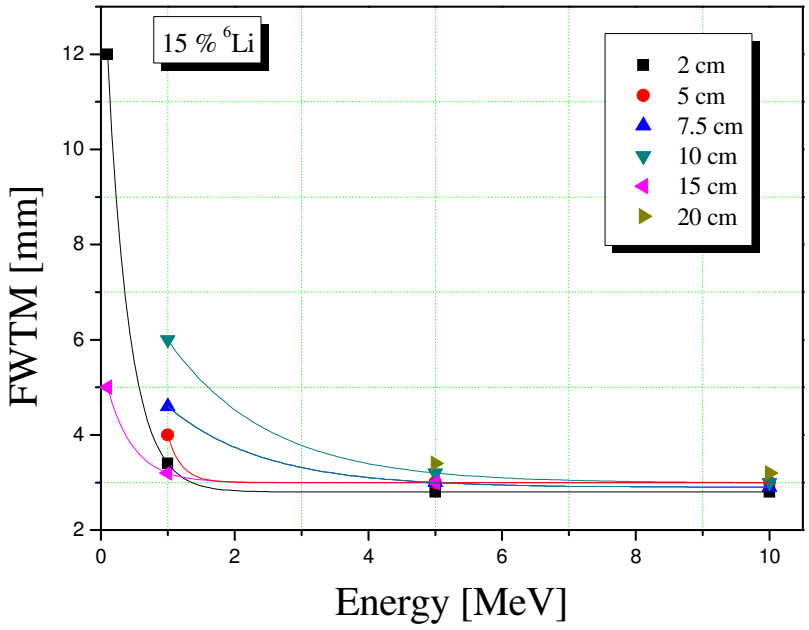

***Fig 4.16**. Comparison of FWTM versus energy of incident neutron for different thicknesses*

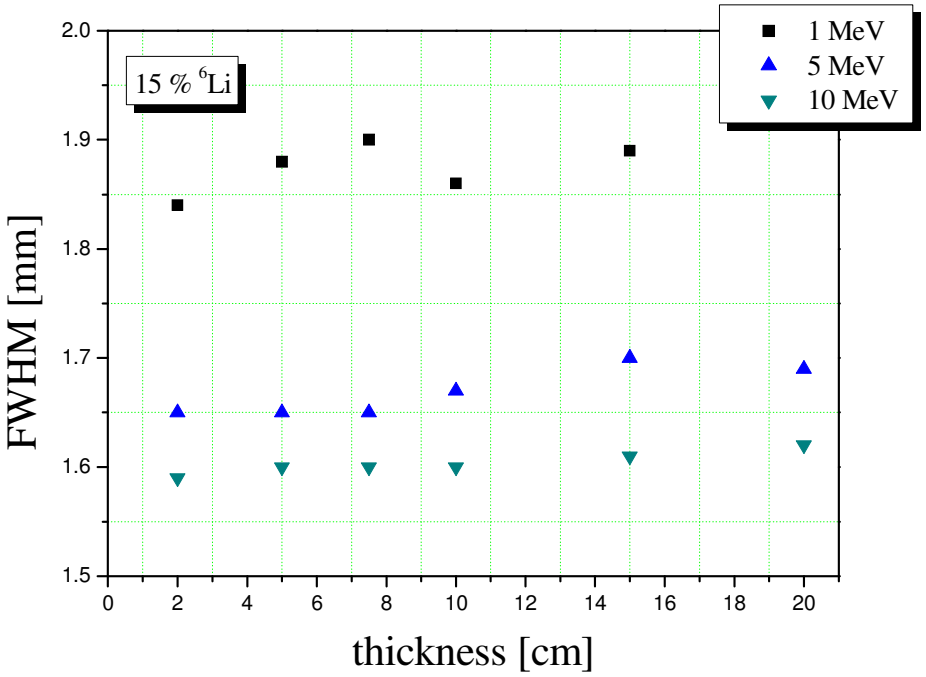

***Fig 4.17**. Comparison of FWHM versus the thickness of the moderator/absorber*

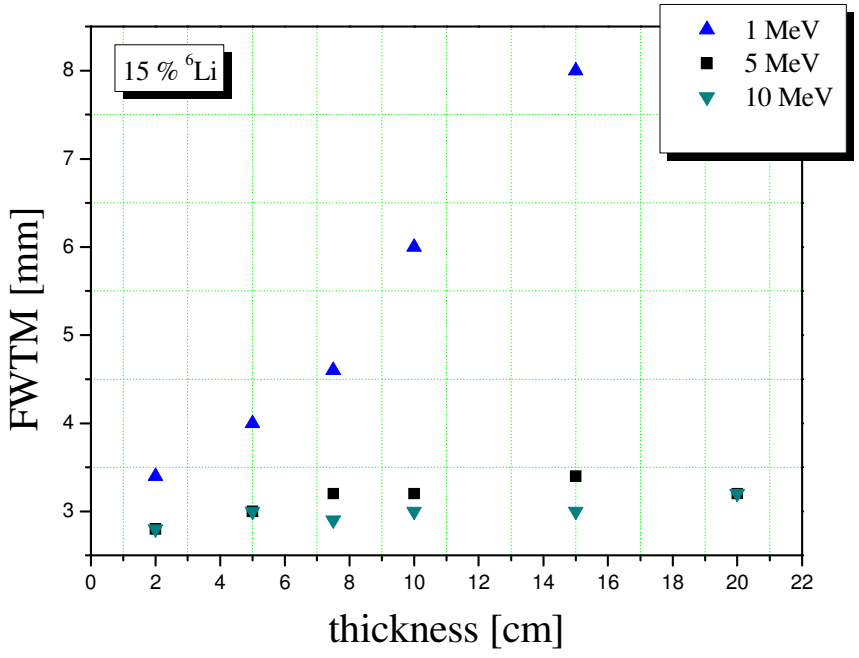

***Fig 4.18**. Comparison of FWTM versus the thickness of the moderator/absorber*

Even if the resolution seems to be very good, we refined the PSF between 0-2.5 mm, with 9 detector cylinder. In Tab 4.5 the FWHM and FWTM for 5 cm thickness are shown.

Energy (MeV)	t (cm)	FWHM (mm)	FWTM (mm)
0.1	5	0.26	6
1	5	0.22	0.44
5	5	0.2	0.38
10	5	0.18	0.34

***Tab 4.5**. Comparison of FWHM and FWTH versus energy of incident neutron for 5 cm thickness*

As shown in Fig. 4.19 for the 5 cm thickness, the PSF is still dominated by the singularity at 0 radial distance. This is due to the interaction of the primary neutrons (neutrons which didn't have a single interaction in the moderator/absorber) in the converter foil. Those neutrons don't participate in the "Bonner mechanism" which implies moderation and capture when thermalised.

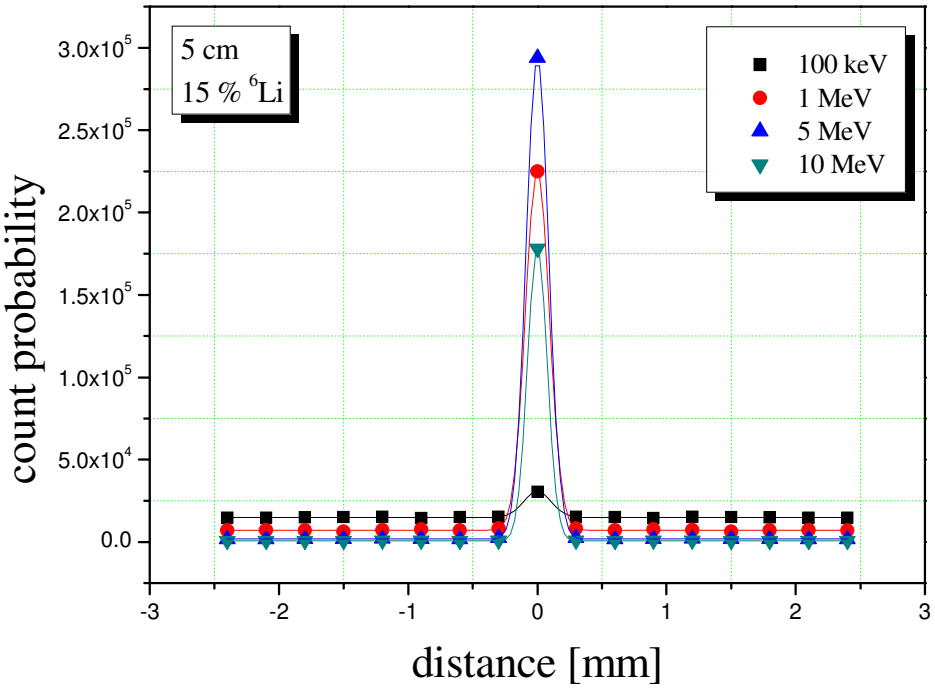

***Fig 4.19**. Comparison of PSF for 5 cm thickness of the moderator/absorber at different incident energy (composition 15% ^{6}Li).*

In order to obtain the PSF for only moderated neutrons, we set up a ring structured "detector" of a 130 µm thick ^{6}Li (10 cylinder, Δ = 0.5 cm) and we simulated the probability of a ^{6}Li(n,t)α reaction (number of tritons created in each detector ring for cm^{2} and normalized for the number of incident neutron (10^{8})). We used mono-energetic neutron beams (0.1, 0.5, 5, 10 MeV) and different thicknesses of moderator/absorber layer (2, 5, 10, 15, 20 cm). In each ring we obtained the number of ^{6}Li(n,t)α reactions per every energy bin. In Fig. 4.20 and 4.21 the results in the central disc and in the first ring (R = 0.75 cm), for 5 cm absorber/moderator thickness are respectively shown; these plot can be seen as the neutron spectrum convolved with the ^{6}Li(n,t)α cross section. For each position, energy and thickness, we evaluated the number of counts from 0 to 80 keV and we calculated the FWHM. The results are shown in Tab. 4.6 .

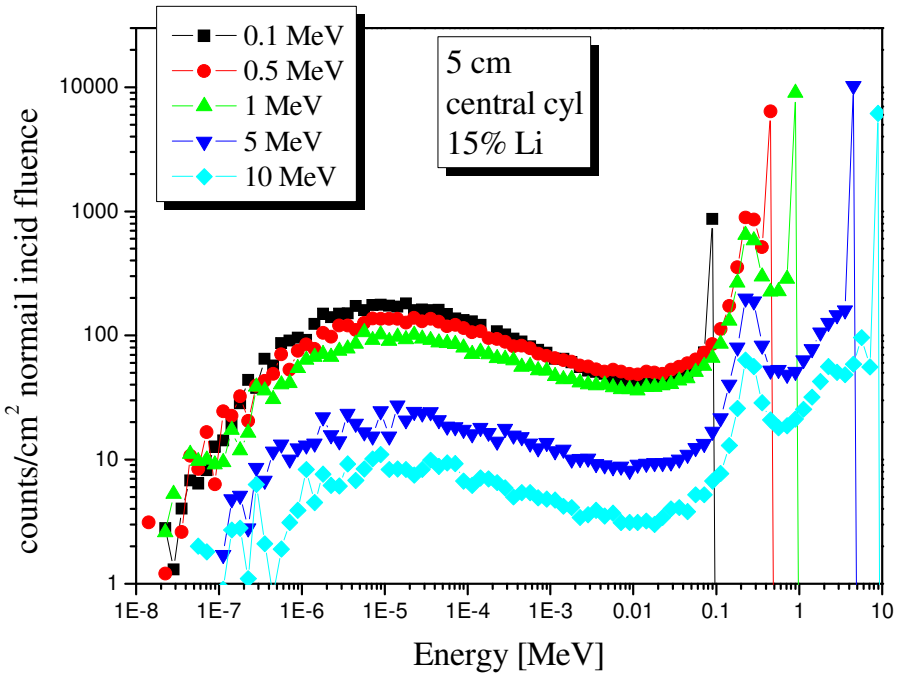

***Fig 4.20**. Number of ^{6}Li(n,t)α reactions in the central disc (R = 0.25 mm) of ^{6}Li converter foil, for 5 cm thickness layer and for different incident beam (100 keV, 0.5 MeV, 1 MeV, 5 MeV, 10 MeV)*

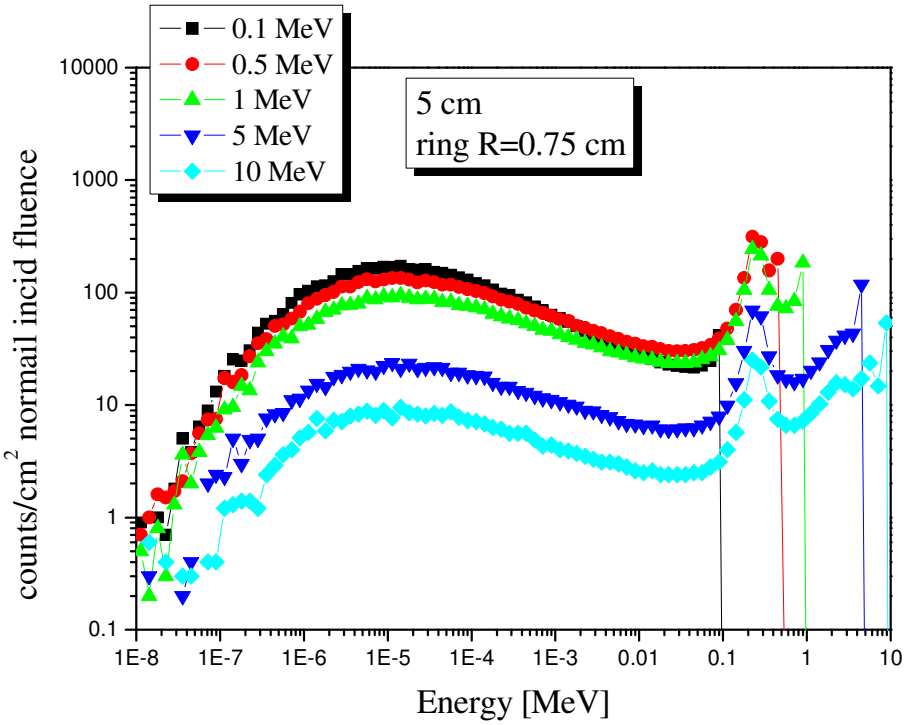

***Fig 4.21**. Number of ^{6}Li(n,t)α reactions in the first ring (R = 0.75 mm) of ^{6}Li converter foil, for 5 cm thickness layer and for different incident beam (100 keV, 0.5 MeV, 1 MeV, 5 MeV, 10 MeV)*

Thickness (cm)	**2**	**5**	**10**	**15**	**20**
Energy (MeV)	**FWHM (cm)**				
0.1	1.7	3.6	6	7	
0.5	2	3.7	6	7	7
1	2.3	3.8	6	7	8.4
5	2.8	4	7.1	7.6	8.6
10	3	4.1	8	9	9.4

***Tab.4.6**. Comparison of FWHM versus energy of incident neutron for different thicknesses (15% Li)*

The FWHM for thickness higher then 5 cm were simulated with detector size of 30 x 30 cm. This is to avoid the artefacts due to the finite size of the detector (10 x 10 cm). Some example of PSF are shown in Figs 4.22 , fitted with a Lorentzian function.

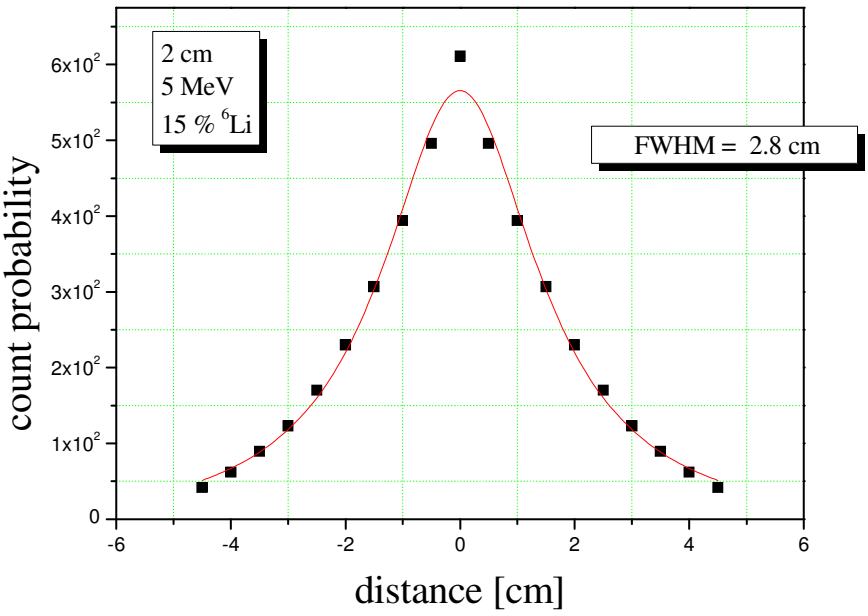

Fig 4.22.a *PSF for 2 cm thickness and for 5 MeV needle incident neutron beam (15% ^{6}Li). Only neutrons with energy < 80 keV are considered.*

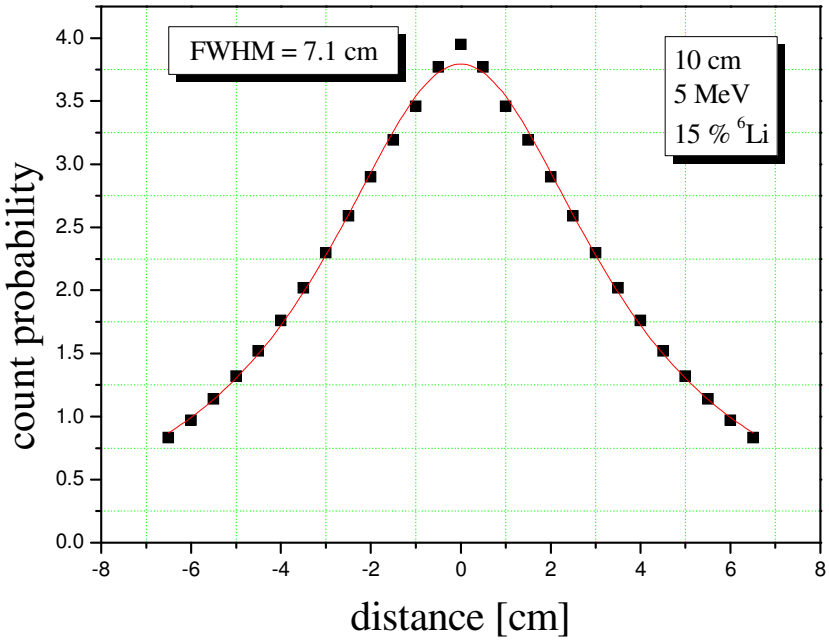

Fig 4.22.b. *PSF for 10 cm thickness and for 5 MeV needle incident neutron beam (15% ^{6}Li). Only neutrons with energy < 80 keV are considered.*

In order to understand the role of Li inside the moderator/absorber, we employed a simulation without dopant in the layer (PE density 0.93 g/cm^3). The FWHM for different energy at 10 cm are shown in Tab. 4.7.

thickness (cm)	10	10 no Li
Energy (MeV)	FWHM (cm)	
0.1	6	8
0.5	6	8
1.0	6	8.6
5.0	7.1	10
10.0	8	10.7

Tab 4.7*. Comparison of FWHM versus energy of incident neutron for 10 cm thicknesses with 15% and 0% of ^{6}Li.*

Response functions

As second step, we calculated the response functions for different thicknesses of moderator/absorber (2, 5, 7, 10, 15, 20) in detectors located in three different positions, for mono-energetic neutrons (0.1, 0.2, 0.5, 1, 2, 5, 7, 10 MeV).

We employed a simulation tool to detect the number of ^{6}Li(n,t)α reactions. A layer of polyethylene (PE) mixed with 15% of ^{6}Li is placed between mono-directional neutron beam emitted from a 10 x 10 cm^2 source, and three ring detectors of a 130 μm thick ^{6}Li (Fig. 4.23). These ones are close to the moderator/absorber layer and we simulated the probability of a ^{6}Li(n,t)α reactions (number of tritons created in each detector ring for cm^2 and normalized for the number of incident neutron (10^8)).

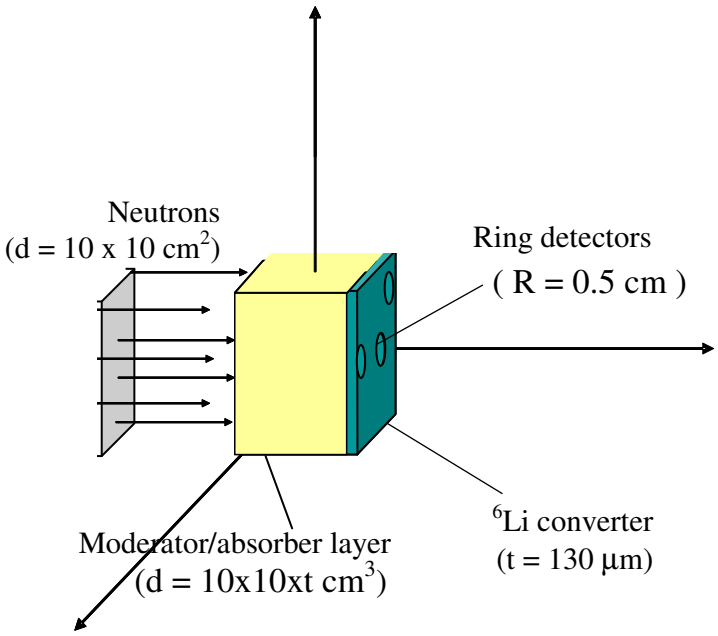

***Fig 4.23**. Schematic view of the simulation set-up.*

The comparisons of those energy response functions, for the central ring detector and for a mixture layer of 15% ^{6}Li, are shown in fig. 4.24.

The response functions for the Bonner sphere is defined as the efficiency of the detector as a function of incident neutron energy. The shape of these depend on the size and material of the moderator. As the size of the moderator is increased, the peak of the response function shifts to a higher neutron energy. This seems to happen in our calculations (Fig. 4.25), but the attenuation of the thermal flux is to high to provide a sharp response for high energy, as shown in Fig. 4.26 for the Bonner sphere spectrometer at PTB. The advantage of the BS geometry is the backscatter of the surrounding material. This phenomena is absent in our flat configuration.

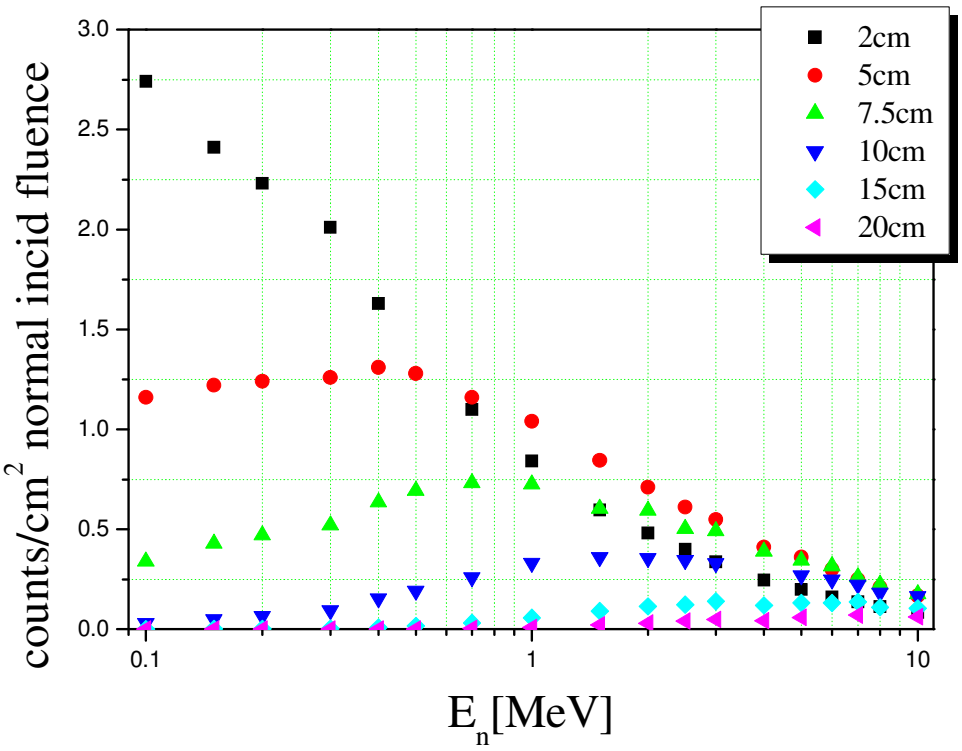

***Fig 4.24**. Comparison of the energy response function, in the central ring (R=0.5 cm), for different thicknesses of the moderator/absorber (15% ^{6}Li). Incident mono-energetic neutron beam of 0.1 MeV,0.15 MeV, 0.2 MeV, 0.3 MeV, 0.4 MeV, 0.5 MeV, 0.6 MeV, 0.7 MeV, 1 MeV, 2 MeV, 3 MeV, 4 MeV, 5 MeV, 7 MeV, 10 MeV*

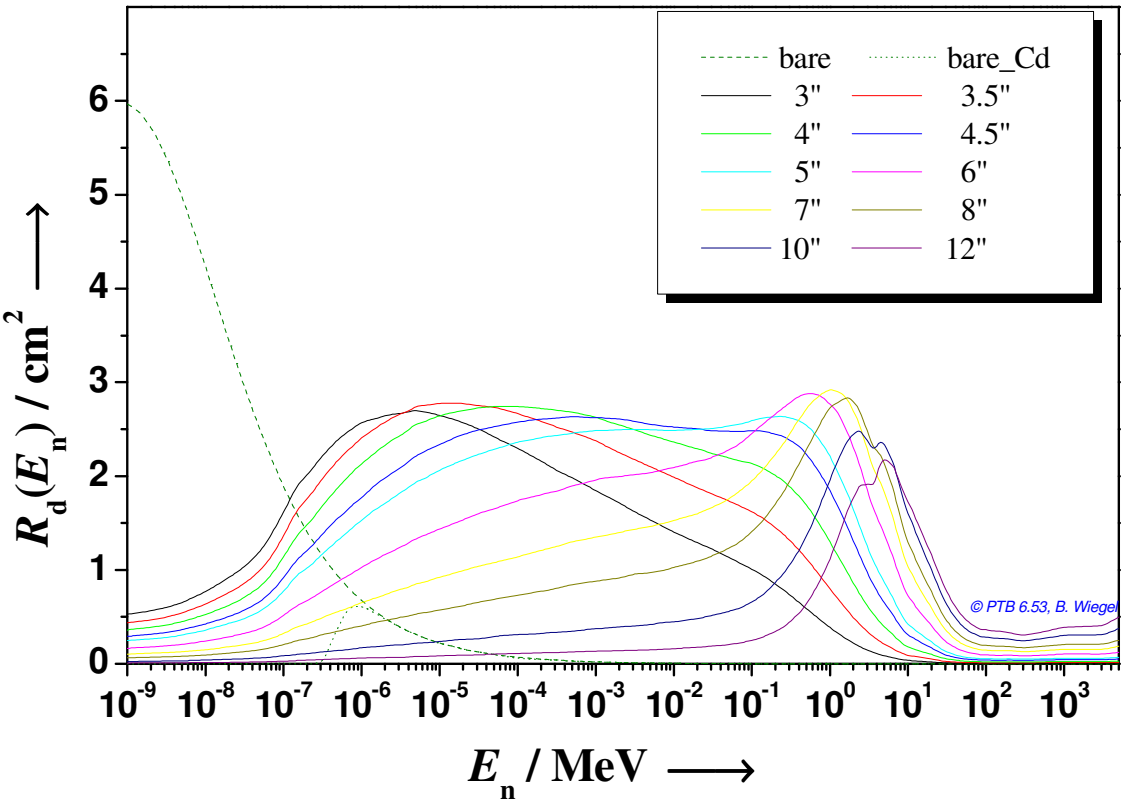

***Fig 4.25**. Responses of the PTB Bonner sphere spectrometer*

In order to check the detector response (i.e. the number of capture reaction in the converter) we performed "theoretical experiment" a using a realistic BNCT spectrum. We chose to use the spectrum from the BNCT facility at the Nuclear Research Reactor of Řež (CZ) [44]; as shown in Fig. 4.26, this is a spectrum with a high epithermal neutron component and a not negligible fast one.

The geometry of the simulation set-up is similar to the one in fig. 6, but instead of a 10 x 10 neutron source, we used a disk source with 12 cm diameter (parallel beam). The size of the detector is 30 x 30 cm and we detected the number of ^{6}Li(n,t)α reactions in the central cylinder detector (R=0.5 cm).

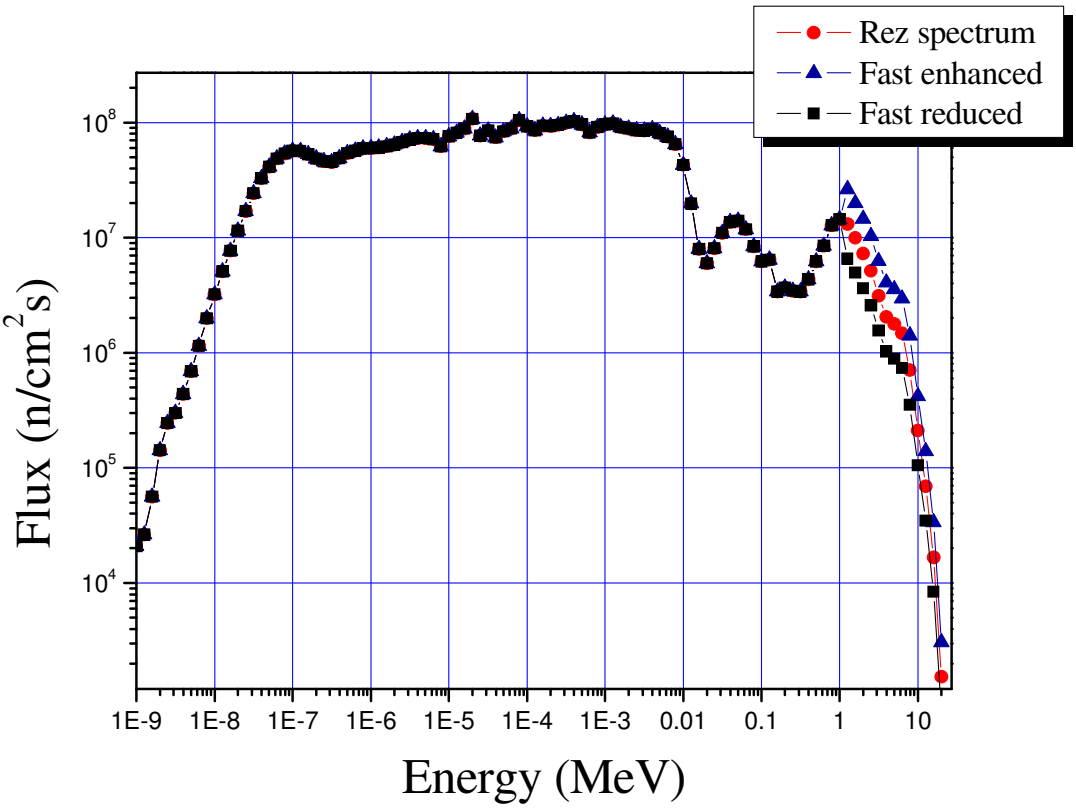

***Fig 4.26**. The spectral distribution of the Řež Reactor BNCT facility is shown (red points), together with the "Fast enhanced" spectrum (blue triangles and the "Fast reduced" spectrum (black square).*

In order to evaluate the different detector responses for different incident energy distributions, similar simulations were performed with two varied spectra: at first the number of source neutrons with energy > 1 MeV was doubled ("Fast enhanced" spectrum), then the same spectrum component was halved ("Fast reduced" spectrum) (see Fig. 4.27).

In Fig. 4.28 the three different responses are shown. The ordinate is the number of counts/cm^{2}s and the abscise is the moderator/absorber thickness; for thicknesses above 10 cm, the higher is the fast neutron component the bigger is the number of counts.

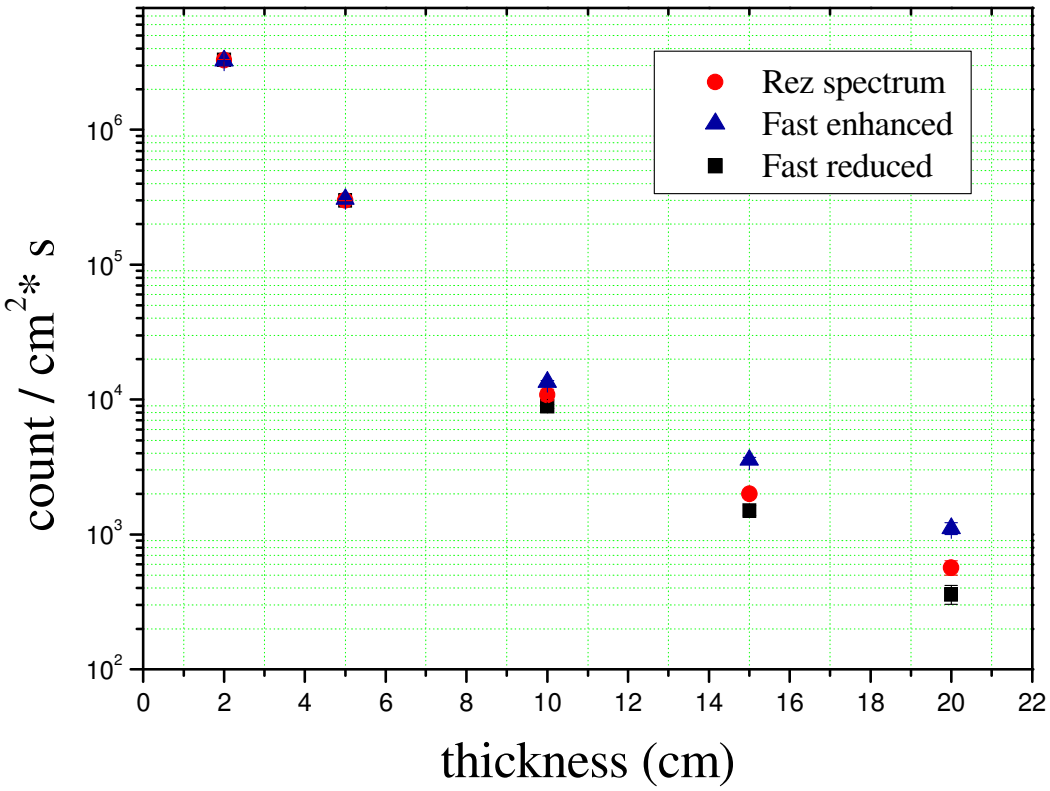

***Fig 4.27**. Comparison of the response for the Řež Reactor BNCT facility, the "Fast enhanced" and the "Fast reduced" spectrum at different moderator/absorber thickness.*

Spectral calculations

In order to calculate the energy distribution of neutrons passing through the absorber/moderator we performed some Monte Carlo calculation.

The source was a 12 cm diameter disk with Řež spectrum (Fig. 4.27), positioned in front of the 15% ^{6}Li absorber/moderator (area is 30 x 30 cm^2). Close to the opposite absorber/moderator side, a vacuum cylinder (t:130µm, d:8cm) was positioned with the axis centred in the 30 x 30 cm^2 area; in this cylinder the neutron fluxes (1/cm^{2}s) are calculated (Fig 4.29).

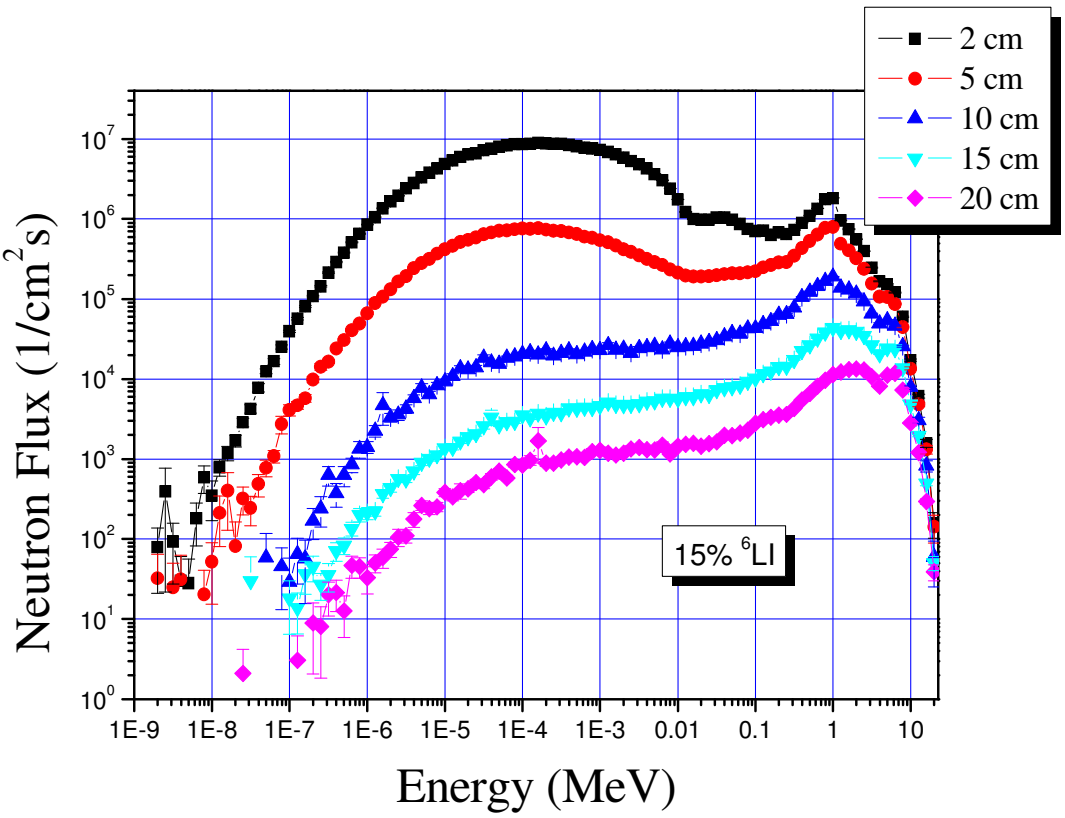

***Fig 4.28**. Energy distribution of the neutrons getting out from the 15% ^{6}Li absorber/moderator. The neutron fluxes for different thicknesses are shown.*

Summary and conclusion

The feasibility of the application of THGEM-detectors for measurement in neutron fields possibly with spectroscopic information, was investigated. After an initial study of the properties of THGEM-based detectors a preliminary configuration of a spectrometric imaging system for fast (0.1 – 10 MeV) neutrons was proposed and Monte Carlo simulations, using GEANT4 and MCNP4c-5 codes, were performed to assess its properties.

The operation of THGEM-based detectors in pure Ar and Ar/CH_4 at room temperature was studied in atmospheric pressure. Gains of 10^4 were obtained with 5.9 keV x-rays in both gases in the tested configurations with rim = 0.1 mm at atmospheric pressure. Energy resolutions of 30% were measured in Ar. A new economical method of THGEM production was studied and some results for different $3x3cm^2$ THGEM configurations (rim = 0.04 mm, 0.06 mm, 0.08 mm and 0.12 mm) were described.

One of the potential applications of such THGEMs is fast and thermal neutron detection and imaging, using a solid radiation converter where neutrons interact and produce energetic charged particles which can be directly detected by the gas detector. Two kind of detectors based on THGEM were proposed and investigated in this work: a fast neutron imaging detector based on the detection of recoil protons from a polyethylene (PE) and a Bonner-type flat neutron imaging spectrometer. Such detectors will provide new and useful information for BNCT (Boron Neutron Capture Therapy) research, such as simultaneous spatial and spectral characterisation of the fast neutron neutron component of the radiation field with a spatial resolution of centimetres inside a phantom and in free air. The efficiency of the detection configuration using PE converter is rather low and is not suitable for the measurement of neutrons below 5 MeV. The second approach, using the detection of moderated neutrons should permit determination of neutron spectra within a energy range of 0.1-10 MeV. The principle of the latter method is very similar to a Bonner sphere spectrometer (BS), but instead of the usual spherical geometry we use a set of flat moderator plates with different thicknesses. To improve the spatial resolution of the spectrometer the moderator is “poisoned” with an absorber material for thermal and epithermal neutrons to restrict the diffusion length of those neutrons. A full spectrometer requires a series of measurements with different thicknesses of those moderator/absorber layers. Suitable moderator/absorber layers might be mixtures of

polyethylene (moderator) and ^{6}Li or ^{10}B (absorber). The moderator/absorber layer is positioned in front of a slow- neutron detector made of a neutron converter foil (e.g. ^{6}Li, ^{235}U) coupled to two cascaded THGEM and a dedicated read-out electrode. Some preliminary studies and simulations were done with Monte Carlo calculation codes (GEANT4 and MCNP4c-5). Compared to the BS, the response function of our configuration shows a lower efficiency, but the new proposed flat-geometry should allow to reduce set-up drawbacks and moreover to obtain spatial information.

The results pave the way towards more extensive studies.

Appendix A - Boron Neutron Capture Therapy (BNCT)

Boron Neutron Capture Therapy (BNCT) is a form of radiation therapy [10,11], currently in the research stage, having a very peculiar characteristic. It can be considered as a particular kind of conformal radiotherapy which the target is not the tumour volume, but each tumour cell. BNCT takes advantage of the high cross section, for slow neutrons, of the reaction of the stable isotope ^{10}B, previously selectively accumulated in the tumour tissue:

$$^{10}B(n,\alpha)^{7}Li \quad (\sigma = 3840 \text{ barn})$$

The isotope ^{10}B absorbs a low energy neutron and ejects energetic short-range alpha particles and lithium ions which deposit most of their energy within the cell containing the original ^{10}B atom (Fig A.1).

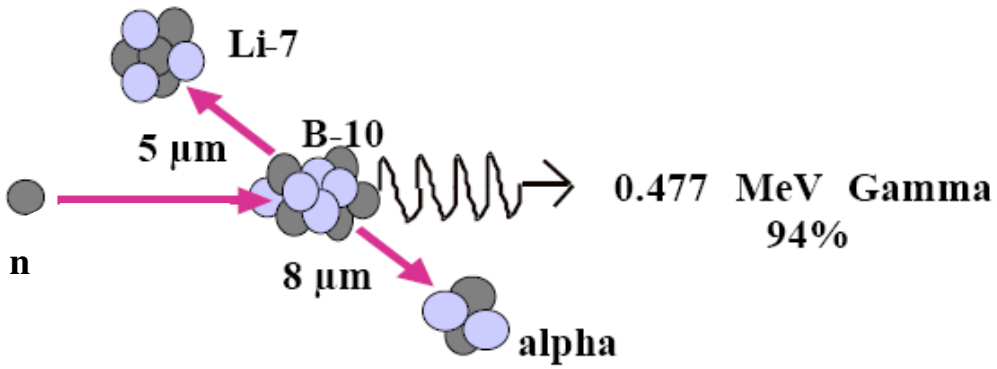

***Fig A.1**. Schematic view of ^{10}B reaction*

If ^{10}B concentration in tumour cells is higher then in normal tissues, a higher dose will be delivered to tumour cells during neutrons irradiation [45]. There are a lot of nuclides that have a high propensity for absorbing low energy or thermal neutrons. Of the various nuclides that have high neutron capture cross-sections, ^{10}B (σ = 3840 barn) is the most attractive because the product is not radioactive, the particles emitted by the capture reaction $^{10}B(n,\alpha)^{7}Li$ have high LET (dE/dx) and their combined path lengths are approximately one cell diameter (about 12

μm) then limiting the radiation effect to the tumour cells that have taken up a sufficient amount of ^{10}B, and simultaneously sparing normal cells. For BNCT to be successful, a large enough number of ^{10}B atoms must be accumulated in the tumour tissue (~35 μg per g) and the thermal neutron fluence on the tumour tissue must be enough to obtain the killing effect. The radiation effect or produced damage can be extremely localized, thereby sparing normal tissue cells. Thus, selectivity is one of the advantages and simultaneously troubles of neutron capture therapy, since it requires delivery of ^{10}B to tumour cells in suitably greater amounts than normal cells. If the ^{10}B is not suitably localized, undesirable effects may be produced in normal tissue cells [46].

The concept of neutron capture therapy (NCT) was introduced in 1936 [47], four years after the discovery of neutrons. In 1951 it was first demonstrated that certain boron compounds would allow higher boron concentration in human brain tumor cells in comparison with normal brain tissue. After a period of experimentation in USA and then in Japan, not much successful owing to selectivity of ^{10}B compound and improper neutron energy, more focused researches has been started in all of the world. In 1997, clinical trials began in Petten (Netherlands) as a result of joint effort of the European Community. In June 1999 clinical trials began in Finland. Today England, Australia, Argentina, Italy, Germany, Sweden, Slovakia, Czech Republic, Russia have been developed wide BNCT activity and trials. At that time, not only in Europe but also worldwide, the interest had generated the growth research activities at a large number of institutes with the objective to develop neutron beams for medical applications.

The dosimetry in neutron fields suitable for BCNT is particularly complex owing to the multiplicity of the mechanism of neutron interactions and the involved materials.

Currently epithermal neutron beams, with sufficient intensity for patient treatment with BNCT, can only be produced in nuclear reactors. Reactor-derived neutrons are classified according to their energies as thermal (En < 0.5 eV), epithermal (0.5 eV < En < 10 keV) or fast (En >10 keV) [48]. Thermal neutrons are the most important for BNCT because they have the maximum cross section for the $^{10}B(n,\alpha)^{7}Li$ reaction; however, since they have a limited depth of penetration, epithermal neutrons, which lose energy and fall into the thermal range as they penetrate tissues, are necessary for treatment of deep tumors. In epithermal beams from reactor sources a fast-neutron component is unavoidably present.

It is necessary to specify something about the concept of *absorbed dose*. It is equal to the energy absorbed per unit mass of the medium, measured in J/kg, called *Gray* (Gy). The total absorbed

dose (D_t) in tissue irradiated with BNCT beams originates from thermal neutrons, intermediate and fast neutrons and gamma rays. Thermal neutrons, present in low amount in the incident beam, but are produced by the thermalization of epithermal neutrons in tissue. Four dose components contribute when the beam enters tissue are:

(1) *the gamma ray dose, D_γ:* the total dose due to the gamma ray background and to the gamma rays induced in the tissue itself by the neutron interactions. The induced gamma rays are mainly due to thermal neutron reactions with hydrogen in tissue $^1H(n,\gamma)^2H$. The emitted gamma rays have energy of 2.2 MeV;

(2) *the fast neutron dose, D_n*: epithermal and fast neutrons mainly cause "knock-on" recoil protons from hydrogen in tissue. Such reaction $^1H(n,n')p$ results in locally deposited energy from the recoil proton. Locally deposited energy from any other fast-neutron induced reactions, if they happen, have to be included; e.g., $^{12}C(n, \alpha)$ reaction for fast neutrons above about 8 MeV;

(3) *the nitrogen dose, D_N:* ^{14}N in tissue absorbs a thermal neutron and emits a proton in a $^{14}N(n,p)^{14}C$ reaction. The emitted proton has an energy of about 640 keV and then a very short range in tissue. So the dose of the proton and the recoil ^{14}C nucleus results in a locally deposited energy.

(4) *the boron dose, D_B:* ^{10}B absorbs a thermal neutron in a $^{10}B(n,\alpha)^7Li$ reaction. The energetic emitted alpha particle and the recoiling ^7Li ion result in locally deposited average energy of about 2.33 MeV. In 94% of the reactions the recoil ^7Li ion is produced in an excited state and de-excites in flight, emitting a 477 keV gamma ray. In the remaining 6% of events, the ^7Li is emitted in the ground state with no gamma ray emission. As the emitted gamma rays are less prevalent and of considerably lower energy than the 2.2 MeV gamma rays from hydrogen capture, they give negligible but are frequently utilized for the purpose of ^{10}B analysis [48].
So, the expression of the total absorbed dose is:

$$D_{tot} = D_\gamma + D_n + D_N + D_B$$

The various dose components have a different *Relative Biological Effectiveness* (*RBE*) and therefore have to be determined separately. The *RBE* has been expressed numerically as factor which multiplied by the dose in study give a reference dose that produce the same biological effect under the same conditions. ($D_x * RBE = D_{ref}$).

In our case, the reference dose is the sum of the different contribution previously described. In a simple formulation, one can write the reference dose, as

$$D_{ref} = (C_B \cdot CBE_B \cdot D_B) + RBE_N \cdot D_N + RBE_n \cdot D_n + RBE_\gamma \cdot D_\gamma$$

where C_B is the ^{10}B concentration and CBE is a factor for the reaction products of ^{10}B, which is like an RBE but corrected for the characteristics of the compound transporting the ^{10}B atoms into the tumour or healthy cells.

For the safe treatment of patients with ionizing radiation, it is of crucial importance that the basic characteristics of the neutron beam (beam geometry, neutron and spectrum, absorbed dose and fluence distributions), are determined with in-air and in phantom, in a coherent and reproducible way. Therefore, reliable dose-monitoring systems are needed in order to verify that the characteristics of the beam satisfy all the required restrictions.. Consequently, for the BNCT treatment planning is important the determination of spatial dose component distributions, in agreement with the desired neutron beam parameters defined by the International Atomic Energy Agency (IAEA) [5].

For the measurement of each *relevant dosimetric quantity*, the method should satisfy the following requirements:

- The calibration of the radiation detector used in the method must be consistent with the international measurement system (IAEA, 2000);
- the method must provide the value of the *relevant dosimetric quantity* with acceptable uncertainty;
- the target values for the maximum acceptable uncertainty are:
    - 5 % for the thermal neutron fluence;
    - 5 % for the gamma ray absorbed dose to reference tissue;
    - 10 % for the fast neutron absorbed dose to reference tissue;
- the method must be practical and feasible to use.

A schematic view of the methods considered for the determination of fast neutron and gamma ray absorbed dose and thermal neutron fluence are shown in Table A.1.

Method	Quantity to be measured			Reviewed references
	Thermal neutron fluence	Gamma ray absorbed dose to reference tissue	Fast neutron absorbed dose to reference tissue	
Paired ionisation chamber technique (Mg(Ar) & TE(TE) chambers)		X	X (total neutron absorbed dose)	Rogus et al.,1994; Raaijmakers et al., 1995; Kosunen et al., 1999; Munck af Rosenschöld et al., 2002, 2003
Thermo-Luminescence Dosimeters (TLD)	X	X	X	Virágh, 1984; Toivonen et al., 1998; Aschan et al., 1999; Gambarini et al., 2001; Kessler et al., 2001; Seppälä et al 2002a
TE(TE) Proportional Counter Microdosimetry		X	X (total neutron absorbed dose)	Green et al., 1997; Kota et al., 2000; Burmeister et al., 2001; Wuu et al., 1992
Activation analysis (manganese, copper and gold foils)	X			Rogus et al., 1994; Raaijmakers et al., 1995 ; Serén et al., 1999
Gel dosimetry (Fricke-gels)		X	X	Gambarini et al., 2002
Gel dosimetry (polyacrylamide gels)		X	X	Farajollahi et al., 2000; Uusi-Simola et al., 2003; Spevacek et al., 2002
Si(Li)-Diode	X			Marek, 1995
BF_3 counter	X			Tattam et al., 1998.

Tab A.1*. Methods applied for the determination of neutron and gamma ray absorbed dose and thermal neutron fluence in BNCT [48].*

Acknowledgements

It is my pleasure to thank all those who supported me during my thesis activity research. In particular, I would like to extend special thanks:

To my advisors Prof. Grazia Gambarini and Prof. Amos Breskin, to giving me this big opportunity, both professional and personal.

To my co-advisor Dr. G. Battistoni for his hints.

To Dr.Volker Dangendorf of PTB (Braunschweig, Germany) and Dr. David Varsky of Soreq (Yavne, Israel) for their time, helpfulness and knowledge in all of the fields.

To my lab-mates at WIS, Marco Cortesi, for his huge help and his time, Raz Alon, for his kindness, Alexey Lyashenko and Dr. Jun Miyamoto.

To Moshe Klin for his technical help and his warm personality.

To all of the Italian and International new friends, for all the time spent together, the many adventures in the Holy Land and the great leaving party.

To all of the others … It's time to write in Italian!

Ringrazio prima di tutto la mia famiglia per avermi supportato e sopportato in questo periodo. Per essere riusciti a starmi vicino anche quando ero lontano e perchè ormai con la tecnologia non li ferma più nessuno!! GRAZIE mamma, papà, Moira, Lele, Matti, Nico e…auguri Lapo!!

Ringrazio le ficozze (Sandra, Vittu, Valent, Emanu) perché anche se "è un mondo difficile" e spesso è un'impresa organizzare qualcosa, siete sempre un punto di riferimento nella mia vita. Grazie anche a IL Cristian, Theo e Jack.

Ringrazio gli “amici pavesi dell’Area Cattaneo” per le serate, le feste, i video e le belle vacanze trascorse insieme.

Ringrazio la 5TC perché è sempre un piacere ritrovarsi (grazie alla Nato e alla Brusa perché restano sempre le mie compagne di banco preferite, grazie a Morta per la pazienza nel supporto informatico e a Mareo per le perle di buongusto).

Ringrazio i fisici pavesi, in particolare Giorgio e la Madda, perché restano sempre i miei “tutor”; la Sara perché come al solito sparisce, ma è sempre un piacere ritrovarla.

Ringrazio le fisiche sanitarie milanesi e i compagni di laboratorio, in particolare Anna e Fra, una squadra vincente (soprattutto col Martini!) e Giacomo per il suo aiuto e la sua pazienza (ora tocca a te!)

Ringrazio la nonna Gina e la famiglia Rossetti, per avermi accolta tra loro. Certo, un po’ partivo avvantaggiata… !

Ringrazio il basket e la mia squadra (“belle de notte”), perché prima o poi una la vinceremo!

Ringrazio tutte quelle cose/persone che mi hanno permesso di vivere meglio questi ultimi 2 anni… come ad esempio il cibo GF !

Roooooooooss, ringrazio soprattutto te, per averci creduto, per i momenti passati e per quelli futuri… ora inizia la vita vera!

References

[1] R. Chechik, A. Breskin, C. Shalem, D. Mormann, *Thick GEM-like hole multipliers: properties and possible applications.* Nucl. Instr. and Meth. A535 (2004) 303-308

[2] Brownell. G. Zamenhof. R.G. Murray. B.W. Wellum. G.R. *Boron Neutron Capture Therapy in therapy in Nuclear Medicine*. R.P. Spencer (ed.). Grune and Stratton. Inc. New York. (1978)

[3] Barth. R.F. Solloway. A.H. Fairchild. R.G. *Boron Neutron Capture Therapy of Cancer*. Cancer Res. 50:1061-1070. (1990)

[4] G. Gambarini at al. *Study of a method based on TLD detector for in-phantom dosimetry in BNCT.* Radiation Protection Dosimetry 110:1-4 (2004)

[5] International Atomic Energy Agency. *Current status of neutron capture therapy*. IAEA-TECDOC-1223. (vienna: IAEA). p. 9 (2001)

[6] C. Shalem, R. Chechik, A. Breskin, K. Michaeli, *Advances in Thick GEM-like gaseous electron multiplier – part I: atmospheric pressure* . Nucl. Instr. and Meth A 558 (2006) 475-489.

[7] R.L. Bramblett, R.I. Ewing, T.W. Bonner. Nucl. Instr. Meth. 9 (1960)1

[8] MCNP - A General Monte Carlo N-Particle Transport Code Version 5 . *Los Alamos National Laboratory. Nov 2005*

[9] Geant4 user's guide - For toolkit developer – http://geant4.web.cern.ch

[10] K. Kleinknecht, *Pratice detecors*. T. Ferbel, *Experimental Techniques in High Energy Physics*. Frontiers in Physics, Lecture Note Series.

[11] Geiger et al, *Phys. Zeit* . 29, 839 (1928)

[12] H. Raether, *Electron avalanches and breakdown in gases*. Butterworth, London, 1964

[13] G. Charpak et al, *Nucl.Instr. and Meth .,* 62, 262 (1998)

[14] A. Sharmai, *Gaseous Micropattern Detectors: High-Energy Physics Energy Physics and Beyond*

[15] A. Oed et al., *Micro pattern structures for gas detectors*. Nucl. Instr. And Meth. A471 (2001)109.

[16] F. Sauli : *A new concept for electron amplification in gas detector.* Nucl. Instr. and Meth., A386, 531 (1997)

[17] F. Sauli, *Principles Of Operation Of Multiwire Proportional And Drift Chambers*, CERN, yellow report 77-09, 1977

[18] D. Mörmann et al., *Operation principles and properties of the multi-GEM gaseous photomultiplier with Ref photocathode*, Nucl. Instr. and Meth. A530(2004)258.

[19] A. Breskin, *Secondary emission gaseous detectors: a new class of radiation imaging detectors*, Nuclear Physics B (Proc. Supp.) 44 (1995) 351.

[20] V. Dangendorf et al.: *Detectors for time-of-flight fast-neutron radiography 1.Neutron-counting gas detector*., (physics/0408074).

[21] Danilatos, G,D (1988). *Foundations of environmental scanning electron microscopy. Advances in Electronics and Electron Physics* **71**: 109-250.

[22] V.Dangendorf et al, *Thermal neutron imaging detectors combining novel composite foil convertors and gaseous electron multimpliaers.* Nucl. Instr. And Meth A 350 (1994) 503-510

[23] T. Francke - V. Peskov, *Micropattern Gaseous Detectors*, physics/0404035 (April 2004)

[24] M. Cortesi, R. Alon, R. Chechin, A. Breskin, D. Vartsky, V. Dangendorf, *Investigation of a THGEM-based detector*, JINST P09002

[25] ACAM-Messelectronic GmbH, http://www.acam.de

[26] MQT300A, CHARGE-TO-TIME CONVERTER, LeCroy 1999, http://www.lecroy.com/

[27] http://www.jjorly.com/g10_fr4_sheets_fabricator.htm

[28] Glenn F. Knoll. *Radiation detection and measurements*. 3 Edition. John Willey. New York (2000)

[29] F.D. Brooks, H. Klein, *Neutron spectrometry-historical review and present status*, Nucl. Instrum. and Meth. A 476 (2002) 1–11

[30] D.J. Thomas, A.V. Alevra, *Bonner sphere spectrometers – a critical review.* Nucl. Instr. And Meth A 476 (2002) 12-20

[31] J. Chadwick In: B. Maglich, Editor, *Adventures in Experimental Physics*, World Science Education, Princeton (1972), p. 193.

[32] D. J. Thomas, *Neutron Spectrometry For Radiation Protection,* Radiation Protection Dosimetry (2004), Vol. 110, Nos 1-4, pp. 141±149

[33] H.H. Hsu, K.R. Alvar, and D.G. Vasilik, *A new Bonner-sphere set for high energy neutron measurements.* IEEE, VOL. 41, NO. 4. AUGUST 1994

[34] R. Bedogni, C. Domingo, A. Esposito, F. Fernandez, *FRUIT: An operational tool for multisphere neutron spectrometry in workplaces.* Nucl. Instr. and Meth. A 580 (2007) 1301-1309

[35] P. J. B. M. Rachinhas. T. H. V. T. Dias, F. P. Santos, A. D. Stauffer. C. A. N. Conde. *Energy resolution of xenon proportional counters: Monte Carlo and experimental results*. IEEE Trans. Nucl. Sci. 43,1399-2405 (1996)].

[36] H. Friedrich, V. Dangendorf, and A. Brauning-Demian, *Position-sensitive thermal neutron detector with Li-6-foil converter coupled to wire Chambers*. Appl. Phys. A: Mater. Sci. Process., vol. 74, pp. S124–S126, 2002

[37] SRIM-2006

[38] J. Söderberg, *Dosimetry and radiation quality in fastneutron radiation therapy*, Linköping Studies in Health Sciences Thesis no. 989

[39] J. K. Shultis, R. E. Faw, *An MCNP primer*, revised July 28, 2006

[40] http://www.nist.gov/data/

[41] J. Beringer et al., *Validation of Geant4 Hadronic Physics*. Nuclear Science Symposium Conference Record, 2003 IEEE

[42] V. Dangendorf et al.: *Detectors energy resolved fast-neutron imaging*, Nucl. Instr. and Meth. A 535 (2004) 93-97

[43] D. Vartsky et al. : *Time-resolved fast neutron imaging: simulation of detector performance*, Nucl. Instr. and Meth. **A542** (2005) 206–212

[44] Burian et al, *Physics for BNCT*, Journ of Physics 41-2006

[45] Locher. G.L.*Biological Effects and Therapeutic Possibilities of Neutrons* Am. J. Roentgenol. Radium Ther. 36: 1-13. (1936).

[46] Archanbeau. A.O. Alcober. V. Calvo. W.G. Brenneis. H. *Biological Effects of Thermal Neutrons and the $^{10}B(n.\alpha)^{7}Li$ Reaction* In: Biological effects of Neutron and Proton irradiations. 2:55-70. Vienna: International Atomic Energy Agency. (1964).

[47] W. Sweet, M. Javid, *The possible Use of Neutron-capturing Isotopes such as boron-10 in the treatment of neoplasms*, I. Intracranial Tumors, J. Neurosurg., 9 (1952) 200-209.

[48] *Recommendations for the Dosimetry of Boron Neutron Capture Therapy (BNCT).* Petten, 1 December 2003. 21425/03.55339/C.

Riassunto (in lingua italiana)

L'obiettivo dell'attività di ricerca è quello di sviluppare un sistema che permetta di ottenere un *imaging* della componente neutronica veloce (100 keV – 10 MeV) nelle applicazioni di Boron Neutron Capture Therapy (BNCT). Grazie a questo sistema dovrebbe essere possibile ottenere informazioni sullo spettro dei neutroni con la minima sensibilità alla componente gamma del campo.

La Boron Neutron Capture Therapy (BNCT) è una radioterapia binaria che sfrutta l'azione combinata di fasci di neutroni e la biodistribuzione nel tessuto tumorale dell'isotopo ^{10}B, il quale presenta un'elevata sezione d'urto per la reazione con i neutroni termici $^{10}B(n, \alpha)^{7}Li$ (σ = 3840 barn). Durante un trattamento BNCT viene somministrato al paziente, per infusione intravenosa, un composto non tossico di ^{10}B, che si distribuisce nei vari tessuti del corpo. Tale composto è legato per sintesi chimica a specifici carriers per cui, in un appropriato intervallo di tempo, il boro si accumula selettivamente in concentrazioni più elevate nelle cellule tumorali, piuttosto che nel tessuto sano. Sfruttando questo accumulo selettivo dell'isotopo ^{10}B nelle cellule malate, si effettua un irraggiamento con neutroni termici (per tumori superficiali) o epitermici (per tumori profondi). Gli atomi del ^{10}B reagiscono con i neutroni generando due particelle cariche ad alto trasferimento lineare di energia (LET): una particella α e una particella ^{7}Li. Queste particelle hanno un breve *range* in tessuto e rilasciano di conseguenza quasi tutta la loro energia in prossimità del luogo dove sono state prodotte, ossia nelle cellule malate. Il rilascio di energia entro le cellule malate innesca una serie di processi che portano al danneggiamento del DNA e quindi alla morte della cellula stessa.
La BNCT è finora stata realizzata sfruttando fasci di neutroni prodotti in reattore, dal momento che le altre sorgenti di neutroni non sono in grado di garantire fluenze sufficientemente elevate di neutroni. La dose totale assorbita (energia impartita per unità di massa) da un tessuto irraggiato con neutroni di bassa energia è dovuta al contributo proveniente dalle diverse componenti presenti nel fascio incidente (neutroni termici, intermedi, veloci e raggi gamma). Innanzitutto si ha la dose gamma dovuta al fondo del reattore, che presenta uno spettro di energie variabile tra 0 e 15 MeV, e quella dovuta ai raggi gamma creati nel tessuto a causa dell'assorbimento dei neutroni termici da parte degli atomi di idrogeno ($^{1}H(n,\gamma)^{2}H$, energia dei

fotoni pari a 2.2 MeV); la dose dei neutroni epitermici e veloci dovuta ai protoni di rinculo generati dalla reazione $^{1}H(n,n')p$; la dose dovuta alla reazione dei neutroni termici con l'azoto presente all'interno del tessuto $^{14}N(n,p)^{14}C$ e la dose terapeutica dovuta alla reazione con ^{10}B che contribuisce alla dose totale assorbita anche nei tessuti sani in cui eventualmente si sia fissato il boro. L'energia emessa dalle particelle α e dagli ioni ^{7}Li risulta pari a 2.33 MeV.
Le varie componenti di dose hanno un diverso valore del fattore RBE (efficacia biologica relativa) e per questo vanno determinate separatamente. Per un trattamento sicuro dei pazienti con le radiazioni ionizzanti è sempre essenziale misurare e registrare con accuratezza le dosi prescritte. E' dunque necessario disporre di un affidabile sistema di monitoraggio della dose al fine di verificare che le caratteristiche del fascio siano conformi e soddisfino a tutte le restrizioni. Di conseguenza, per la pianificazione del trattamento BNCT è importante la determinazione della distribuzione spaziale delle varie componenti di dose, in accordo con i parametri definiti dall' International Atomic Energy Agency (IAEA). In particolare, la dose da neutroni veloci ha un significativo effetto radiobiologico ed è ancora difficile da rivelare.

Il *detector* proposto inizialmente era costituito da uno strato di polietilene (o polipropilene) per la conversione dei neutroni veloci in protoni, accoppiato a due THGEM (THick Gas Electron Multipliers) in cascata e un elettrodo di read-out. Questo sistema permetterebbe di ottenere, in modo rapido ed economico, una stima della componente neutronica veloce e la sua distribuzione spaziale per le applicazioni di BNCT.
Per una buona rappresentazione spaziale di un fascio di neutroni veloci, il detector dovrebbe essere caratterizzato da alta efficienza neutronica e da bassa sensibilità a raggi gamma. E' quindi necessario trovare un compromesso tra l'efficienza dei neutroni e la sensibilità ai gamma, ottimizzando la geometria del convertitore in base all'energia del fascio incidente.

I THGEM (THick Gas Electron Multipliers) sono stati introdotti nel 2004 presso il Radiation Detection Laboratory dell'Istituto Weizmann (Rehovot, Israel) e sono il più recente sistema sviluppato per la rivelazione delle particelle cariche e dei fotoni. Il principio di funzionamento si basa sulla moltiplicazione degli elettroni nel gas all'interno dei fori.
Essi sono fabbricati con la tecnica Printed Circuit Board (PCB), basata sul doppio rivestimento di un materiale isolante (FR - 4, Kevlar, Teflon, ecc…).

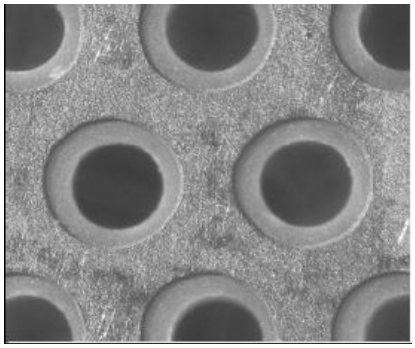

***Fig 3**. Immagine al microscopio di un THGEM.*

L'elettrodo consiste in una piastra forata meccanicamente, con un bordo (in genere 0,1 mm) inciso chimicamente intorno ad ogni foro (*Fig.1*). Questo bordo è essenziale per ridurre la probabilità di scariche nel gas; sono dunque ammissibili tensioni superiori e, di conseguenza, è possibile ottenere guadagni più elevati. Il principio di funzionamento del THGEM è identico a quello di un normale GEM.

L'applicazione di una differenza di potenziale sul THGEM, genera un forte campo di dipolo (E_{hole}) all'interno dei fori. Gli elettroni depositati dalla radiazione ionizzante, nella regione di conversione al di sopra del THGEM, si muovono sotto l'azione del campo E_{drift} e vengono focalizzati all'interno dei fori, grazie al forte campo elettrico presente all'interno di essi. Gli elettroni sono moltiplicati all'interno dei fori, sotto l'azione del forte campo elettrico (25-50 Kv / cm); in base alle dimensioni e alla direzione del campo E_{trans}, una frazione della risultante valanga di elettroni è raccolta sull'elettrodo inferiore del THGEM, mentre la parte restante può essere ulteriormente trasferita ad un anodo di raccolta o ad un successivo elemento moltiplicatore (*Fig.2*). Ogni foro agisce come un moltiplicatore indipendente e il confinamento della valanga entro i fori ha il vantaggio di ridurre effetti secondari; questo porta ad alti guadagni e alla possibilità di funzionamento in una grande varietà di gas.

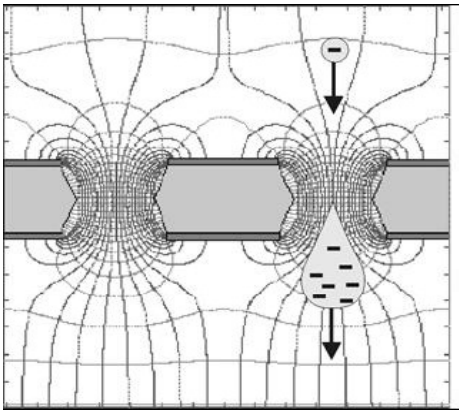

Fig 2. *Schema del principio di funzionamento di un GEM. Gli elettroni seguono le linee del campo e vengono focalizzati all'interno dei fori, dove si genera la moltiplicazione a valanga a causa della presenza di un forte campo elettrico.*

L'attuale prototipo di detector è costituito da uno strato (di spessore variabile) di moderatore/assorbitore, composto da polietilene miscelato con un isotopo assorbitore di neutroni lenti (^{6}Li o ^{10}B), e da un foglio di convertitore di neutroni posto sul retro dello strato. Il tutto è accoppiato a due THGEM in cascata e ad un elettrodo di read-out. Per lo studio iniziale si è deciso di utilizzare ^{6}Li puro sia come dopante nel moderatore che come strato convertitore. Il principio è molto simile a quello delle sfere di Bonner, ma invece di usare delle sfere si utilizza una serie di lastre piane con diversi spessori. Lo spettrometro a sfere di Bonner è l'unico sistema spettrometrico per i neutroni che copra l'intera gamma di energie, da neutroni termici ai GeV. Questo sistema è costituito da un sensore di neutroni termici (ad es. ^{6}LiI(Eu)), che viene utilizzato al centro di una serie di diverse sfere di polietilene. Dalla lettura delle misure effettuate con un set di sfere, è possibile ricavare informazioni riguardanti lo spettro del campo di neutroni in cui sono state effettuate le misure. La derivazione di queste informazioni spettrali non è semplice e la validità dei risultati delle BS è stata spesso messo in discussione. La nuova idea qui proposta prevede di ottenere informazioni spaziali, anche se con scarsa risoluzione energetica, in modo da ottenere una più completa caratterizzazione del fascio.

Una volta sviluppato il sistema, si vorrebbero effettuare anche alcune misure in modo da ottenere informazioni che attualmente non si possono trovare in letteratura, ma utili per la ricerca nel campo della BNCT. L'obiettivo è quello di determinare contemporaneamente lo spettro di neutroni con adeguata risoluzione energetica e con una risoluzione spaziale di qualche centimetro all'interno di un fantoccio cilindrico (con la dimensione della testa) a diverse profondità, rispetto al fascio di neutroni incidente. Questo potrebbe essere ottenuto mediante la

ripetizione della serie di misurazioni effettuate in aria al collimatore, ma utilizzando fantocci di diversi spessori, costituti da materiale tessuto equivalente, posizionati di fronte allo spettrometro. Le misurazioni devono essere ripetute con spessori sempre più elevati, fino al raggiungimento delle dimensioni del fantoccio. In questo modo potrebbe essere possibile avere informazioni circa le variazioni dello spettro dei neutroni all'interno del fantoccio. Questa informazione sarebbe utile sia per valutazioni dosimetriche sia per la valutazione delle fluenze termiche ed epitermiche ottenuta da misure per attivazione, applicando le tecniche di unfolding: infatti al momento questi metodi utilizzano, anche all'interno dei fantocci, lo spettro del fascio di neutroni al collimatore non essendo disponibile altra conformazione.

Il lavoro è stato basato sull'utilizzo dei calcoli Monte Carlo, utilizzando MCNP e GEANT4 come codici di simulazione, e sull'attività sperimentale finalizzata ad eseguire studi sulla fattibilità e sullo sviluppo di un detector basato sulla tecnologia dei THGEM, per poter ottenere un *imaging* della componente neutronica veloce con bassa sensibilità ai raggi gamma. L'attività di ricerca è stata frutto di una collaborazione tra il laboratorio di dosimetria della Prof.ssa Gambarini e il laboratorio di Radiation Detection del Prof. Breskin all'Istituto Weizmann di Rehovot (Israele), con la collaborazione del Dott. Dongendorf (PTB, Germania) e del Dott. Varsky (Soreq, Israele).